Synthesis and Reactivity of Silver Complexes of Nitrogen Confused Scorpionate Ligands

Fathiya Jahan
Marquette University

SYNTHESIS AND REACTIVITY OF SILVER COMPLEXES OF NITROGEN CONFUSED SCORPIONATE LIGANDS

by

Fathiya Jahan, M.S.

A Thesis submitted to the Faculty of the Graduate School,
Marquette University,
in Partial Fulfillment of the Requirements for
the Degree of Master of Science

Milwaukee, Wisconsin

August 2019

ABSTRACT
SYNTHESIS AND REACTIVITY OF SILVER COMPLEXES OF NITROGEN CONFUSED SCORPIONATE LIGANDS

Fathiya Jahan, M.S.

Marquette University, 2019

Scorpionate ligands are one of the most crucial nitrogen donor ligands in coordination chemistry. The scorpionate ligands have served as excellent ligand scaffolds for investigating iron(II) spin crossover chemistry. In this study, the complex, $[Fe(^{H}L^{*})_2](OTf)_2$, **1**, where $^{H}L^{*}$ = bis(3,5-dimethylpyrazol-1-yl)(3-1H-pyrazole)methane was prepared which exhibited multiple solid-state structures and solvates. Six crystalline forms of **1** were prepared by controlling the crystallization conditions. Thus, when reagents are combined in CH_3CN, an equilibrium mixture of *cis*- and *trans*- is established that favors the latter below 310K. Among the six crystal forms, *trans*-**1**, *trans*-**1**.CH_3CN, *cis*-**1** and *co*-**1** undergo SCO below 250K while *trans*-**1**.xCH_3CN (x=2,4) solvates do not undergo SCO before desolvation. Another application of the scorpionates is in nitrene transfer reactions. In this contribution, two new N-confused C-scorpionates, $^{Ts}L^{ipr2}$ and $^{H}L^{ipr2}$, each with two 'normal' 3,5-diisopropylpyrazolyl groups, and either an N-tosyl or N-H group on the 'confused' pz were synthesized. These new ligands complement those previously described dimethylpyrazolyl derivatives, $^{H}L^{*}$ and $^{TS}L^{*}$, which have less bulky 'normal' pyrazol-1-yls. For these two bulky N-confused scorpionate ligands, the 2:1 and 1:1 ligand:silver complexes were prepared and characterized both structurally and spectroscopically. Their potential as catalysts for nitrene transfer reactions was also investigated.

ACKNOWLEDGEMENTS

Fathiya Jahan

Firstly, I would like to express my sincere gratitude to my advisor, Dr. James Gardinier, for giving me the opportunity to work in his research lab. I am grateful for his guidance, patience and encouragement which I received from him to complete this research work. I would also like to thank my committee members, Dr. Adam Fiedler and Dr. Scott Reid, for their valuable feedback on my thesis. I would like to thank faculty members Dr. Sergey Lindeman for providing us the single crystal diffraction analysis data and Dr. Sheng Cai for helping me with variable-temperature NMR experiments. I am thankful to all my present group members, Dr. Denan Wang and Billy Shone and past group members Kristin Meise and Alex Trelevan for their tremendous support during the completion of this research work.

I am extremely grateful to my beloved parents Sheikh Abdur Rouf and Jahan Ara Arju for their love and sacrifices for educating and preparing me for my future. I would like to express my love for my niece, Maryam Hasan, who came to my life as a blessing. Lastly, I would like to thank my husband, Taukir Ahmed, for being my support and never to stop believing in me.

TABLE OF CONTENTS

LIST OF TABLES

LIST OF FIGURES

CHAPTER 1: INTRODUCTION

Nitrenes are electron deficient, uncharged molecular fragments consisting of a nitrogen atom which has only six electrons in its valence shell. They can exist as both singlet state and triplet state. In singlet state nitrenes have two pairs of electrons and a low- energy empty orbital. In the triplet state they have one electron pair with two electrons in parallel spins as shown in figure 1.1.[1]

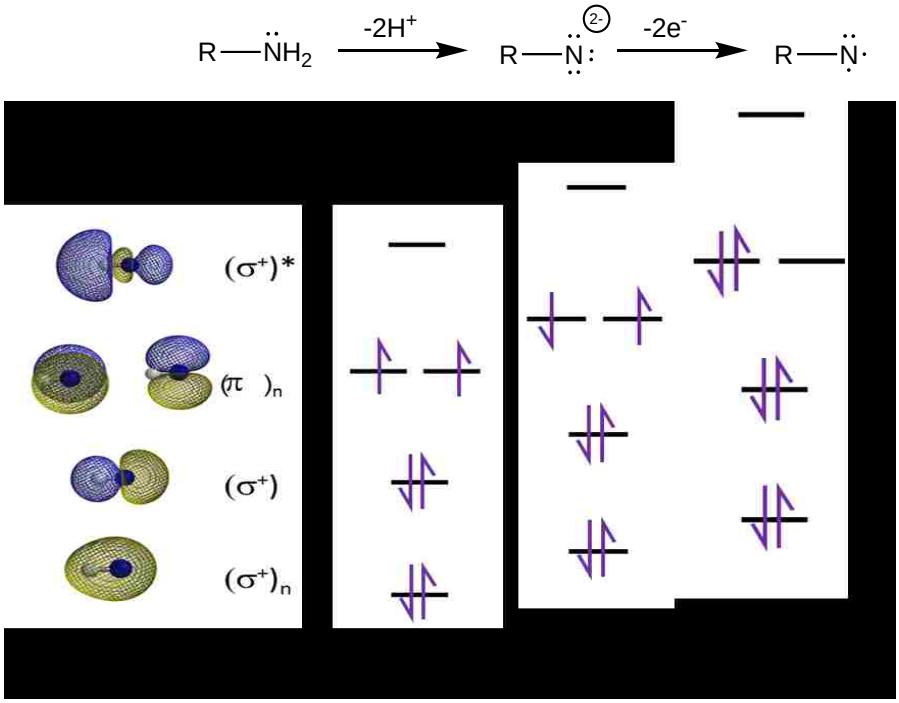

Figure 1.1. Electronic States of Nitrene

Transition metal catalyzed nitrene transfer is a promising synthetic method to install valuable carbon−nitrogen bonds that are widespread in natural products and pharmaceuticals.[2-5] Transition metal catalyzed nitrene transfer typically involves the formation of a metal-imido intermediate in the presence of a nitrene precursor and a transition metal catalyst [L_nM]. Group 11 elements such as copper and silver catalysts show great promise as cost effective alternates to conventional Rh catalysts.[2] Hypervalent

iodine reagents are the common nitrene sources for these nitrene transfer reactions as shown in equation 1.[9]

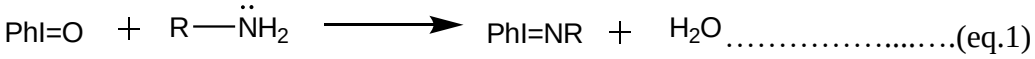

.....(eq.1)

The metal-imido intermediate then undergoes reaction with an organic substrate and two main modes of reactivity have been observed as shown in figure 1.2. [3]

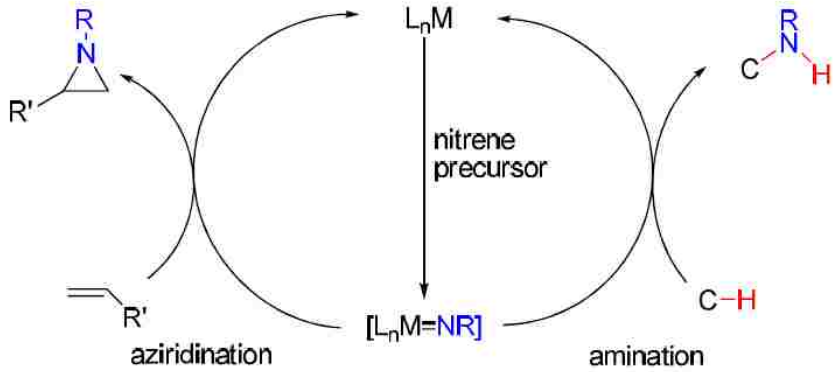

Figure 1.2. Transition metal catalyzed nitrene transfer reactions. Figure is taken from reference 3.

Addition of the nitrene across a C=C in an unsaturated organic substrate such as olefins, yield a strained, three membered ring containing one nitrogen atom known as the aziridine. The aziridine is an important synthetic intermediate in many organic syntheses and in pharmaceuticals.[4]

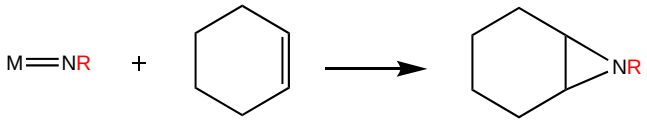

.....(eq.2)

This aziridination reaction is thought to proceed by the formation of a radical intermediate as shown in figure 1.3.[5]

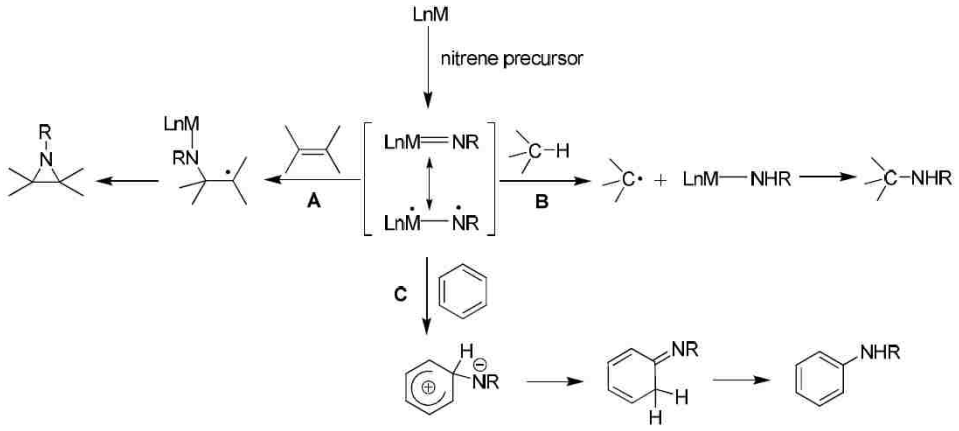

Nitrene precursors: ArINTs, ArINNs, NaCINTs, ArN_3 etc.

Figure 1.3: Proposed mechanism for transition metal mediated aziridination of olefins (route A), amination of sp^3 C-H bonds (route B) and aromatic C-H bonds (route C). Figure is taken from reference 5.

The second mode of reactivity of the metal-imido intermediate is the C-H bond amination which involves insertion of the nitrene into a C-H bond of an organic substrate giving the amine product. Amination of a sp^3 C-H bond will take place by a stepwise abstraction of hydrogen and radical rebound mechanism giving the carboradical intermediate as shown in the figure 1.3 (route B). In contrast, the direct amination of an aromatic (sp^2) C-H bond involves the electrophilic addition of nitrene radical to an aromatic C=C bond as shown in figure 1.3 (route C).[3-5] In 1968, Breslow and Sloan heated a solution of dichloramine-T(I) in cyclohexane with Zn to yield a sulfonyl nitrene which inserted into a C-H bond of the solvent as shown in equation 3.[6]

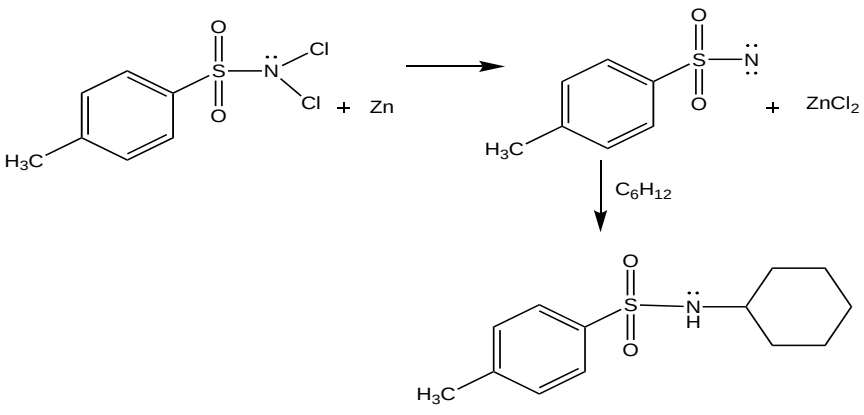

……(eq.3)

In 1982, Breslow and Gellman used manganese or iron tetraphenylporphyrin (TPP) to catalyze a nitrogen insertion reaction.[7] Cyclohexane was reacted with (tosyliminoiodo) benzene and manganese(III) - or iron(III) -tetraphenylporphyrin chloride to afford N-cyclohexyltoluene-p -sulphonamide as shown in equation 4.

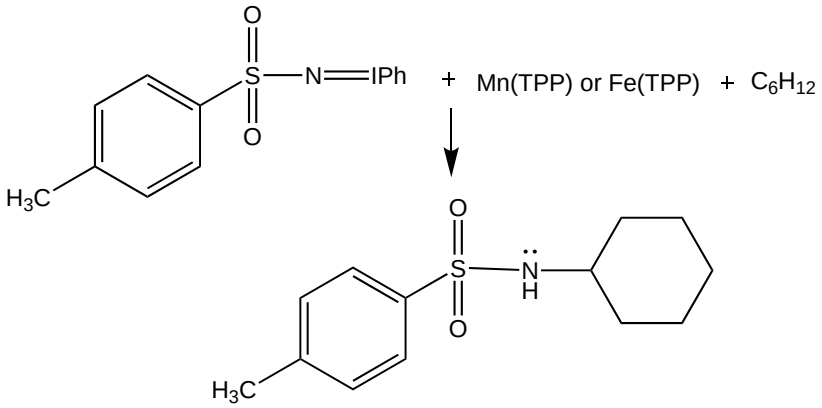

……(eq.4)

The first report of an efficient olefin aziridination reaction catalyzed by a disilver(I) compound was from the He group.[8] Efficient aziridination of olefins were performed by using 1 equivalent of a tridentate 4,4′,4″-tri-tert-butyl-2,2′:6′,2″-terpyridine (tBu_3tpy), 1 equivalent of a silver(I) salt as the catalyst and PhI=NTs as a nitrenoid source in acetonitrile as shown in equation 5. No reaction was observed in the absence of the

silver(I) salt and the reaction was unaffected by the counteranions (NO_3^-, OTf^-, ClO_4^- and BF_4^-).

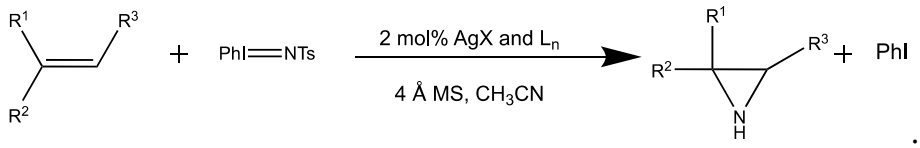

…….(eq.5)

Olefin aziridination was also carried out with pyridine or 4-tert-butyl-pyridine as the ligand but only a trace amount of aziridine product was obtained. Other ligands like bipyridine, 4,4′-di-tert-butyl-bipyridine, or 2,2′:6′,2″-terpyridine (tpy) gave a decent yield of aziridine along with a variety of byproducts. However, no product was observed when t Bu-bis(oxazoline) or Ph-bis(oxazoline)- pyridine was used as the ligand. The effect of ligand on the yield of the olefin aziridination reaction is given in table 1.1.

Table 1.1: Effect of ligand on the yield of the olefin aziridination reaction. Table is taken from reference 8.

Ligand	**Yield (GC)**
pyridine	trace
4-*tert*-butylpyridine	trace
bipyridine	35-50 %
4,4'-di-*tert*-butylbipyridine	35-50 %
2,2':6',2''-terpyridine (tpy)	35-50 %
4,4',4''-tBu_3tpy	66-91 %
4-*tert*-butylbis(oxazoline)	-
4-phenylbis(oxazoline)pyridine	-

Crystal structure of $[Ag_2(^tBu_3tpy)_2(NO_3)](NO_3)$ contained a dinuclear Ag core with a short Ag-Ag interaction of 2.842 Å as shown in figure 1.4. Both $Rh_2(OAc)_4$ which is used to catalyze similar olefin aziridination [9,10] reactions and $[Ag_2(^tBu_3tpy)_2(NO_3)](NO_3)]$ have short metal-metal distances and accessible coordination sites at the terminal positions which means that the two systems may share similar mechanistic characteristics. Thus, a disilver compound is required to catalyze the two electron nitrene transfer.

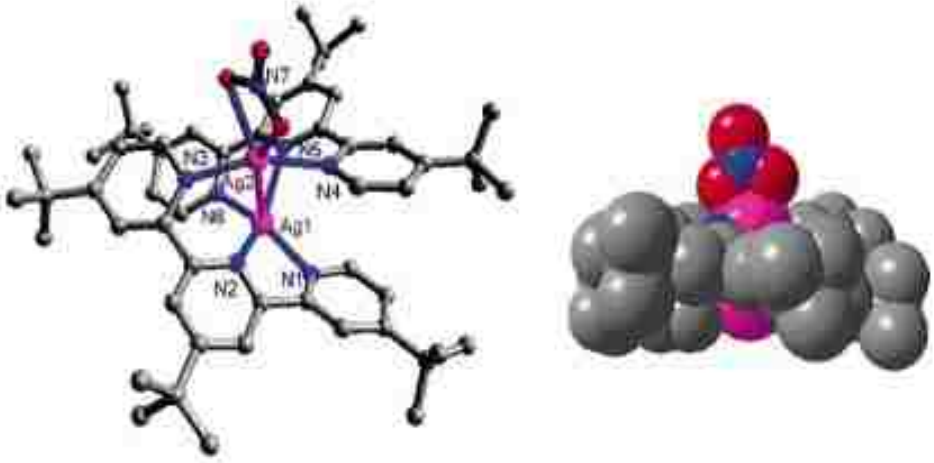

Figure 1.4: The molecular structure and space filling model of $[Ag_2(^tBu_3tpy)_2(NO_3)](NO_3)]$. Figure is taken from reference 8.

Extensive studies have been done for the aziridination reactions using alkenes as substrates but only a handful can be found with conjugated dienes as the substrate. However, previous studies of vinylaziridines using Cu and Ru-based catalysts have the drawbacks that only symmetric dienes can be used and the stereoselectivity (intended cis/ trans or trans/cis) of the vinylaziridine cannot be controlled.[11-12] The Perez group reported a MTp^x (M= Cu, Ag) complex that catalyzed vinylaziridination reactions using

trans,trans-2,4-hexadien-1-ol as the substrate which is a nonsymmetric diene with an -OH group.[13] The primary goal of their study was to control the stereo and regioselectivity of the vinylaziridine. Aziridination reaction of this kind of nonsymmetric diene would give rise to two different kinds aziridines each of them with a cis or trans geometry. These are formed either by nitrene addition to the double bond vicinal to the hydroxy end of the substrate or by nitrene addition to the double bond vicinal to the methyl end as shown in figure 1.5.

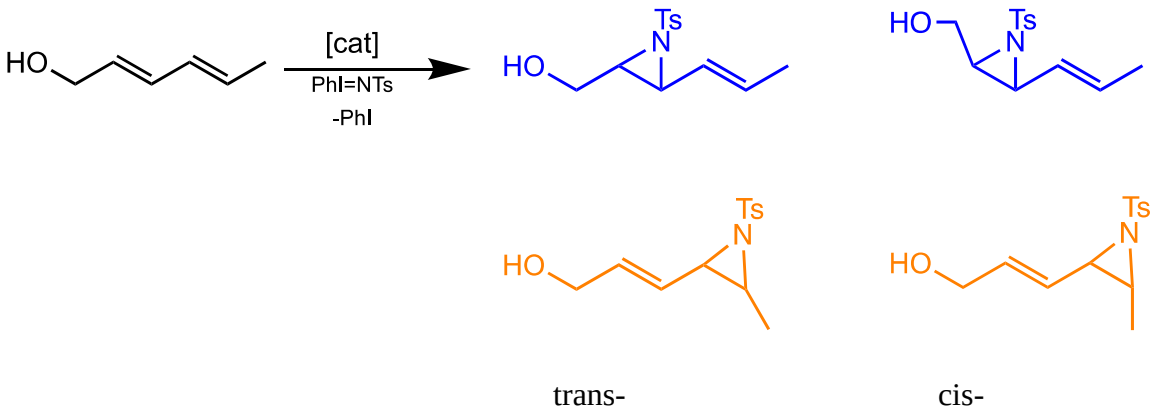

Figure 1.5: Aziridination of trans,trans-2,4-hexadien-1-ol with Tp^{x}M catalysts (M=Cu, Ag) using PhINTs as the nitrene source. Figure taken from reference 13.

Table 1.2: Reaction of trans,trans-2,4-hexanedien-1-ol with Tp^{x}M catalysts(M= Cu, Ag) using PhINTs as the nitrene source. Table taken from reference 13.

Catalyst	**Conv. %**	**Regio.**	***trans/cis***
[Tp*Cu][(a)]	> 67	82:18	66:34
[Tp*Ag][(a)]	> 95	90:10	>98:<2
[Tp*^{,Br}Ag][(a)]	> 99	90:10	>98:<2
[Tp*^{,Br}Ag][(b)]	> 99	89:11	>98:<2
[Tp*^{,Br}Ag][(c)]	80	89:11	>98:<2
[Tp*^{,Br}Ag][(d)]	> 99	88:12	>98:<2

Reaction Conditions:

a) [cat.]/[PhINTs]/[substrate]=1:20:30, 0.0125 mmol catalyst, 5% cat. loading.

b) [cat.]/[PhINTs]/[substrate]=1:200:300, 0.0046 mmol catalyst, 0.5% cat. loading
c) [cat.]/[PhINTs]/[substrate]=1:1000:15000, 0.0030 mmol catalyst, 0.1% cat. Loading
d) [cat.]/[PhINTs]/[substrate]=1:200:200, 0.0125 mmol catalyst, 0.5% cat. Loading

Tp^xM (M=Cu, Ag) complexes were able to catalyze the aziridination of dienes containing a terminal hydroxy group. Aziridine formed by the nitrene addition to the double bond vicinal to the hydroxy end of the substrate was favored by the Tp^xCu complex. However, the copper catalyst showed low selectivity as it caused a certain degree of inversion of the initial trans configuration of the diene and yielded a final trans to cis aziridine ratio of 1:1 to 2:1. On the other hand, only trans aziridines were observed with the Tp^xAg complexes. Since Tp^xBr gave nearly quantitative conversion using a 5% catalyst loading, the aziridination reaction was then conducted by using a 0.1% and 0.5% catalyst loading. No loss of catalytic activity was observed at 0.5% catalyst loading. However, the aziridine conversion dropped to 80% when 0.1% catalyst loading was used as shown in table 1.2. When a 1:200:200 ratio of [cat.]/[PhINTs]/[diene] was used an approximately 9:1 mixture of regioisomers of aziridines was formed, with complete retention of its configuration. In order to test if the high selectivity was a result of the directing effect of the hydroxyl group, the Perez group[13] next employed O-protected dienes containing an acetyl or benzyl groups. Lower conversions into aziridines, and lower regioselectivity were observed when O-protected dienes were used (acetal, benzyl) which confirmed high regioselectivity was caused by the directing effect of the hydroxyl group.

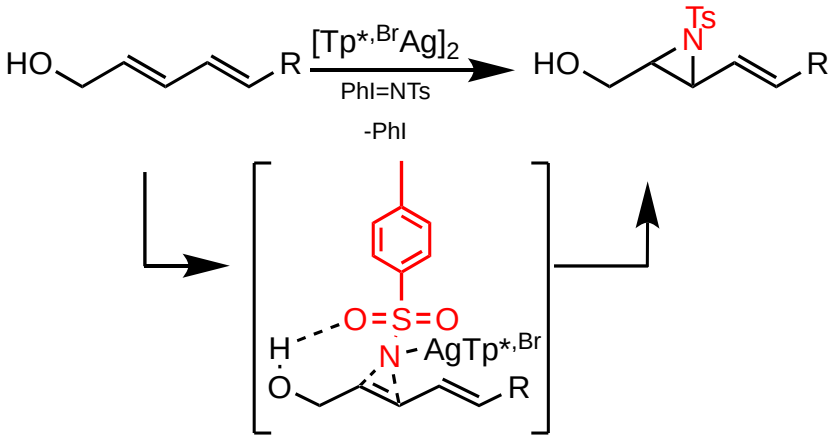

Figure 1.6: Reaction of O-protected diene with $[Tp^{*Br}Ag]_2$ catalyst using PhINTs as the nitrene source. [R=Ac, 78% conversion and R=Bn, 66% conversion]. Figure is taken from reference 13.

The diene aziridination was then applied to the synthesis of an amino alcohol, (±) sphingosine with an overall yield of 65% as shown in figure 1.7.

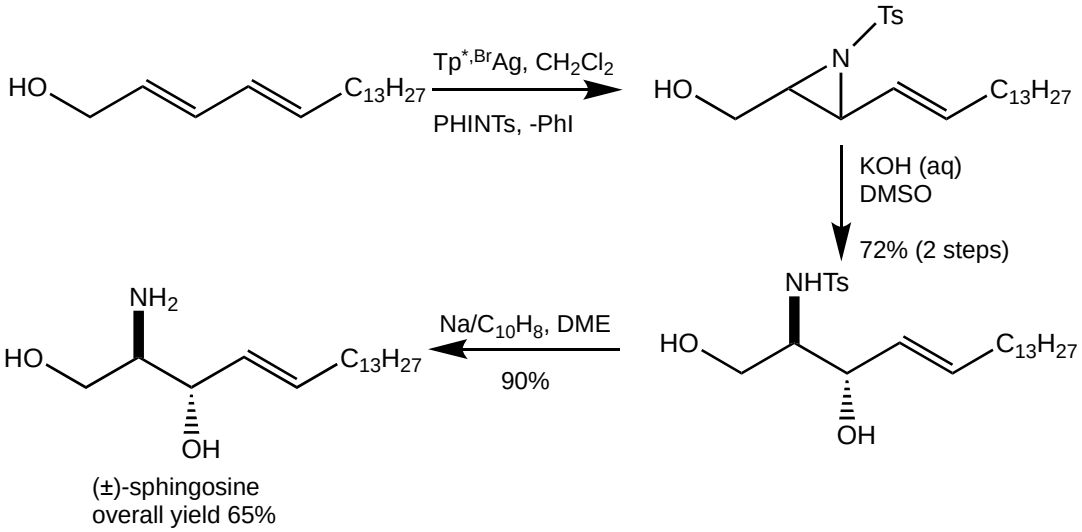

Figure 1.7: Application of the diene aziridination reaction to the synthesis of (±) sphingosine. Figure taken from reference 13.

The mechanism of nitrene transfer in these reactions is still uncertain. It has been suggested that the metal nitrene is an active intermediate in the catalytic cycle.[14] The metal-nitrene intermediate can exist in two electronic states, singlet and the triplet state.

A stepwise or radical mechanism will give rise to the triplet species whereas a singlet state will be formed from a concerted mechanism as shown in figure 1.8. In order to investigate the olefin aziridination reactions from a mechanistic point of view, the Diaz and Perez groups employed several mechanistic probe reactions.[14] The most commonly performed mechanistic probe experiment is to study the stereospecificity of the olefin aziridination reaction. Retention of the stereochemistry of the olefin suggests a concerted mechanism whereas a certain loss or inversion of the olefin geometry suggests a stepwise mechanism.

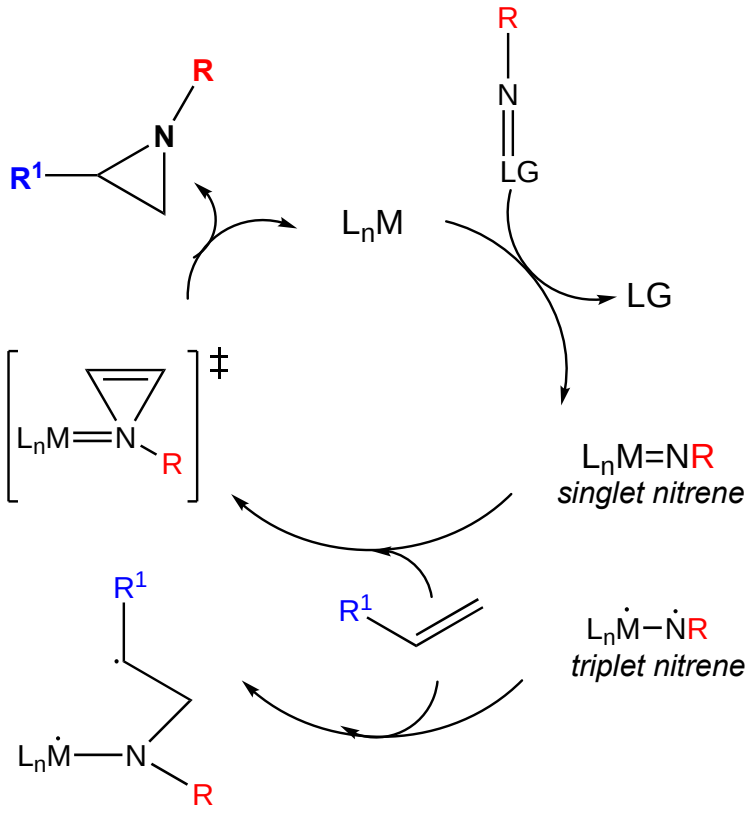

Figure 1.8: Two commonly proposed pathways for nitrene transfer. Figure is taken from reference 14.

Olefin aziridination was carried out with four different Z- or E-olefins using copper and silver complexes of a series of hydrotris(pyrazolyl)borate Tp^{x} ligands. Each type of olefin was converted to the corresponding aziridines with complete retention of olefin geometry which contradicts the previous result with E,E-hexadien-1-ol with copper and silver based catalysts.[13] The observance of retention of initial geometry by the olefins suggests that the concerted mechanism is prevalent in both Cu and Ag based catalysts. Other mechanistic probe experiments include the addition of radical inhibitors (presence of absence of t-butylhydroxitoleuene, BHT) or the use of radical clocks as substrates. Loss of aziridine yield in the presence of a radical inhibitor suggests a stepwise mechanism. When the aziridination was performed by $Tp^{*,Br}M$ (M= Cu, Ag), the copper based catalyst showed a dramatic loss of aziridine yield in the presence of BHT whereas the silver catalyst showed no change.[14] Therefore, the silver-based catalyst may not form a radical intermediate or the intermediate was very short lived and intercepted by BHT. The Diaz and Perez groups subsequently investigated aziridination of 1,1-dicyclopropylethylene (radical clock) using $Tp^{Br3}Cu$ and $Tp^{*,Br}Ag$ catalysts.[14] The silver catalyst preferentially formed the imine product while the copper catalyst showed minor amounts of other products. From these experiments, copper system showed a stepwise mechanism, but silver did not. Their mechanistic proposal from the experimental and theoretical calculations suggests that the reaction starts with the formation of a metal-nitrene intermediate in the triplet state. The copper nitrene intermediate is $Tp^{Me2}Cu^{II}N{\cdot}Ts$ but the silver-nitrene intermediate has two unpaired electrons on the nitrogen atom. This metallonitrene intermediate can attack the olefin through a transition state (^{3}TS) resulting to the formation of the first carbon-nitrogen bond. The triplet state is intercepted with the

singlet before the intermediate (^{3}RI) is formed in the case of silver catalyst as shown in figure 1.9.[14] This explains the retention of stereochemistry by the olefins when the silver catalyst was used. This indicates that the aziridination of olefins by silver catalyst follows a concerted pathway, however, lack of fitting to the plain Hammett equation indicates polar and radical contribution. For the copper catalyst, the interception of the triplet state with the singlet takes place beyond the ^{3}RI intermediate. Since the radical intermediate is formed first for the copper catalyst, the addition of a radical inhibitor lowers the aziridine yield. Thus, the previously accepted proposal that retention of stereochemistry of the olefin suggests a concerted pathway is not valid. The Diaz and Perez group[14] suggested that a stepwise pathway with a triplet copper-nitrene intermediate can also give stereospecific aziridination. Also, for the silver catalyst the initial metal-nitrene intermediate is biradical even though it follows a concerted pathway.

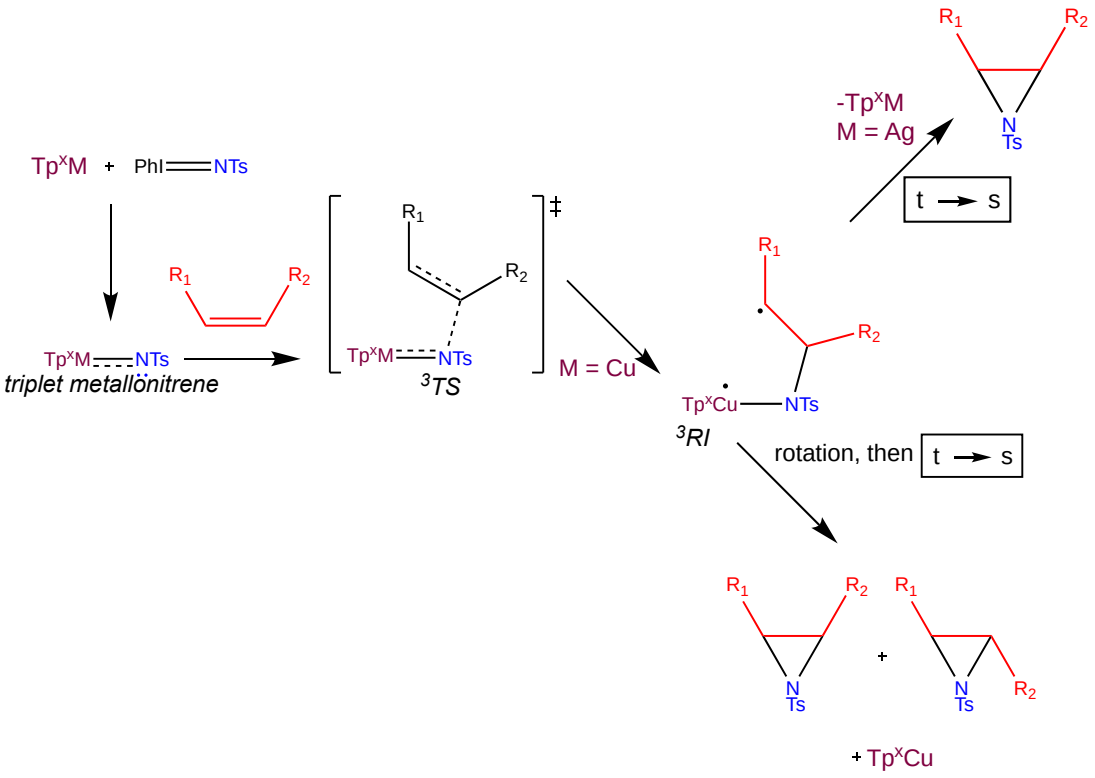

Figure 1.9: Mechanistic proposal for the olefin aziridination reaction catalyzed by Tp^xM (M= Cu, Ag; Tp^x= hydrotrispyrazolylborate ligand). Figure is taken from reference 14.

Detailed studies have been done for metal catalyzed amidation of C-H bonds, however, efficient examples of such reactions are only a handful. The He group[15] have synthesized a disilver(I) $[Ag_2(tBu_3tpy)_2(NO_3)](NO_3)]$ (tBu_3tpy=4,4',4''-tri-tert-butylterpyridine) compound that acts as an efficient catalyst for olefin aziridination and intramolecular C-H amidation reactions but the amidation reaction must be carried out at 82˚C and this disilver catalyst failed to conduct intermolecular C-H amination even at elevatedtemperatures as shown in equation 6.

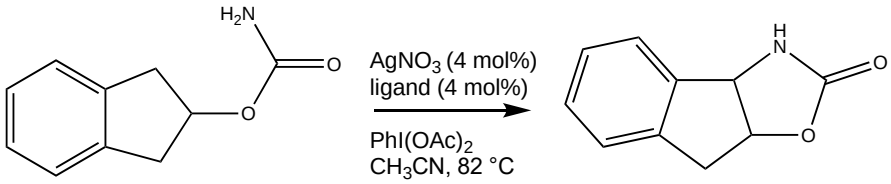

……..…(eq.6)

The He group[16] then introduced a less electron-donating ligand system, a commercially available bidentate ligand, bathophenanthroline. The new catalyst system of silver(I) trifluoromethane sulfonate (AgOTf) with 4,7-diphenyl-1,10-phenanthroline proved to be an excellent catalyst for intermolecular amination of benzylic C-H bonds as shown in equation 7.

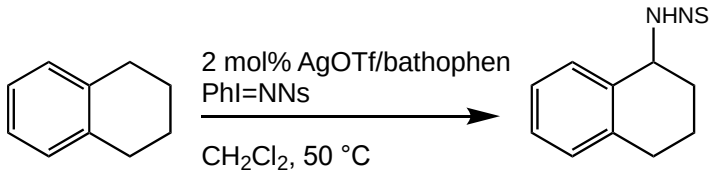

…….……(eq.7)

Silver is known to have the unique ability to change coordination geometry in the presence of different Ag counteranion, different ligands, or different metal/ligand ratios. Thus, treatment of a single Ag salt and a single ligand will give different catalysts with varying selectivity. The Schomaker group[17] used this concept and developed a AgOTf: phenanthroline catalyst system for the aziridination of homoallenic carbamates to bicyclic methylene aziridine. When metal: ligand ratio was 1:1, aziridination was the major mode of reaction. When ligand amount was increased, C-H insertion was favored as shown in figure 1.10. This indicates that an equilibrium exists between Ag(phen)OTf and $Ag(phen)_2OTf$ and each complex favors a different mode of reactivity. For tri- and disubstituted allenes, the rate of aziridination was faster than C-H insertion. Blocking of C-H insertion potential sites resulted in no or decreased reactivity in the case of $Ag(phen)_2OTf$ while the reactivity of Ag(phen)OTf catalyst towards aziridination remained unaffected. This indicates that steric congestion on the Ag center favors insertion and less steric congestion favors aziridination.

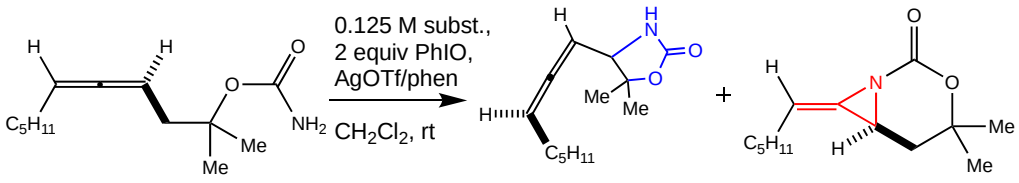

Figure 1.10: Effect of AgOTf: phen stoichiometry on the Aziridination/Insertion Ratio. Figure is taken from reference 17.

Compared to $AgTp^x$ and other anionic B-scorpionates the reaction chemistry of AgTpms or $[Ag_n(Tpm^x)_m]^+$ are less explored because of the difficulty in the ligand synthesis.[18-19] The efficient aziridination and amination catalysis have been reported by other groups using silver complexes of charge neutral nitrogen donor ligands, but only a

handful reports can be found for tris(pyrazolyl)methanes. Our group has recently synthesized a new class of tris(pyrazolyl)methanes, the nitrogen-confused C-scorpionates, where one of the three pyrazolyl rings is bound to the central methine carbon atom via a pyrazolyl ring carbon atom rather than the more usual nitrogen atom. Two new nitrogen-confused C-scorpionate ligands with two "normal" pz* groups (=3,5-dimethylpyrazol-lyl) and a "confused" pyrazolyl with either N-H, ^{H}L*, or N-Tosyl (Tosyl=p-toluenesulfonyl), ^{Ts}L*, bound to a central methine carbon atom were prepared as shown in figure 1.11. These bulky ligands complement those previously described, ^{H}L and ^{Ts}L, which had less bulky, unsubstituted, "normal" pyrazol-1-yls.[20]

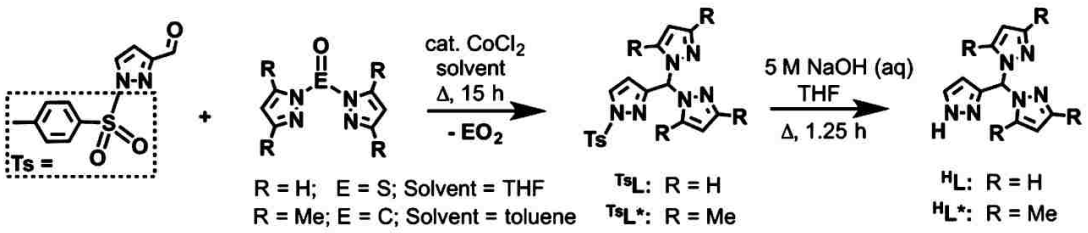

Figure 1.11: Preparative routes to Nitrogen-Confused Scorpionate ligands. Figure is taken from reference 20.

For these four related nitrogen-confused scorpionate ligands, the 2:1 and 1:1 ligand/silver complexes were prepared and characterized both spectroscopically as shown in figure 1.12 and figure 1.3. The complexes' catalytic activity for aziridination of styrene were also reported.

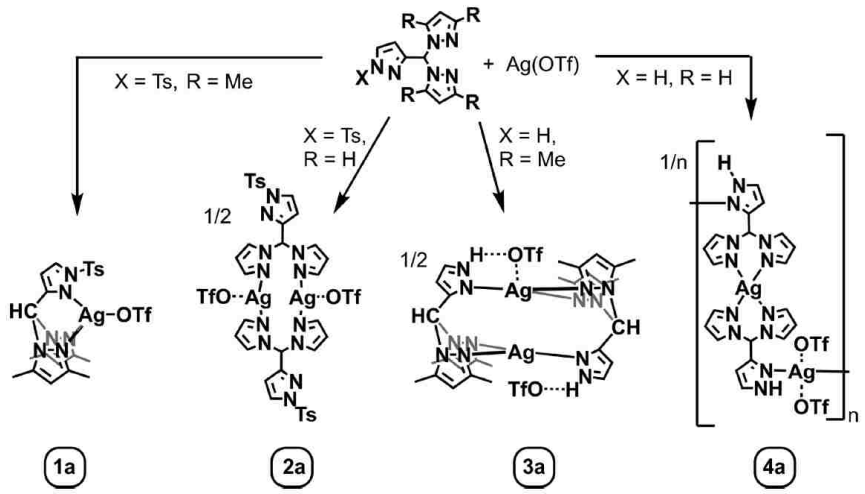

Figure 1.12: Summary of the Solid-State Coordination Behavior of 1:1 ^{x}L/Ag(OTf) Complexes. Figure is taken from reference 20.

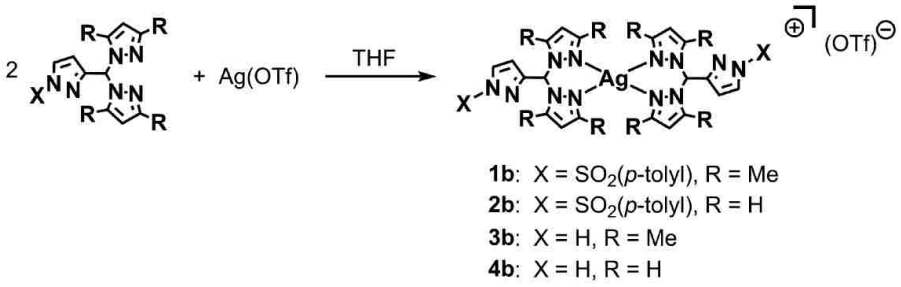

Figure 1.13: Preparation and labeling of 2:1 ^{x}L/Ag(OTf) Complexes. Figure is taken from reference 20.

The new silver complexes were used to catalyze nitrene transfer reaction between styrene, N-tosylamine, and a hypervalent iodine reagent, $PhI(OAc)_2$ at 2 mol % catalyst loading in acetonitrile. Table1.3 summarizes the results of the catalysis reaction. 1b gave the highest aziridine yield followed by 1a ≈ 2a and then 3a. The other new silver catalysts performed similarly to control experiments that show molecular sieves alone have some catalytic ability under these conditions (16 h at 80˚C). The aziridination reaction did not occur at room temperature, in methylene chloride, or even when using preformed

PhI=NTs (as used in other silver catalyzed aziridination reactions). A small amount (1-2 %) of a statistical diastereomeric mixture of 2,4-diphenyl-N-tosylpyrrolidine (B, Table 1.3) was also observed in the cases where catalysis was successful. This transformation has never been reported with a silver(I) catalyst before.

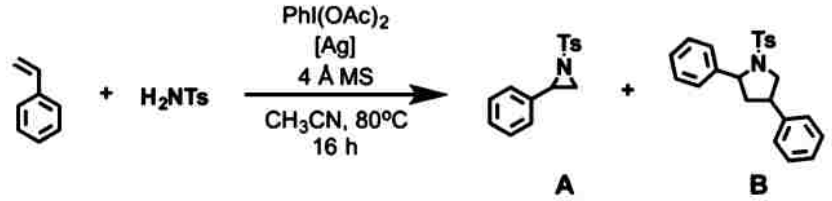

entry	[Ag]	NMR yield of A	% yield of A[b]	% yield of B[b]	TON[c]
1	none	3 (2)	0	0	0
2	AgOTf	3 (2)	0	0	0
3	1a	17 (6)	18 (5)	2.2 (0.1)	10
4	1b	34 (4)	27 (3)	2 (1)	15
5	1b[d]	27 (3)			
6	2a	16 (8)	10 (2)	2.1 (0.5)	11
7	2a[e]	trace			
8	2b	6 (2)	8 (2)	0	4
9	3a	15 (3)	12 (4)	1 (0.2)	7
10	3b	6 (1)			
11	4a	8 (2)	2	0	1
12	4b[d]	6 (1)			

Table 1.3: Summary of results from Nitrene-Transfer Reactions[a]. Table is taken from reference 20.

[a] Conditions: 5mmol of styrene, 1mmol of $PhI(OAc)_2$, 1mmol of H_2NTs, 0.02 mmol of [Ag], 0.5g of 4 Å molecular sieves, 4mL of CH_3CN, 16 h, 80˚C. [b]Isolated yields based on H_2NTs; average of three runs (average deviation in parentheses). [c]TON= mmol (A+B, isolated)/ mmol [Ag]. [d]In situ. [e]Room temperature, 16 h.[20]

For the very first time, silver(I) C-scorpionates were used as nitrene transfer catalysts in the aziridination of styrene in CH_3CN using H_2NTs and $PhI(OAc)_2$ as an oxidant. The new silver complexes with the bulkiest derivative, $[Ag(^{Ts}L^*)_2](OTf)$ was proved to be a better catalyst than the $[Ag(^{Ts}L^*)](OTf)$ and the rest of the catalysts that

were tested. This result contradicts the previously reported results where catalytic activity is favored when silver adopts lower coordination numbers. However, these silver complexes show lower activity for catalytic aziridination compared to the previously reported $AgTp^x$ complexes. The purpose of this thesis work is to fully investigate if by further increasing the steric bulk on the pyrazolyls these current catalysts can be made more competitive with other previously reported catalysts for intermolecular aziridination reactions.

The second chapter of this thesis describes initial research on the solution and solid-state properties of the iron(II) N-confused C-scorpionate complex, $[Fe(^{H}L^{*})_2](OTf)_2$, that served as synthetic training and was aimed at completing work of a previous group member, Kristin Meise, M.S. Kristin had found that this iron(II) complex crystallized in different forms in from either methanol or acetonitrile solutions and that each form had unusual magnetic switching/ spin crossover (SCO) behavior. She worked extensively on the chemistry in methanol but the work with acetonitrile remained mostly incomplete. Thus, this chapter fully details my efforts toward a completed study of the solution equilibrium that controls much of the crystallization behavior of this compound. The structures of five of the six different crystal forms and the magnetic properties of the compounds are described; Kristin had previously described only two crystal forms, co-1 and cis-1 from this solvent. This work was submitted to the journal *Inorganic Chemistry* and the final revision is currently under review.

The third chapter describes the preparation of two new N-confused C-scorpionates, $^{Ts}L^{ipr}$ and $^{H}L^{ipr}$, each with two 'normal' 3,5-diisopropylpyrazolyl groups, and either an N-tosyl or N-H group on the 'confused' pz. Also, described in this chapter

are the preparation of the silver complexes of these bulky ligands and their potential as catalysts for nitrene transfer reactions. The final chapter will be the conclusion and details future work for the synthesis of a binuclear copper complex in order to develop even better catalysts for nitrene transfer reactions.

CHAPTER 2: SELECTIVE ISOMER FORMATION AND CRYSTALLIZATION-DIRECTED MAGNETIC BEHAVIOR IN NITROGEN-CONFUSED *C*-SCORPIONATE COMPLEXES OF FE(O_3SCF_3)$_2$

2.1. INTRODUCTION

Transition metal complexes that have metal centers with d^4 to d^7 electron configurations and ligands that impart intermediate fields to the metal can be provoked to undergo reversible spin crossover (SCO)[21,22] between low spin (LS) and high spin (HS) electronic states via controlled perturbations to temperature, applied pressure, or various forms of electromagnetic radiation.[23-31] Since a given SCO complex in each of its electronic spin states exhibits different size, color, magnetic properties, and bulk solid-state electrical resistivity, there has been great interest in their potential employment for various technological applications.[32-40] The temperature dependence of bulk molar magnetic susceptibility (χ_M) is most often used to characterize SCO behavior since it is simple to measure and because χ_M directly correlates to the high spin fraction (γ_{HS}) in the sample. The temperature with $\gamma_{HS} = 0.5$, or $T_{1/2}$, is generally used as a descriptive reference. The full χ_M versus T plots reveal whether or not the SCO is complete, if SCO occurs in one or more steps, and whether there is cooperativity in the form of either a large $\delta\chi_M/dT$ or a hysteresis (where $T_{1/2}\uparrow$ (heating) is different than $T_{1/2}\downarrow$ (cooling)), or both.[41] The requisite conditions (T, P, $h\nu$, etc.) for the initiation and progression of SCO in the solid state depends not only on the metal ion, the ligand field strength, but, critically, on the nature of crystal packing. Thus, each polymorph[42] or solvatomorph[43] of a given complex typically exhibits different magnetic behavior than its relative. A longstanding research challenge in SCO compounds is to use molecular design and/or

crystal engineering approaches to identify structure –property relationships with the goal of imparting a specific magnetic behavior ($T_{1/2}$, $\delta\chi_M/dT$, number of SCO steps, etc.) into the bulk solid.

Within the profuse collection of transition metal complexes that exhibit SCO behavior, octahedral iron(II) complexes of organoamine and/or N-heterocyclic donors represent one of the largest and most intensely studied classes.[44-49] Of these, complexes of scorpionate ligands,[50,51] poly(pyrazolyl)borates or poly(pyrazolyl)methanes (*C*-scorpionates), have received increased scrutiny because of their interesting SCO behavior[52-59] and their attractive physical properties that are useful for materials processing.[60-67] While the SCO behavior of iron(II) scorpionates has shown some evidence of tunability via ligand modifications,[68-72] there is a need for elaboration in order to more fully understand the impact of substituent changes on fine-tuning ligand field strength and crystal packing, and, hence, controlling SCO behavior in this class of compounds.

We recently introduced a new class of C-scorpionate, the nitrogen-confused C-scorpionate, where the connectivity of one of the three heterocycles bound to the central methine carbon occurs at the 3-carbon ring position instead of the more usual N-1 position. The iron(II) complexes $[Fe(^{H}L)_2](X)_2$ (X = BF_4,[73] OTf[74]), where ^{H}L is a ligand with two unsubstituted pyrazolyls and a 'confused' pyrazolyl with an N-H moiety, were studied. Both complexes are low spin (LS) at room temperature and undergo SCO with $T_{1/2}$ near 360 K but the triflate (OTf) derivative exhibited a more cooperative SCO than the BF_4 derivative due to stronger intermolecular charge-assisted hydrogen bonding interactions between the pyrazolyl-NH donor and anion acceptor (O versus F). It is

known for iron(II) complexes of normal scorpionates that introducing methyl substituents at the 3-pyrazolyl ring positions dramatically reduces $T_{1/2}$ of SCO presumably because interligand steric interactions of six methyl groups near the metal center favor the longer bond distances associated with the HS state. For instance, $\{Fe[HC(3,5\text{-}Me_2pz)_3 = Tpm^*]_2\}(BF_4)_2$ has $T_{1/2}$ near 200 K[75] while $\{Fe[HC(pz)_3 = Tpm]\}(BF_4)_2$ has $T_{1/2}$ near 400 K.[76] Lowering the number of methyls at the 3-pyrazolyl positon gives $T_{1/2}$ between these two extremes as in the cases of $[Fe\{HC(3\text{-}Mepz)_2(5\text{-}Mepz)\}_2](BF_4)_2$ ($T_{1/2}$ = 250 K)[77] or $[Fe(Tpm^*)(Tpm)](BF_4)_2$ ($T_{1/2}$ (polymorph 1) ~ 228 K; $T_{1/2}$ (polymorph 2) ~ 310 K).[78] Given these results and the current interest in discovering new examples of species that undergo thermal SCO with $T_{1/2}$ near room temperature,[79] we initiated a study of the SCO behavior of iron(II) complexes of $^{H}L^*$, a N-confused C-scorpionate ligand with two 3,5-dimethylpyrazolyl rings and an unsubstituted 'confused' pyrazolyl; such complexes would have four methyl groups near the metal center. During the course of these studies, we discovered that the iron(II) triflate complex showed unexpectedly rich structural chemistry that was responsible for the unusual thermal SCO behavior as evaluated by magnetometry measurements. This chapter details the coordination chemistry, crystallization behavior, and resultant magnetic properties of $[Fe(^{H}L^*)_2](OTf)_2 \cdot xCH_3CN$, **1**$\cdot xCH_3CN$, where x = 0, 1, 2, or 4.

2.2. EXPERIMENTAL

General Considerations. Commercial solvents were dried by conventional means and distilled under a nitrogen atmosphere prior to use. Anhydrous $Fe(OTf)_2$ was purchased from commercial sources and was purified by low temperature crystallization from CH_3CN/Et_2O to give $Fe(OTf)\cdot 2CH_3CN$ that was stored under argon in a drybox.[74a] The

compound ^{H}L* was prepared as described elsewhere.[74b] The iron(II) complex was prepared under argon using Schlenk line techniques, however, after isolation, it was stored and manipulated under normal laboratory atmospheric conditions.

Instrumentation. Midwest MicroLab, LLC, Indianapolis, IN, performed all elemental analyses. Melting point determinations were made on samples contained in glass capillaries using an Electrothermal 9100 apparatus and are uncorrected. IR spectra were recorded for samples as KBr pellets in the 4000-500 cm^{-1} region on a Nicolet Magna-IR 560 spectrometer or on solid samples using a Thermo Scientific Nicolet iS5 IR spectrometer equipped with an iD3 Attenuated Total Reflection (ATR) accessory. ^{1}H NMR spectra were recorded on a Varian 400 MHz spectrometer. Chemical shifts were referenced to residual CD_2HCN resonance[80] at δ_H 1.94 for CD_3CN. Solution magnetic moments were measured by the Evans method.[81] Magnetic susceptibility data were collected on a Quantum Design MPMS3 SQUID magnetometer. Raw moment data were corrected for sample shape and radial offset corrections using the MPMS 3 Sample Geometry Simulator.[82] Diamagnetic corrections of -372×10^{-6} emu/mol for each *trans*-**1**, *cis*-**1**, and *co*-**1** calculated from tabulated Pascal's constants[83] were applied to the measured susceptibility data, as appropriate. Electronic absorption (UV-Vis/NIR) measurements were made on a Cary 5000 instrument. Powder X-ray diffraction patterns were collected with an Oxford Diffraction Ltd. Supernova equipped with a 135 mm Atlas CCD detector or with a Rigaku Miniflex II instrument using Cu Kα radiation.

A. Synthetic Protocol.

$[Fe(^{H}L^{*})_2](OTf)_2$, **1**. A solution of 0.854 g (3.15 mmol) $^{H}L^{*}$ in 20 mL CH_3CN was added to a solution of 0.654 g (1.50 mmol) $Fe(OTf)_2 \cdot 2CH_3CN$ in 10 mL CH_3CN. The flask originally containing $^{H}L^{*}$ was washed with 5 mL CH_3CN and the washings were transferred to the reaction medium to ensure quantitative transfer of reagent. After the pale violet solution had been stirred 1 hr at room temperature solvent was removed under vacuum distillation with an external room-temperature water bath to facilitate evaporation. The pale lavender pink residue was washed with Et_2O (3 x 10 mL) and was dried under vacuum to leave 1.073 g (80 %) of **1** as a nearly colorless powder. Mp, did not melt below 200ºC. Anal. Calcd. (found) for **1**, $C_{30}H_{36}F_6FeN_{12}O_6S_2$: C, 40.28 (40.29); H, 4.06 (4.08); N, 18.79 (18.79). μ_{eff} (Evans, CD_3CN) = 4.9 μ_B. IR: ν_{NH} (Nujol/KBr) =3139; triflate (Nujol/KBr, s to vs): 1286 (ν_{as}, SO_3), 1256 (ν_s, CF_3), 1160 (ν_{as}, CF_3), 1033 (ν_s, SO_3), 638 (δ_s, SO_3) cm^{-1}. UV-vis [CD_3CN] λ, nm (ε, $M^{-1}cm^{-1}$): 800 (20), 467 sh (90), 374 sh (280), 338 (600), 320 (640). See below for ^1H NMR data.

cis-$[Fe(^{H}L^{*})_2](OTf)_2$, *cis*-**1**. This isomer has not yet been obtained pure in bulk form. Greatest amounts of this isomer as a powder admixed with small amounts of *trans*-**1** are obtained by boiling a CH_3CN solution of **1** to dryness with the aid of an external 90ºC oil bath (see Figure 2.1 for PXRD and 2.2 for NMR).

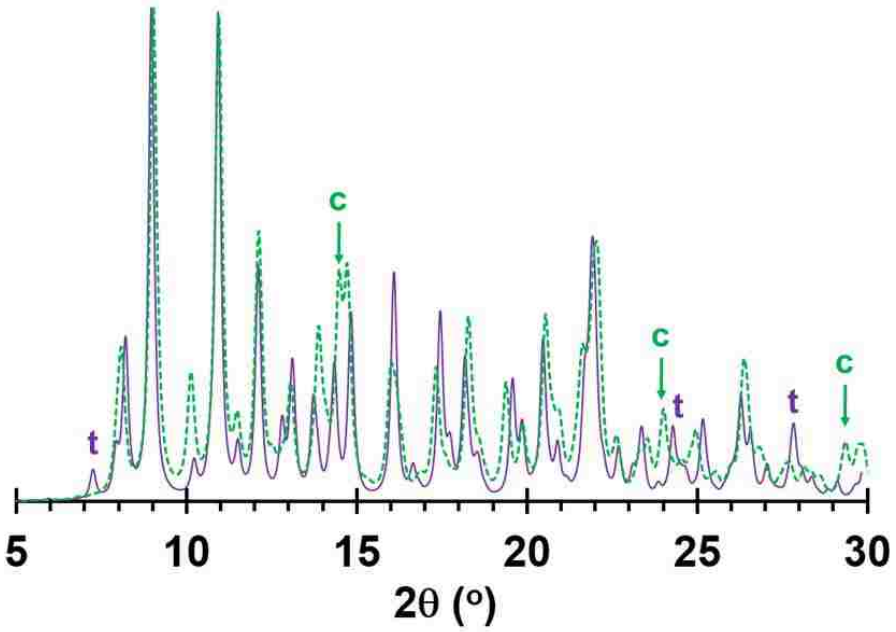

(a)

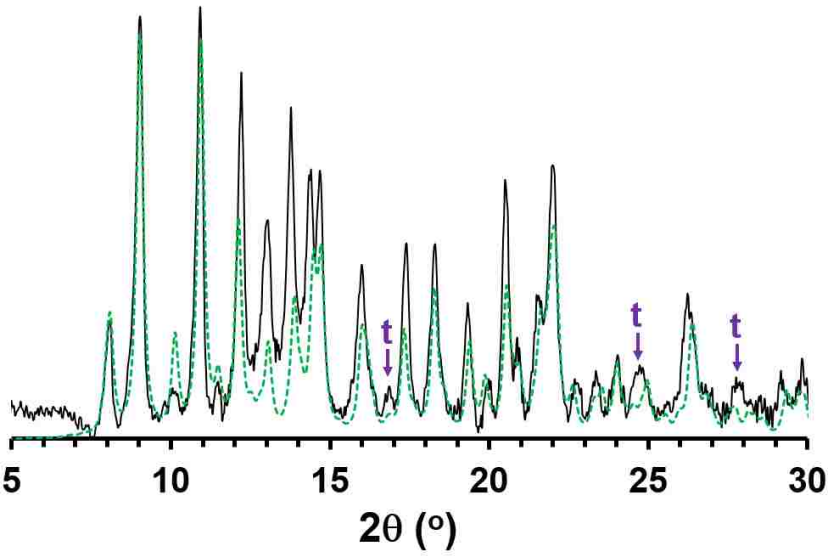

(b)

Figure 2.1 (a) Comparison of PXRD diffractograms calculated from single crystal diffraction data acquired at 250 K of trans-**1** (purple) and cis-**1** (green dashed line) where the reflections that can most easily be used to identify the respective isomers are labeled 't' or 'c'. **(b)** Experimental PXRD pattern (black) obtained for residue left after boiling a CH_3CN solution of 1 to dryness. The calculated PXRD pattern for cis-**1** (green dashed lines) is shown and peaks characteristic of trans-**1** are demarcated with a 't'.

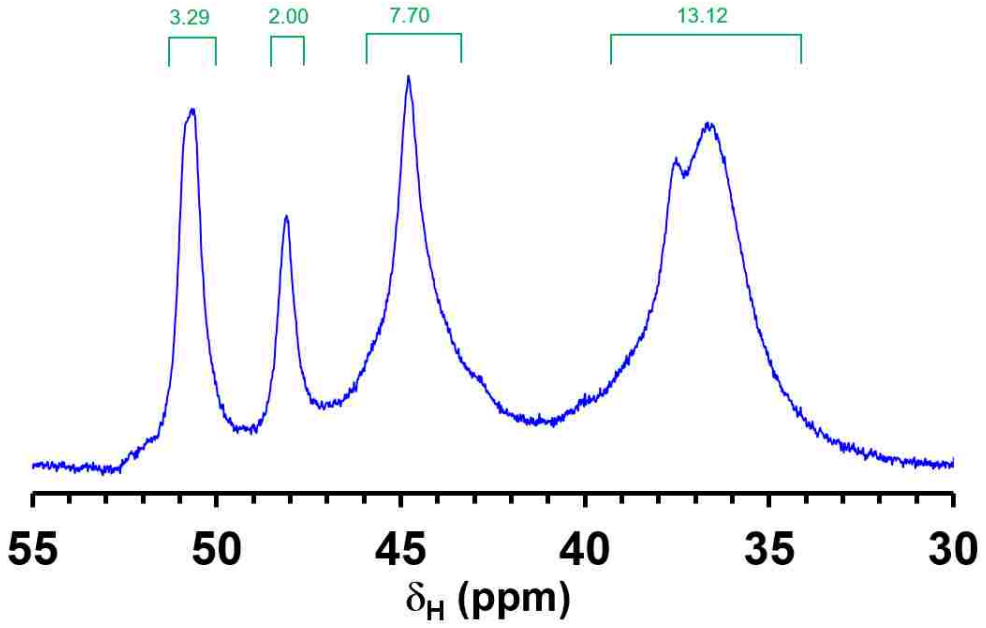

Figure 2.2. Downfield portion of the ^{1}H NMR spectrum of the residue obtained by boiling a solution of 1 in CH_3CN to dryness with an external oil bath at 90°C. PXRD of sample was shown in Figure 2.1b.

Single crystals of *cis*-**1** could be selected (at random) from mixtures with *trans*-**1** (see below) and analyzed by single crystal x-ray diffraction (scXRD), as follows. Room temperature vapor diffusion of Et_2O into a filtered 0.025 M CH_3CN solutions of **1** gave colorless plate-like needles which are a mixture of isomers, *trans*-**1** and *cis*-**1**. One of the latter was hand-selected and used for scXRD. The bulk colorless needle crystals were collected by decanting the mother liquor, washing with Et_2O, and drying under vacuum 20 min. ^{1}H NMR (CD_3CN) analysis confirms the bulk crystals to be a mixture of isomers (see Figure 2.3). The resonances attributed to the *cis*- isomer are: δ_H 50.7 (2 H), 48.0 (2 H), 44.8 (2 H), 44.2 (6 H), 35.6 (4 H), 21.5 (6 H), 20.3 (6 H), 19.3 (6 H), -41.6 (2 H) ppm.

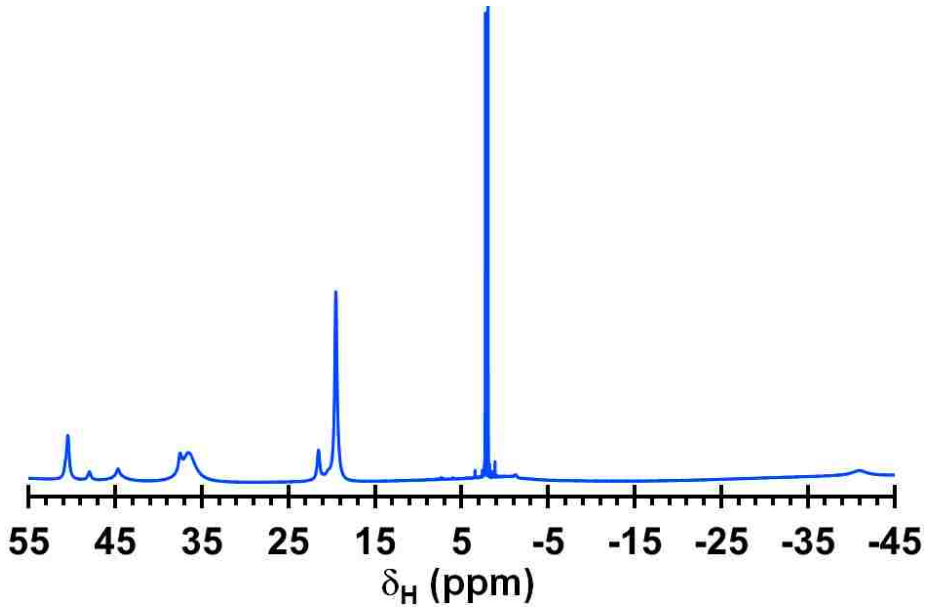

Figure 2.3. ^{1}H NMR (CD_3CN, 295 K) spectrum of bulk filtered and vacuum dried crystals from room vapor diffusion of Et_2O into a CH_3CN solution of **1**.

co-[Fe(^{H}L*)$_2$](OTf)$_2$, *co*-**1**. Crystallization by cooling a hot (60ºC) CH_3CN solution of **1** (200 mg/ 1 mL CH_3CN, ca. 0.22 M) to room temperature overnight gave 52 mg large, pale blue-green block-like prisms of *co*-**1**. An additional 47 mg fraction was obtained by evaporating the mother liquor to ½ volume by heating to 60ºC under a nitrogen stream, then allowing the mother liquor to cool to room temperature 2 h, then cool at 4ºC for 12 h, followed by decantation and drying under nitrogen. A final crop of 20 mg crystals was obtained by concentrating and cooling a second time as above. Anal. Calcd. (found) for *co*-**1**, $C_{30}H_{36}F_6FeN_{12}O_6S_2$: C, 40.28 (40.07); H, 4.06 (4.04); N, 18.79 (18.66). ^{1}H NMR (CD_3CN) δ_H 50.7, 50.5, 48.0, 44.7, 44.2, 37.5, 36.6, 35.6, 21.5, 20.4, 19.6, 19.3, 2.22, -41.0, -41.7 ppm.

trans-[Fe(^{H}L*)$_2$(CH_3CN)$_x$](OTf)$_2$·xCH_3CN (x = 1, 2, or 4), *trans*-**1**·xCH_3CN (x = 1, 2, or 4). A solution of 500 mg **1** in 7 mL CH_3CN was placed in a freezer at -20ºC and the

solution became light violet on cooling. Large violet square plates of *trans*-**1**·2CH_3CN formed over 14 h. The violet crystals of *trans*-**1**·2CH_3CN (251 mg) were separated from the mother liquor by decanting and drying under an N_2 stream. Evaporation of the mother liquor to about 1/3 volume and cooling another 14 h gave a second crop (42 mg) of *trans*-**1**·2CH_3CN. Total: 293 mg *trans*-**1**·2CH_3CN. Note: if any trace colorless powder of *trans*-**1**·4CH_3CN is present in the bulk crystallization, it can be removed by shaking and decanting the cold suspension from the larger violet crystals. Then after drying under a nitrogen stream, the violet crystals of di-solvate are then separated mechanically from any opaque, pale aqua crystals of the (now desolvated) tetrasolvate. Longer crystallization times (4 -7 d) or more dilute solutions produced a mixture of *trans*-**1**·2CH_3CN and colorless prisms of *trans*-**1**·4CH_3CN. If the crystallization time is extended to 2 weeks or more then the violet crystals transform completely into colorless prisms of *trans*-**1**·4CH_3CN. The crystals of *trans*-**1**·4CH_3CN rapidly desolvate under a N_2 stream to give approximately 45 mg of desolvated *trans*-**1** per 100 mg of **1**. The following ^{1}H NMR data are for violet *trans*-**1**·2CH_3CN. ^{1}H NMR (CD_3CN, 295 K) δ_H 50.5 (4 H), 37.5 (2 H), 36.6 (12 H), 19.5 (16 H), 2.22 (6 H), -41.0 (2 H) ppm.

Samples of **1**·2CH_3CN desolvate to **1**·CH_3CN during shipping to combustion analysis laboratory. Samples of **1**·CH_3CN can be prepared intentionally by subjecting **1**·2CH_3CN to oil pump vacuum (0.1 mtorr) at room temperature 1 h. Anal. Calcd. (found) for '*trans*-**1**·CH_3CN', $C_{32}H_{39}F_6FeN_{13}O_6S_2$: C, 41.07 (41.31); H, 4.20 (4.29); N, 19.46 (19.70).

trans-[Fe(^{H}L*)$_2$](OTf)$_2$, *trans*-**1**. *Method A*. A 100 mg (0.102 mmol) sample of *trans*-**1**·2CH_3CN dissolved in 2 mL CH_3CN at room temperature (avoid heating) is immediately precipitated with 6 mL Et_2O. The colorless powder 81 mg (0.091 mmol, 89

%) is collected after filtration and drying under a nitrogen stream. *Method B*. A sample of 65 mg (0.067 mmol) *trans*-**1**·2CH_3CN is heated at 70ºC 4 h under vacuum to give 46 mg (0.051 mmol, 76 %) *trans*-**1** as a colorless powder. Anal. Calcd. (found) for '*trans*-**1**', $C_{30}H_{36}F_6FeN_{12}O_6S_2$: C, 40.28 (40.34); H, 4.06 (4.04); N, 18.79 (18.70).

B. X-ray Crystallography.

X-ray intensity data from a violet prism of *cis*-**1**, a violet needle of *trans*-**1**, a violet irregular crystal of *co*-**1**, a violet prism of *trans*-**1**·2CH_3CN and a colorless prism of *trans*-**1**·4CH_3CN were collected at 100.0(1) K with an Oxford Diffraction Ltd. Supernova equipped with a 135 mm Atlas CCD detector. The data for *trans*-**1**, *cis*-**1**, and co-**1** were also collected at 250 K (a temperature where the latter two crystals were colorless, but the former was light violet/pink). Cu Kα radiation, λ = 1.54184 Å was used for all experiments except for *trans*-**1** which used Mo Kα radiation λ = 0.71073 Å. Raw data frame integration and Lp corrections were performed with CrysAlis Pro (Oxford Diffraction, Ltd.).[84] Final unit cell parameters were determined by least-squares refinement of 18495 (100 K) and 14400 (250 K) reflections from the data sets of *cis*-**1**, of 22417 (100K) and 17127 (250 K) reflections from the data sets of *co*-**1**, 10392 (100 K) reflections from data set of *trans*-**1**·2CH_3CN and 13813 (100 K) reflections from data set of *trans*-**1**·4CH_3CN, 15651 (100 K) and 10071 (250 K) reflections from the data sets of *trans*-**1**, with $I > 2\sigma(I)$ for all cases. Analysis of the data showed negligible crystal decay during collection in each case. Direct methods structure solutions were performed with Olex2.solve[85] while difference Fourier calculations and full-matrix least-squares refinements against F2 were performed with SHELXTL.[86] Empirical absorption

corrections were applied using spherical harmonics implemented in the SCALE3 ABSPACK scaling algorithm. The hydrogen atom bound to nitrogen of the pyrazol-3-yl group in *cis*-**1**, *trans*-**1** (100 K), and *trans*-**1**·2 CH_3CN were located and refined. All other hydrogen atoms were placed in idealized positions and included as riding atoms. The X-ray crystallographic parameters and further details of data collection and structure refinements are given in table 2.1.

Special Details: For *cis*-**1**, one of the triflate anions is well ordered while the other is unequally disordered 67%:33% over two nearby positions. At high temperature the extreme disorder causes an A-level alert in the checkcif program; this alert is resolved in the 100 K structure. Also a modulated phase with q-vector (0.077 0 0.171) was found at 100 K; no satellites were detected at 250 K. For *co*-**1**, one of the triflate ions is disordered over two nearby positons. The major component (84%) is hydrogen bonded to the pyrazolyl. The minor component occupies an alternative position in a cavity. The content of the cavity could not be elucidated but may involve small amount of unidentified solvent and/or a third orientation of the anion. The crystal of *trans*-**1** at 100 K was a twin where component two is rotated 180° around [-0.01 -0.02 1.00] (reciprocal space) or [0.00 0.00 1.00] (direct space). The crystal of *trans*-**1**·2 CH_3CN was an 87/8/5 triplet where component 2 was rotated by -170.9° around [-0.05 1.00 -0.01] (reciprocal space) or [-0.05 1.00 -0.02] (direct space) while component 3 was rotated by -174.6° around [-0.02 1.00 0.00] (reciprocal space) or [-0.01 1.00 -0.00] (direct space).

Table 2.1. Crystal data and structure refinement for *trans*-**1**·2CH_3CN and *trans*-**1**·4CH_3CN.

Identification code	*trans*-**1**·2CH_3CN	*trans*-**1**·4CH_3CN
Empirical formula	$C_{34}H_{42}F_6FeN_{14}O_6S_2$	$C_{38}H_{48}F_6FeN_{16}O_6S_2$
Formula weight	976.78	1058.89
Temperature/K	100.15(10)	100.15(10)
Crystal system	monoclinic	monoclinic
Space group	$P2_1/c$	$P2_1/n$
a/Å	13.1862(2)	10.29427(7)
b/Å	11.62430(13)	10.25787(7)
c/Å	14.3231(2)	22.46703(18)
α/°	90	90
β/°	101.7586(15)	95.8748(7)
γ/°	90	90
Volume/Å^3	2149.38(5)	2359.99(3)
Z	2	2
ρ_{calc}g/cm^3	1.509	1.490
μ/mm^{-1}	4.490	4.150
F(000)	1008.0	1096.0
Crystal size/mm^3	0.257 × 0.233 × 0.129	0.365 × 0.268 × 0.18
Radiation	CuKα (λ = 1.54184)	CuKα (λ = 1.54184)
2Θ range for data collection/°	6.848 to 141.128	7.912 to 141.296
Index ranges	-16 ≤ h ≤ 14, -14 ≤ k ≤ 14, -17 ≤ l ≤ 17	-12 ≤ h ≤ 12, -12 ≤ k ≤ 12, -27 ≤ l ≤ 23
Reflections collected	20304	22365
Independent reflections	4080 [R_{int} = 0.0323, R_{sigma} = 0.0168]	4468 [R_{int} = 0.0223, R_{sigma} = 0.0144]
Data/restraints/parameters	4080/12/334	4468/0/319
Goodness-of-fit on F^2	1.114	1.069
Final R indexes [I ≥ 2σ (I)]	R_1 = 0.0389, wR_2 = 0.1164	R_1 = 0.0263, wR_2 = 0.0690
Final R indexes [all data]	R_1 = 0.0416, wR_2 = 0.1182	R_1 = 0.0273, wR_2 = 0.0700
Largest diff. peak/hole / e Å^{-3}	0.62/-0.57	0.23/-0.41

Table 2.1, contd. Crystal data and structure refinement for *cis*-**1**·at 250 and 100 K.

Identification code	*cis*-**1** (250 K)	*cis*-**1** (100 K)
Empirical formula	$C_{30}H_{36}F_6FeN_{12}O_6S_2$	$C_{30}H_{36}F_6FeN_{12}O_6S_2$
Formula weight	894.68	894.68
Temperature/K	250.00(14)	100.1(6)
Crystal system	monoclinic	monoclinic
Space group	$P2_1/c$	$P2_1/c$
a/Å	12.9325(3)	12.78177(10)
b/Å	21.3789(4)	21.02035(20)
c/Å	14.7731(3)	14.74699(12)
α/°	90.00	90.00
β/°	103.050(2)	103.0849(8)
γ/°	90.00	90.00
Volume/Å^3	3979.02(15)	3859.30(6)
Z	4	4
ρ_{calc}g/cm^3	1.493	1.540
μ/mm^{-1}	4.780	4.928
F(000)	1840.0	1840.0
Crystal size/mm^3	0.383 × 0.233 × 0.144	0.383 × 0.233 × 0.144
Radiation	CuKα (λ = 1.54184)	CuKα (λ = 1.54184)
2Θ range for data collection/°	7.02 to 149.22	7.1 to 148.28
Index ranges	-15 ≤ h ≤ 16, -26 ≤ k ≤ 26, -18 ≤ l ≤ 18	-15 ≤ h ≤ 15, -25 ≤ k ≤ 25, -18 ≤ l ≤ 18
Reflections collected	36060	37282
Independent reflections	7971 [R_{int} = 0.0424, R_{sigma} = 0.0312]	7739 [R_{int} = 0.0279, R_{sigma} = 0.0191]
Data/restraints/parameters	7971/143/603	7739/95/603
Goodness-of-fit on F^2	1.098	1.034
Final R indexes [I ≥ 2σ (I)]	R_1 = 0.0517, wR_2 = 0.1398	R_1 = 0.0360, wR_2 = 0.0928
Final R indexes [all data]	R_1 = 0.0651, wR_2 = 0.1650	R_1 = 0.0396, wR_2 = 0.0958
Largest diff. peak/hole / e Å^{-3}	0.47/-0.56	0.36/-0.48

Table 2.1, contd. Crystal data and structure refinement for *trans*-**1**·at 250 and 100 K.

Identification code	*trans*-**1** (250 K)	*trans*-**1** (100 K)
Empirical formula	$C_{30}H_{36}F_6FeN_{12}O_6S_2$	$C_{30}H_{36}F_6FeN_{12}O_6S_2$
Formula weight	894.68	894.68
Temperature/K	250.00(14)	100.1(6)
Crystal system	monoclinic	triclinic
Space group	$P2_1/c$	P-1
a/Å	14.8018(7)	12.9592(3)
b/Å	21.0660(10)	14.6378(4)
c/Å	13.0878(6)	20.8275(4)
α/°	90.00	91.421(2)
β/°	103.434(5)	90.536(2)
γ/°	90.00	103.016(2)
Volume/Å^3	3969.3(3)	3847.71(16)
Z	4	4
ρ_{calc}g/cm^3	1.497	1.544
μ/mm^{-1}	0.570	0.588
F(000)	1840.0	1840.0
Crystal size/mm^3	0.746 × 0.171 × 0.083	0.715 × 0.137 × 0.068
Radiation	MoKα (λ = 0.71073)	MoKα (λ = 0.71073)
2Θ range for data collection/°	6.626 to 59.338	6.442 to 57.45
Index ranges	-20 ≤ h ≤ 18, -29 ≤ k ≤ 28, -18 ≤ l ≤ 17	-17 ≤ h ≤ 17, -18 ≤ k ≤ 18, -26 ≤ l ≤ 28
Reflections collected	45285	32057
Independent reflections	10168 [R_{int} = 0.0487, R_{sigma} = 0.0450]	32057 [R_{int} = ?, R_{sigma} = 0.0572]
Data/restraints/parameters	10168/19/525	32057/95/1139
Goodness-of-fit on F^2	1.052	1.013
Final R indexes [I ≥ 2σ (I)]	R_1 = 0.0902, wR_2 = 0.2699	R_1 = 0.0587, wR_2 = 0.1592
Final R indexes [all data]	R_1 = 0.1390, wR_2 = 0.3152	R_1 = 0.0897, wR_2 = 0.1702
Largest diff. peak/hole / e Å^{-3}	1.33/-0.92	1.17/-0.70

Table 2.1, contd. Crystal data and structure refinement for *co*-**1**·at 250 and 100 K.

Identification code	*co*-**1** (250 K)	*co*-**1** (100 K)
Empirical formula	$C_{30}H_{36}F_6FeN_{12}O_6S_2$	$C_{30}H_{36}F_6FeN_{12}O_6S_2$
Formula weight	894.68	894.68
Temperature/K	250.00(14)	100.0(3)
Crystal system	monoclinic	monoclinic
Space group	I2/a	I2/a
a/Å	23.1055(3)	22.96795(18)
b/Å	13.2707(2)	13.20086(9)
c/Å	27.9530(4)	27.72924(19)
α/°	90.00	90.00
β/°	108.6125(16)	108.3556(8)
γ/°	90.00	90.00
Volume/Å^3	8122.8(2)	7979.65(10)
Z	8	8
ρ_{calc}g/cm^3	1.463	1.489
μ/mm^{-1}	4.683	4.767
F(000)	3680.0	3680.0
Crystal size/mm^3	0.39 × 0.356 × 0.208	0.39 × 0.356 × 0.208
Radiation	CuKα (λ = 1.54184)	CuKα (λ = 1.54184)
2Θ range for data collection/°	7.46 to 148.12	7.5 to 148.3
Index ranges	-22 ≤ h ≤ 28, -13 ≤ k ≤ 16, -34 ≤ l ≤ 34	-28 ≤ h ≤ 23, -16 ≤ k ≤ 16, -34 ≤ l ≤ 34
Reflections collected	29314	38795
Independent reflections	8118 [R_{int} = 0.0332, R_{sigma} = 0.0239]	8025 [R_{int} = 0.0277, R_{sigma} = 0.0180]
Data/restraints/parameters	8118/19/524	8025/38/557
Goodness-of-fit on F^2	1.053	1.060
Final R indexes [I ≥ 2σ (I)]	R_1 = 0.0498, wR_2 = 0.1474	R_1 = 0.0703, wR_2 = 0.1988
Final R indexes [all data]	R_1 = 0.0509, wR_2 = 0.1492	R_1 = 0.0718, wR_2 = 0.2004
Largest diff. peak/hole / e Å^{-3}	1.11/-1.00	4.16/-0.96

C. Computational details

General Considerations. Geometry optimizations were performed using Handy's optimized exchange (OPTX) with the PBE correlation (OPBE functional)[87] in combination with the def2-SV(P) double-zeta basis set for light atoms and def2-QZVPP for Fe[88] because we have previously found[89] (and find again here) that this method provides excellent agreement (within 0.09 Å) with solid state structures. Moreover, such an approach has been found to successfully determine spin-state splitting in other iron complexes that undergo spin crossover phenomena.[90] Solvent effects were accounted for by using the polarizable continuum model IEFPCM,[91] as implemented in Gaussian 16.[92] Analytical vibrational frequency calculations were carried out to verify that optimized geometries were stationary points. Table 2.2 summarizes the results of these studies.

Table 2.2. Summary of SCF energies and thermochemical data from theoretical calculations (OPBE/def2-SV(P) (C,H,N), def2-QZVPP (Fe)/PCM (CH_2Cl_2) on isomers of $[Fe(HL^*)_2]^{2+}$ in different spin states.

	trans $(HS)^{2+}$	**trans-$(LS)^{2+}$**	**cis $(HS)^{2+}$**	**cis-$(LS)^{2+}$**
multiplicity	2	0	2	0
$<S^2>$	6.0198/6.0001	--	6.0148/6.0000	--
E_{tot}(hartree)	-3007.348894	-3007.375467	-3007.449739	-3007.375816
E_{298} (hartree)	-3006.781387	-3006.784702	-3006.781102	-3006.783612
E_o E_{tot}+ZPE(hartree)	-3006.821965	-3006.822503	-3006.821744	-3006.821580
H_{298} (hartree)	-3006.780443	-3006.783758	-3006.780158	-3006.782668
G_{298} (hartree)	-3006.895477	-3006.887389	-3006.894910	-3006.886487

2.3 RESULTS AND DISCUSSION

The reaction between $Fe(OTf)_2$ and two equivalents of $^{H}L^*$ in CH_3CN gives the desired complex $[Fe(^{H}L^*)_2](OTf)_2$, **1**, in high yield. Recrystallization of **1** under different

conditions led to the four different crystal types pictured in Figure 2.4. Recrystallization of **1** by room temperature vapor diffusion of Et_2O into CH_3CN solutions produced

Figure 2.4. Left: Photograph of the mixture of crystals obtained after recrystallization of **1** by vapor diffusion of Et_2O into a 0.025 M CH_3CN, filtering, and after drying under vacuum producing a mixture of large blocks of *co*-**1** and smaller plate-like needles of *cis*-**1** and *trans*-**1**. Center: Photograph of crystals of *trans*-**1**·$2CH_3CN$ obtained after cooling a CH_3CN solution of **1** to -20°C, decanting the mother liquor and (immediately) after drying under a nitrogen stream. Right: Crystals of *trans*-**1**·$4CH_3CN$ in their mother liquor. Each photograph was taken under the same magnification.

plate-like needles that are a mixture of *cis*- and *trans*- isomers, as defined by the relative disposition of the confused pyrazolyl ring on each ligand about iron's coordination sphere. The unit cell parameters of crystals of each isomer at 250 K are nearly identical, so it is very difficult to distinguish these crystals by visual inspection. The *trans*- isomer can be isolated by alternate means (vide infra). This mixture of needles was sometimes accompanied by large isometric crystalline blocks (left of Figure 2.4) that was found to contain both *cis*- and *trans*- $[Fe(^{H}L^{*})_2]^{2+}$ cations in the same unit cell, so this crystal form is referred to as *co*-**1**. Crystals of *co*-**1** are also formed predominantly in a mixture along with smaller amounts of plate-like needle mixtures of *trans*-**1** and *cis*-**1** by slow evaporation of CH_3CN solutions of **1**. Crystals of *co*-**1** are best isolated (giving highest quality crystals without contamination of needles) by slowly cooling hot concentrated (ca. > 0.2 M) CH_3CN solutions to room temperature or to 4°C (at the sacrifice of crystal

quality). Recrystallization of lower concentrations of **1** in CH_3CN (≤ ca. 0.10 M) at low temperature (-20 ºC) gave different CH_3CN solvates of *trans*-**1**. More specifically, when dilute solutions are placed directly in a -20 ºC freezer, violet crystals of a hydrogen-bonded bis-acetonitrile solvate *trans*-$[Fe(^{H}L^*)_2](OTf)_2 \cdot 2CH_3CN$, *trans*-**1**$\cdot 2CH_3CN$, form (Figure 2.4, center) after about 1 d, followed by colorless block-like prisms of the tetrasolvate, *trans*-**1**$\cdot 4CH_3CN$ (Figure 2.4, right). If crystallization chambers are left for extended periods (2 weeks to 1 month) the initially formed violet crystals eventually transform to colorless *trans*-**1**$\cdot 4CH_3CN$. Alternatively, when more dilute (< 0.02 M) solutions are cooled in a -20ºC freezer, the resulting crystal mixture is composed mainly of *trans*-**1**$\cdot 4CH_3CN$ with minor amounts of the disolvate. If crystals of *trans*-**1**$\cdot x CH_3CN$ (x = 2, 4) are subject to recrystallization by vapor diffusion of Et_2O into CH_3CN solutions at 4ºC, then a mixture of *trans*-**1** and *trans*-**1**$\cdot 2CH_3CN$ is obtained.

A. Solid State Structures.

Crystals of *trans*-**1**$\cdot$x CH_3CN (x = 2 or 4) maintained their color over the temperature range of 298 to 100 K while *trans*-**1**, *cis*-**1** and *co*-**1** changed from colorless at room temperature to violet at 100 K. Thus, the crystal structures of the former two complexes were determined at 100 K while those of the latter complexes were determined at two temperatures (250 K (colorless) and 100 K (violet)). The structures of the *trans*-**1**$\cdot x CH_3CN$ solvates (x = 2 or 4) will be described briefly first, then the structures of the other compounds are described in more detail because unusual features of their crystal packing dictate their peculiar magnetic behavior.

Views of the structure of *trans*-**1**·2CH_3CN are shown in Figure 2.5 while selected bond distances and angles are listed in Table 2.3. The asymmetric unit consists of an iron(II) ion located on an

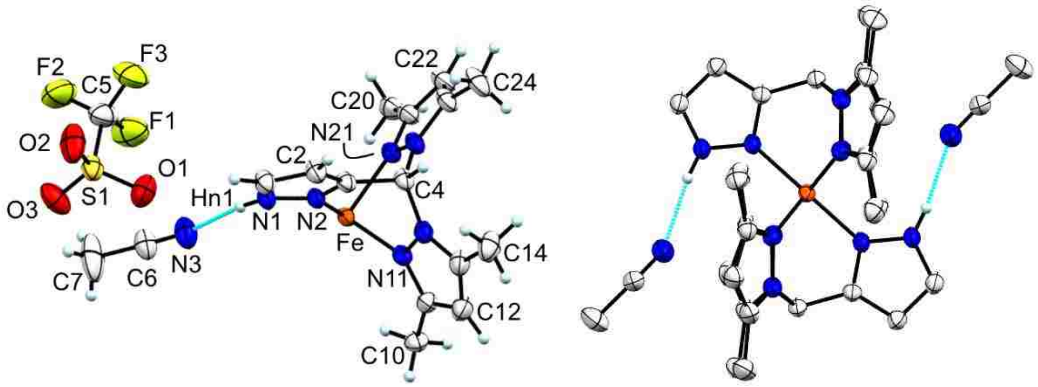

Figure 2.5. Left: Asymmetric unit of *trans*-**1**·2CH_3CN, minor disorder component of anion and solvate atoms omitted for clarity. Thermal ellipsoids are shown at 50% probability. Right: View of the dication showing trans- disposition of the 'confused' pyrazolyls, with most hydrogen atoms omitted for clarity.

Table 2.3. Selected bond distances (Å), angles (°), and torsions (°) for *trans*-**1**·xCH_3CN (x = 2, 4).

Bond distances (Å)	**1**·2CH_3CN	**1**·4CH_3CN
Fe-N2	1.9364(17)	2.1297(10)
Fe-N11	1.9908(18)	2.1799(11)
Fe-N21	1.9964(16)	2.2147(11)
N1-H1n	0.86(3)	0.88
Bond Angles (°)		
N2-Fe-N11	87.93(6)	83.85(4)
N2-Fe-N21	87.71(6)	83.61(4)
N11-Fe-N21	86.95(7)	83.28(4)
N2 Fe1 N2'	180.00(8)	180.00(6)
N2-Fe-N11'	92.07(6)	96.15(4)
N11-Fe-N21'	93.05(7)	96.72(4)
Bond Torsions (°)		
FeN2-C3C4	-0.3(2)	10.15(15)
FeN11-N12C4	-1.7(2)	7.89(14)
FeN21-N22C4	-2.0(2)	12.92(14)
FeN2-C3C2	-179.47(13)	-171.42(8)
FeN11-N12C13	177.51(13)	-173.03(8)
FeN21-N22C23	176.40(13)	-161.71(8)

inversion center, one κ^3*N*-ligand, one triflate anion, and one CH_3CN molecule. The crystal symmetry gives a pseudo-octahedral FeN_6 kernel with an average Fe-N bond length of 1.97 (3) Å. This distance is characteristic of low spin (LS) iron(II) and is identical to that previously found in $[Fe(^{H}L)_2](BF_4)_2$ that possessed a dication with unsubstituted 'normal' pyrazolyls and that was shown to be 100% LS iron(II) by magnetometry.[73] In the dication of *trans*-**1**·2CH_3CN, the Fe-N distance associated with the 'confused' pyrazolyl is much shorter (Fe-N2 1.936(2) Å) than those of the other two pyrazolyls (Fe-N11, 1.991(2) Å; Fe-N21 1.997(2) Å). The ligand is relatively strain-free with no discernable distortions[72] which normally manifest in pyrazolyl ring twisting (pz twist = average of the absolute value of the two torsion angles, $|FeN\text{-}NC_{methine}|$, and the corresponding confused pyrazolyl's torsion $|FeN\text{-}CC_{methine}| \geq 0^o$ (un-twisted value); here, pz twist = 1.4°) and pyrazolyl ring tilting (pz tilt = average of the two $|FeN\text{-}NC_{pz}|$ torsions and 'confused' pz ring equivalent $|FeN\text{-}C_{pz}C_{pz}|$ torsion $\leq 180^o$ (un-tilted value); here, the pz tilt = 177.8°). Finally, the 'confused' pyrazolyl N-H was located and refined (N1-H1n 0.86(3) Å) and is, somewhat surprisingly, hydrogen bonded[93] to the solvate acetonitrile [N1H1n···N3 2.03(3) Å, 172(2)°, N3···N1 2.884(3) Å] rather than to the triflate anions. The triflate anions are instead associated with acidic methine and pyrazolyl ring hydrogens[94] and with solvate methyl hydrogens on neighboring dications to give the three-dimensional supramolecular structure. The three dimensional crystal packing of *trans*-**1**·2CH_3CN is of a loosely stacked sheets held together by N-H···N and C-H···X (X = O, F) interactions listed in Table 2.4. A view of the main non-covalent interactions involved in the assembly of sheets is given in Figure 2.6 a. As indicated above, the acetonitrile solvate is hydrogen bonded to the confused pyrazolyl groups in the dication

via N1-H1n···N3 (2.03 Å). The triflate anions bridge dications to form chains that run along the *b*- axis by three charge assisted C-H···O interactions, Figure 2.6b and c. The triflate is anchored to acidic methine hydrogen of one dication (C4-H4···O2) while the other two oxygens of the triflate are in contact with a neighboring dication's confused pyrazolyl's 5-hydrogen (C1-H1···O1) and acetonitrile methyl group (C7-H7c···O3). The polymer chain is assembled into sheets along the *c*-axis by the interaction of the triflate O1 and a pyrazolyl methyl hydrogen H10c on a neighboring polymer. The *bc*-sheets are stacked loosely in the *a*-direction by weak C-H···F interactions involving the acetonitrile methyls (C7-H7a···F2) and pyrazolyl methyl groups (C22-H22···F3a), Figure 2.6d.

Table 2.4. Geometries of main N-H···N and C-H···X (X = O, F) weak hydrogen-bonding interactions in *trans*-**1**·2CH_3CN.

Donor(D)(-H)	D-H (Å)	H···A (Å)	D···A (Å)	D-H···A (°)
N1-H1n···N3	0.86(3)	2.03(3)	2.884(3)	172(3)
C1-H1···O1	0.95	2.41	3.088(3)	128
C4-H4···O2	1.00	2.34	3.283(3)	157
C7-H7c···O3	0.98	2.51	3.350(4)	144
C10-H10c···O1	0.98	2.55	3.483(3)	159
C7-H7a···F2	0.98	2.57	3.299(7)	131
C22-H22···F3a	0.95	2.45	3.152(7)	130

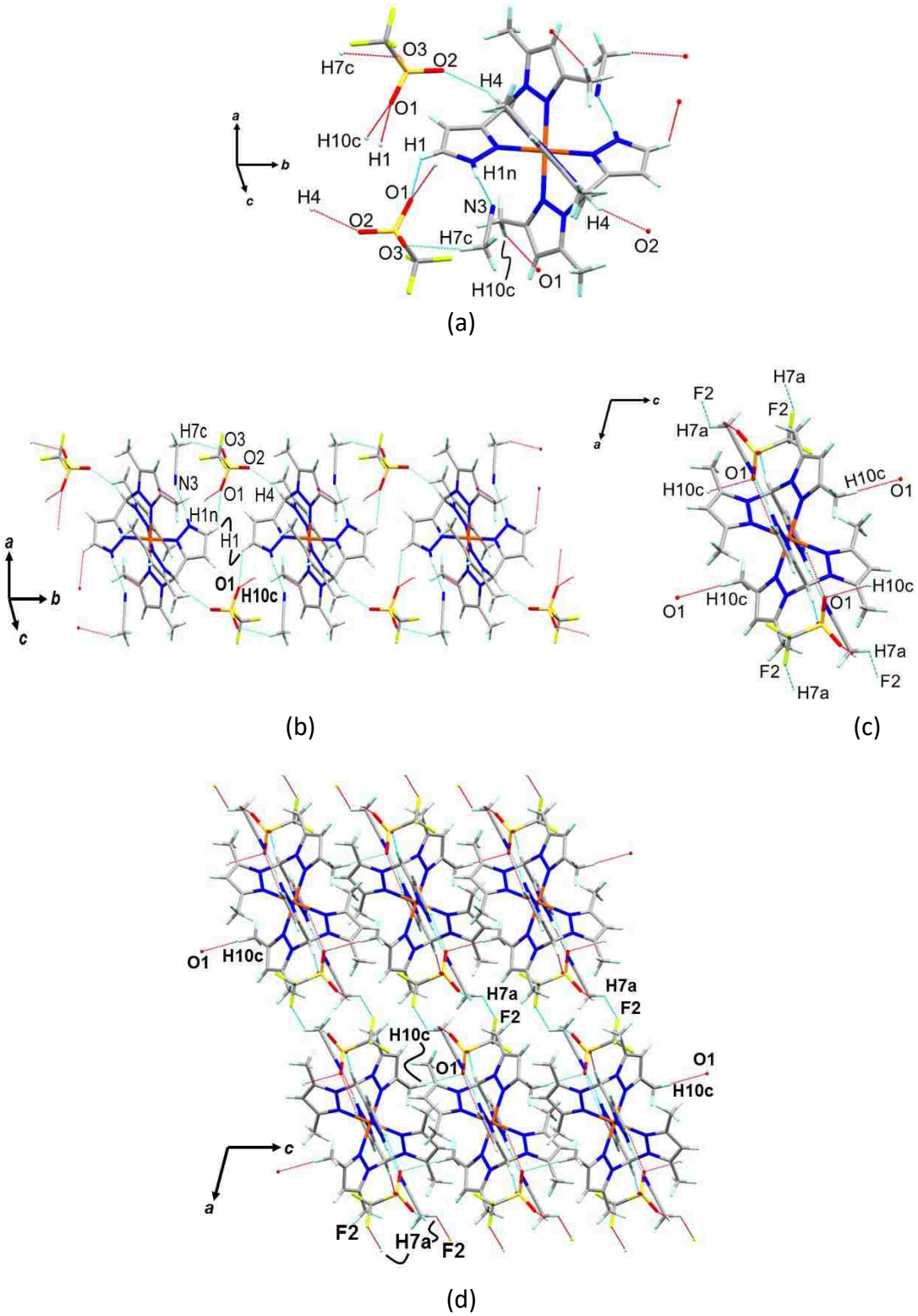

Figure 2.6. Supramolecular assembly of *trans*-**1**·2CH_3CN. (a) View of complex with intact (cyan) and dangling contacts (red). (b) Polymer chain propagating along b- axis. (c) End view of the polymer chain (down the b-axis). (d) View of two bc-sheets stacked along the a-axis by C-H···F interactions.

The structure of *trans*-**1**·4CH_3CN at 100 K contrasts that of the di-solvate in that the dication in the tetrasolvate is HS iron(II) as opposed to LS iron(II) found in the disolvate, a difference that can be attributed to the crystal packing, as described below. A comparison of bond distances and angles between the tetra- and di- solvates are found in Table 2.3. Thus, the average Fe-N distance of 2.17 Å in the tetra-solvate is characteristic for HS iron(II) versus 1.97 Å for LS iron(II) in the di-solvate. Moreover, the ligand in the tetrasolvate is significantly distorted (Figure 2.7, left) but is

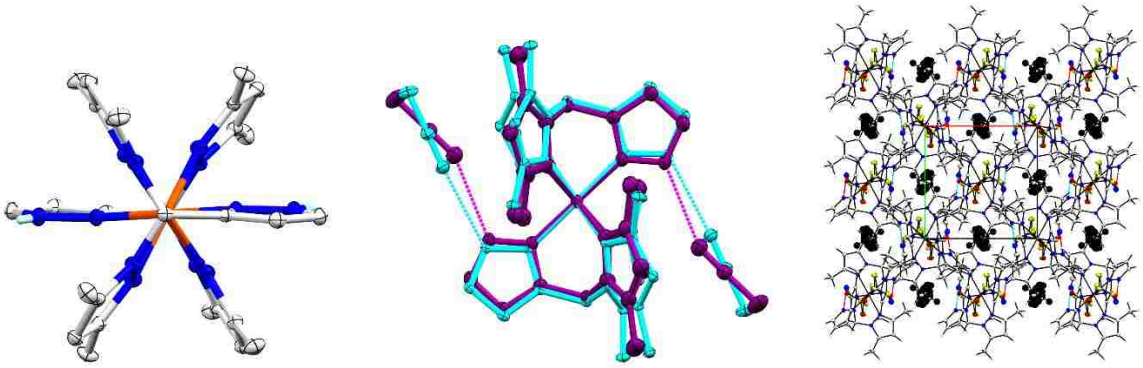

Figure 2.7. Left: View of the dication of *trans*-**1**·4CH_3CN down the $C_{methine}$-Fe vector with most H atoms, all CH_3CN and triflate atoms removed for clarity to emphasize pyrazolyl ring twisting; Center: Comparison of dications in *trans*-**1**·4CH_3CN (cyan) versus in *trans*-**1**·2CH_3CN (violet); Right: View of crystal packing of *trans*-**1**·4CH_3CN showing the half of the acetonitrile molecules (as larger black ball and sticks) in channels/pockets along the c- axis.

not very distorted in the disolvate. That is, the tetrasolvate has both greater pyrazolyl ring twisting (10.3° vs 1.4°) and pyrazolyl ring tilting (168.7° vs 177.8°) than the disolvate. In fact, the large pz twist in the tetrasolvate is close to the previously identified empirical 11° pz twist limit[72] whereby spin crossover has never been observed for an iron(II) scorpionate. This empirical limit presumably reflects that any large distortion(s) caused by crystal packing imparts an insurmountable kinetic barrier (especially at low temperature) for reorganization to a hypothetical undistorted low spin form. In *trans*-

1·4CH_3CN, two of the acetonitriles are hydrogen bonded to the dication (N1···N3 2.8796(18) Å, N1-H1n···N3, 168°) with a geometry quite similar to that in *trans*-**1**·2CH_3CN, vide supra (center of Figure 2.7). However, the other two acetonitrile molecules of solvation in **1**·4CH_3CN are loosely held in pockets along the *c*- axis (Figure 2.7, right) by CH···O[94] weak hydrogen-bonding interactions with the triflate anions (C9H9a···O1, 2.51 Å, 166°). These latter acetonitrile molecules are, in turn, pressed against the most distorted pz* ring (with N21) to give a short CH···π interaction[95] between the acetonitrile methyl donor and pyrazolyl acceptor (CH9b···Ct(N21) 2.73 Å, 132°). The three dimensional supramolecular structure of *trans*-**1**·4CH_3CN is constructed via weak N-H···N hydrogen bonding and various charge-assisted C-H···O interactions listed in Table 2.5. Figures 2.8a and 2.8b show the labelling of the various interactions involved in the 3D assembly. Two of the four acetonitrile solvates are hydrogen bonded to the confused pyrazolyl groups in the dication via N1-H1n···N3 (2.01 Å), and will be referred to as Type I solvate. A methyl hydrogen on the other two acetonitriles (Type II) are involved in long and presumably weak hydrogen bonding interaction with triflate oxygens of type O1 (C9-H9a···O1) to hold these solvate molecules (shown as black capped stick representations in Fig 2.8) loosely in the lattice. From a supramolecular assembly point of view, each triflate anion caps a ligand of the dications via three sets of C-H···O interactions. The acidic methine hydrogen H4 and the adjacent ring hydrogen of the confused pyrazolyl H2 interact with oxygen atoms on one triflate (C4-H4···O2 and C2-H2···O3), Figure 2.8b. A pyrazolyl methyl hydrogen H24c also interacts with O2 (C24-H24c···O2) to help anchor the triflate to the "back side" of the ligand. The third oxygen, O1, of the triflate acts as a weak hydrogen bond acceptor to Type I (and Type II,

as above) acetonitrile methyl hydrogens. Since each complex contains two triflates and two Type I CH_3CN's, the geometry is such as to generate a sheet parallel with the (-1 0 1) direction, Figure 2.8c and 2.8d. The sheets are stacked in the third dimension by a C-H···O interaction between a confused pyrazolyl ring hydrogen (H1, at the 2-position) and O3 of a triflate of an adjacent sheet, Figure 2.8e.

Table 2.5. Geometries of main N-H···N and C-H···O weak hydrogen-bonding interactions in *trans*-**1**·4CH_3CN.

Donor(D)(-H)	D-H (Å)	H···A (Å)	D···A (Å)	D-H···A (°)
N1-H1n···N3	0.88	2.01	2.88	168
C1-H1···O3	0.95	2.57	3.19	123
C2-H2···O3	0.95	2.47	3.42	175
C4-H4···O2	1.00	2.35	3.31	162
C7-H7b···O1	0.98	2.35	3.31	170
C9-H9a···O1	0.98	2.51	3.47	166
C24-H24c···O2	0.98	2.54	3.18	123

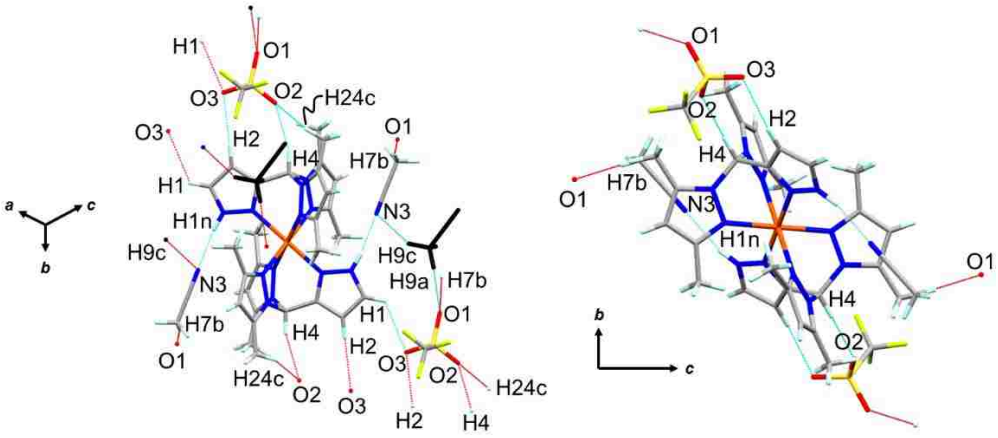

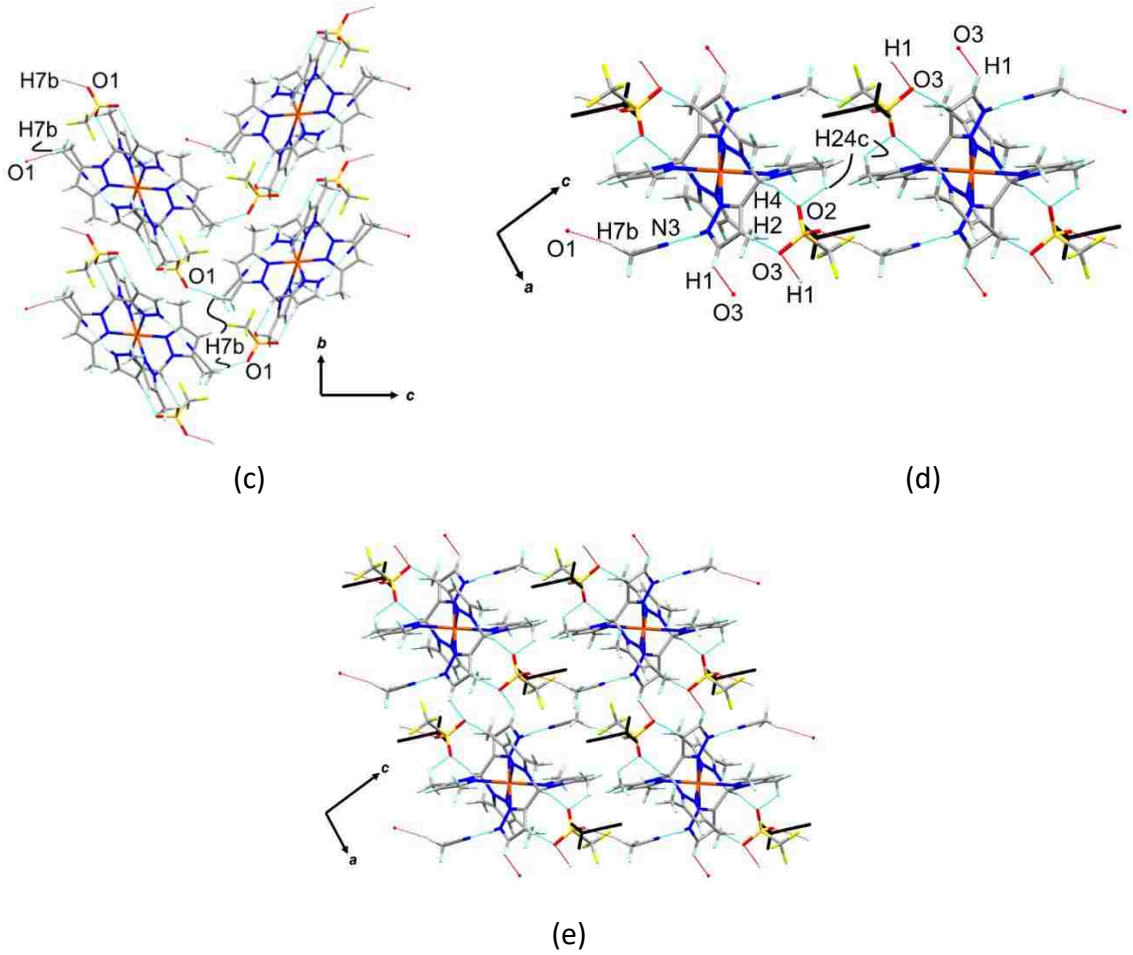

Figure 2.8. Supramolecular assembly of *trans*-**1**·4CH_3CN. (a) View and labelling of all short contacts (completed, cyan; dangling, red) involving *trans*-**1**·4CH_3CN where two solvate CH_3CN molecules are represented as black capped sticks. (b) an alternate and simplified diagram viewed down a-axis. (c) View of sheet down a. (d) View of sheet side down the b-axis. (e) View down b-axis of two stacked sheets.

Single crystal X-ray diffraction data was obtained for a colorless needle of *cis*-**1** at 250 K and then after cooling to 100 K when the needle was violet (Figure 2.9). A listing of selected bond distances and interatomic angles for *cis*-**1** at different temperatures are provided in Table 2.6. The

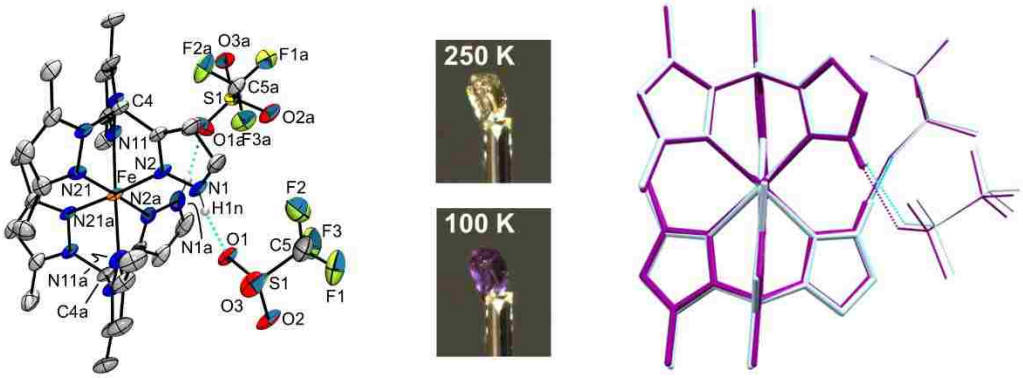

Figure 2.9. Left: Structure of *cis*-[Fe(^{H}L*)$_2$](OTf)$_2$, *cis*-***1***, at 100 K; Middle: Photographs of a crystal at different temperature; Right: Overlay of structures obtained at 250 K (light blue) and 100 K (violet).

compound crystallizes in the space group P2$_1$/c where the asymmetric unit is composed of one cation, one well-ordered triflate anion, and another triflate anion that is disordered unequally (2:1) over two nearby positions. The FeN$_6$ coordination environment is distorted octahedral since the Fe-N bonds of the confused pyrazolyl are at least 0.02 Å shorter than those of the (inequivalent) pz* groups. At 250 K, the average Fe-N bond distance of the six bonds is 2.17(2) Å which is aligned with expectations for HS iron(II). At 100 K, the average distance shortens to 2.11(2) Å, indicative of an increasing portion (ca. 33%) of LS iron(II). For reference, the compound [Fe(^{Bn}L)$_2$](BF$_4$)$_2$·2CH$_3$CN (with an N-benzyl on the 'confused' pyrazolyl and unsubstituted 'normal' pyrazolyls) had an average Fe-N bond distance of 2.14 Å at 250 K (partly LS) and 1.99 Å at 100 K (fully LS).[73] In *cis*-**1**, the average pyrazolyl ring twist is 6° at both temperatures; thus, spin crossover behavior is expected and is observed in this case, vide infra.

Table 2.6. Bond distances (Å), angles (deg.) and torsion angles (deg.) for *cis*-**1.**

	250 K	100 K
Bond Distances (Å) Fe1-N2	2.146(2)	2.0849(17)

Fe1-N11	2.173(2)	2.1089(14)
Fe1-N21	2.192(2)	2.1356(15)
Fe1-N2a	2.146(2)	2.0833(16)
Fe1-N11a	2.196(2)	2.1404(16)
Fe1-N21a	2.177(2)	2.1242(17)
Bond Angles (°)		
N2-Fe1-N11	82.57(9)	83.46(6)
N2-Fe1-N21	83.77(9)	84.47(6)
N11-Fe1-N21	85.25(9)	86.14(5)
N2a-Fe1-N11a	82.36(9)	83.52(6)
N2a-Fe1-N21a	83.75(9)	84.29(6)
N11a-Fe1-N21a	85.52(9)	86.59(6)
Bond Torsions (°)		
C4C3-N2Fe1	-9.3(3)	-8.3(2)
C4N12-N11Fe1	2.3(3)	1.7(2)
C4N22-N21Fe1	-9.7(3)	-9.1(2)
C4aC3a-N2aFe1	-2.7(3)	-3.9(2)
C4aN12a-N11aFe1	5.5(3)	3.2(2)
C4aN22a-N21aFe1	-8.3(3)	-10.8(2)

The three dimensional supramolecular structure of *cis*-**1** is constructed from N-H···O,[93] C-H···O,[94] and C-H···F[96] weak charge-assisted hydrogen bonding interactions involving hydrogen donors of the dications and either oxygen or fluorine acceptors of the triflate anions (Table 2.7 and Figure 2.10). One of the triflate anions is disordered in a 2:1 ratio over two positions, thus the discussion will first focus on the well-ordered triflate anion with atoms O1, O2, and O3. A sheet of cations is formed in the *ac*- plane by N-H···O and C-H···O weak hydrogen-bonding interactions involving these well-ordered triflate anions (contact #'s 1, and 4-8 in Table 2.7). That is, a dimer is formed by a pair of triflate anions bridging two dications where O1 of the triflate interacts with the N-H of the confused pyrazolyl (N1-H1n···O1, 1.98 Å) on one cation and O2 interacts with the methine hydrogen, H4a, of the neighboring dication. This hydrogen bonding interaction is in the range found for other hydrogen-bonded iron(II) SCO compounds. For

Table 2.7. Geometries of main N-H···O and C-H···O weak hydrogen-bonding interactions in *cis*- **1** at 100 K.

Contact	Donor(D)(-H)	D-H (Å)	H···A (Å)	D···A (Å)	D-H···A (°)
1	N1-H1n···O1	0.83(3)	1.98(3)	2.795(2)	170(3)
2	N1a-H1na···O1a	0.83(3)	1.96(3)	2.678(3)	143(2)
3	N1a-H1na···O1b	0.83(3)	2.29(3)	3.103(5)	165(3)
4	C2a-H2a···O2	0.95	2.55	3.243(3)	130
5	C4a-H4a···O2	1.00	2.26	3.188(2)	154
6	C24a-H24a···O2	0.98	2.48	3.401(3)	156
7	C12-H12···O2	0.95	2.56	3.445(2)	156
8	C22-H22···O3	0.95	2.48	3.190(2)	132
9	C4-H4···O2a	1.00	2.23	3.157(14)	154
10	C4-H4···O2b	1.00	2.42	3.34(3)	153
11	C2-H2···O2a	0.95	2.54	3.22(2)	128
12	C2-H2···O2b	0.95	2.57	3.29(3)	133
13	C20a-H20b···O3a	0.98	2.44	3.420(5)	176

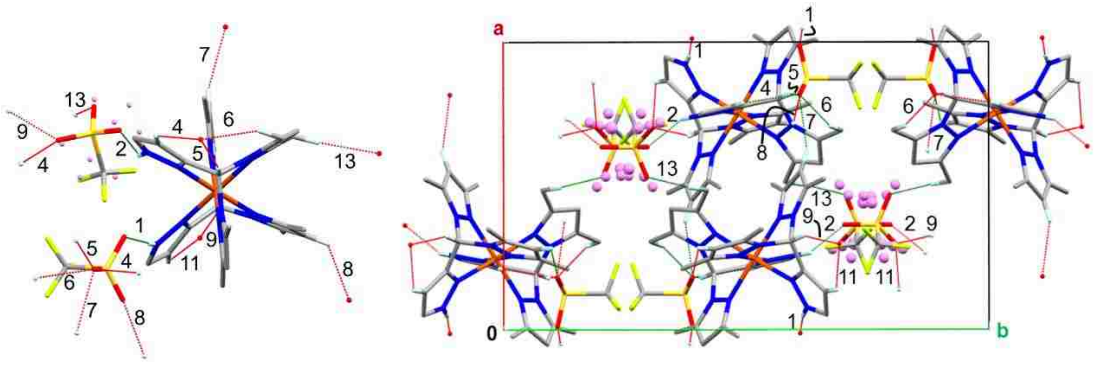

(a) (b)

Figure 2.10. Noncovalent interactions of *cis*-**1**. (a) Labeling of atoms involved in interactions. Hanging and completed contacts are red and green dashed lines, respectively. Pink spheres represent minor triflate disorder component. (b) View down c-axis of unit cell with noncovalent interactions labeled in accord with Table 2.7.

instance, N-H···O interactions in [Fe(2,6-bis(pyrazol-3-yl)pyridine)$_2$](cis,cis-1,3,5-cyclohexanetricarboxylate dianion)·5.5 H_2O range from 1.73 to 1.86 Å [97], those in [Fe(2,6-bis[5-methyl-1H-pyrazol-3-yl]pyridine)$_2$](ClO_4)$_2$-solvate (solvate = H_2O, MeOH, or $MeNO_2$) that range from 1.80 to 2.26 Å[98] or those in [Fe(2-(pyrazol-1-yl)-6-(pyrazol-

3-yl)pyridine)$_2$]$(ClO_4)_2$ of 1.93 and 2.03 Å.[99] The dimers are organized into sheets parallel with the *ac*-plane (containing the two dications in the middle of the unit cell in Figure 2.10b) by interactions of O2 and O3 of one dimer with the hydrogens at the 4-positions of the dimethylpyrazolyl groups of neighboring dimers (interactions 7 and 8, Table 2.7). The *ac*-sheets are stacked along the *b*-axis by hydrogen bonding interactions with oxygen atoms of the disordered triflate (major disorder component: contact #'s 2, 9, 11, and 13 minor disorder component: contact #'s 3, 10, and 12 in Table 2.7). Importantly, each contact with the disordered triflate falls well below the limits for NH···O or CH···O interactions and are in the range of medium-strength hydrogen bonds.[87a,b] Similarly, the acidic methine hydrogen, H4, of one *ac*-sheet acts as a donor to triflate oxygens from an adjacent sheet (67% involve contact 9 and 33% involve contact 10, Table 2.7) where both associated C···O distances are well within the accepted limits for a CH···O interaction.[88] The minor component of the disordered triflate also has a number of CH···F weak hydrogen bonding interactions that serve to support the structure but will not be discussed further. The overall supramolecular structure is retained at 250 K but all contacts are elongated versus those at 100 K.

The structure of *trans*-**1** was determined at 250 K and 100 K, where the crystal was light pink and violet, respectively. The crystal undergoes a reversible phase transition over this temperature range, being monoclinic ($P2_1/c$) at 250 K but is triclinic (P-1) at 100 K. In the 250 K structure, the asymmetric unit (Figure 2.11a) contains one well-ordered (containing S1) and one disordered triflate (containing S1a) anion in general positions and two independent Fe(^{H}L*) units where the iron center in each is located on

an inversion center thereby guaranteeing each is the *trans*- isomer. The average Fe-N bond distance about Fe1a (Table 2.8) of 2.18(3) Å is typical of

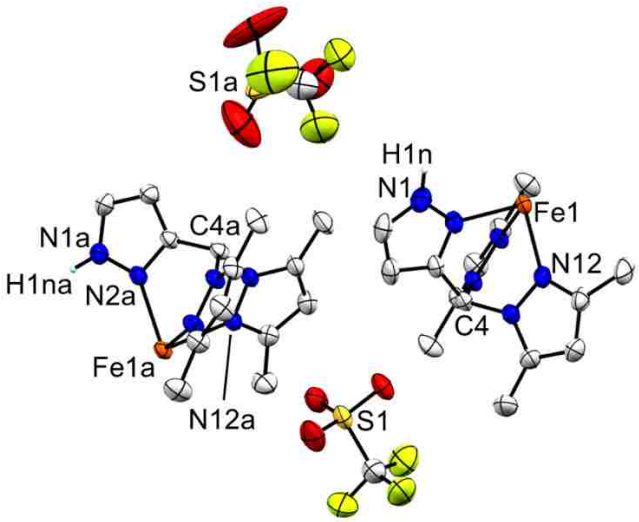

(a)

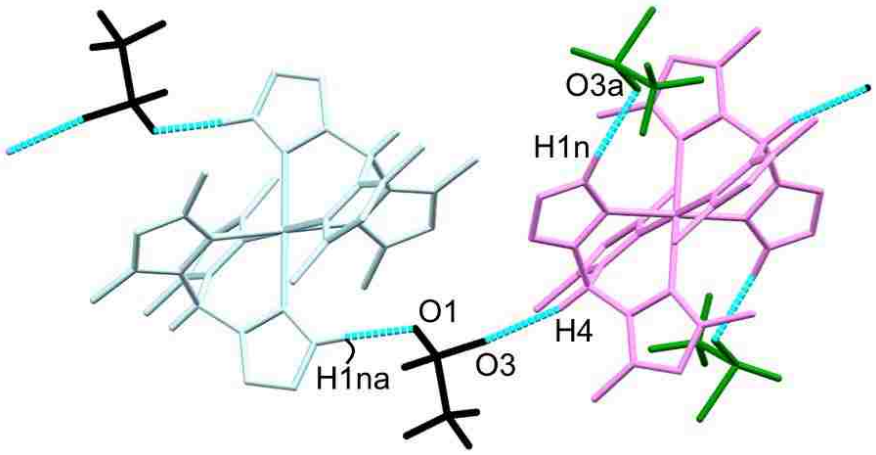

(b)

Figure 2.11. (a) Asymmetric unit of the 250 K structure of trans-[Fe(^{H}L*)$_2$](OTf)$_2$, *trans*-**1**, with partial atom labeling. and (b) View showing shortest three hydrogen bonding interactions (Σ van der Waals radii – 0.4 Å, cyan dotted lines) forming chains. Color key: Black sticks = well-ordered triflate ion, Green sticks = disordered triflate ion, Pale Blue sticks = HS dication with central Fe1a, Pink sticks = partial HS/LS dication with central Fe1.

Table 2.8. Bond distances (Å), angles (deg.) and torsion angles (deg.) for *trans*-**1.**

	250 K	100 K			
Bond Distances (Å)		Bond			
Fe1-N2	2.082(4)	Fe1-N2	1.942(3)	Fe1b-N2b	2.143(2)
Fe1-N12	2.129(4)	Fe1-N12	2.010(2)	Fe1b-N12b	2.172(3)
Fe1-N22	2.151(4)	Fe1-N22	1.990(2)	Fe1b-N22b	2.216(3)
Fe1a-N2a	2.145(4)	Fe1a-N2a	2.063(3)	Fe1c-N2c	2.146(3)
Fe1a-N12a	2.216(4)	Fe1a-N12a	2.125(3)	Fe1c-N12c	2.214(3)
Fe1a-N22a	2.173(3)	Fe1a-N22a	2.139(3)	Fe1c-N22c	2.179(3)
Bond Angles (°)		Bond Angles			
N2-Fe1-N12	84.52(16)	N2-Fe1-N12	87.77(10)	N2b-Fe1b-	83.42(10)
N2-Fe1-N22	84.66(15)	N2-Fe1-N22	87.68(11)	N2b-Fe1b-	83.49(10)
N12-Fe1-N22	85.17(14)	N12-Fe1-N22	87.28(10)	N12b-Fe1b-	82.84(10)
N2a-Fe1-N12a	83.82(15)	N2a-Fe1a-	84.98(11)	N2c-Fe1C-	83.49(10)
N2a-Fe1-N22a	83.60(14)	N2a-Fe1a-	84.57(10)	N2c-Fe1C-	83.37(10)
N12a-Fe1-N22a	82.79(15)	N12a-Fe1a-	85.62(10)	N12c-Fe1C-	82.04(11)
Bond Torsions (°)		Bond			
C4C3-N2Fe1	-3.3(6)	C4C3-N2Fe1	0.8(4)	C4bC3b-	7.3(4)
C4N11-N12Fe1	-7.7(5)	C4N11-	0.5(3)	C4bN11b-	3.9(4)
C4N21-N22Fe1	-0.8(5)	C4N21-	3.9(3)	C4bN21b-	8.4(4)
C4aC3a-N2aFe1a	-6.7(5)	C4aC3a-	-8.6(4)	C4cC3c-	-5.8(4)
C4aN11a-N12aFe1a	-6.0(5)	C4aN11a-	-12.5(3)	C4cN11c-	-5.5(4)
C4aN21a-N22aFe1a	-3.0(5)	C4aN21a-	-4.5(3)	C4cN21c-	-3.0(4)

HS iron(II) whereas that about Fe1 of 2.12(3) Å is indicative of partial LS character (HS/LS). The confused pyrazolyl N-H groups in each serve as hydrogen bond donors to oxygen atoms of triflate anions (Figure 2.11b). The HS complex has N-H···O interactions with the well-ordered triflate (N1aH1na···O1 , 1.94 Å, 169°) while the HS/LS complex interacts with the disordered triflate (N1H1n···O3a, 2.17 Å, 167°). The well-ordered also triflate interacts with the acidic methine hydrogen of the partially LS complex (C4H4···O3, 2.30 Å, 157°) to form a chain of complexes with alternating (HS/LS) Fe1 and HS Fe1a centers along the [1 0 1] direction. The three dimensional supramolecular structure of *trans*-**1** at 250 K is constructed via various N-H···O hydrogen bonding and charge-assisted weak C-H···O interactions listed in Table 2.9. Figure 2.12a shows the labelling of the various interactions involved in the 3D assembly.

The N-H···O (contact 1, Table 2.9) and C-H···O interactions (contacts 3,5, and 6, Table 2.9) involving the oxygen atoms of the well-behaved triflate serve to assemble the dications into sheets parallel with the *ac*- plane (Figures 2.12b and 2.12c). The *ac*-sheets are stacked along the *b*- direction by N-H···O (contact 2, Table 2.9) and C-H···O interactions (contact 4, Table 2.9) between the hydrogens of confused pyrazolyl rings and the oxygen atoms of the disordered triflate (Figures 2.12c and 2.12d). This results such that all disordered triflates are found in layers of dictions that are partly LS (the SCO layer).

Table 2.9. Geometries of main N-H···O and C-H···O weak hydrogen-bonding interactions (sum of van der Waals radii – 0.2 Å) in *trans*-**1** (250 K).

Contact #	Donor(D)(-H)	D-H (Å)	H···A (Å)	D···A (Å)	D-H···A (°)
1	N1a-H1na···O1	0.87	1.94	2.802(6)	169
2	N1-H1n···O3a	0.87	2.17	3.024(13)	167
3	C1-H1···O2	0.94	2.55	3.108(8)	118
4	C2a-H2a···O2a	0.94	2.48	3.264(13)	141
5	C4-H4···O3	0.99	2.30	3.236(6)	157
6	C10-H10a···O3	0.97	2.46	3.399(9)	163

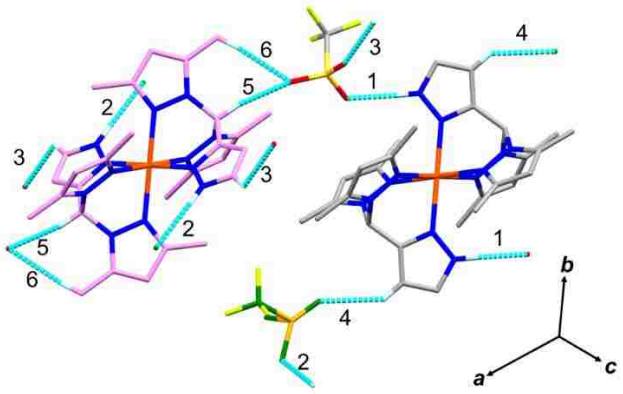

(a)

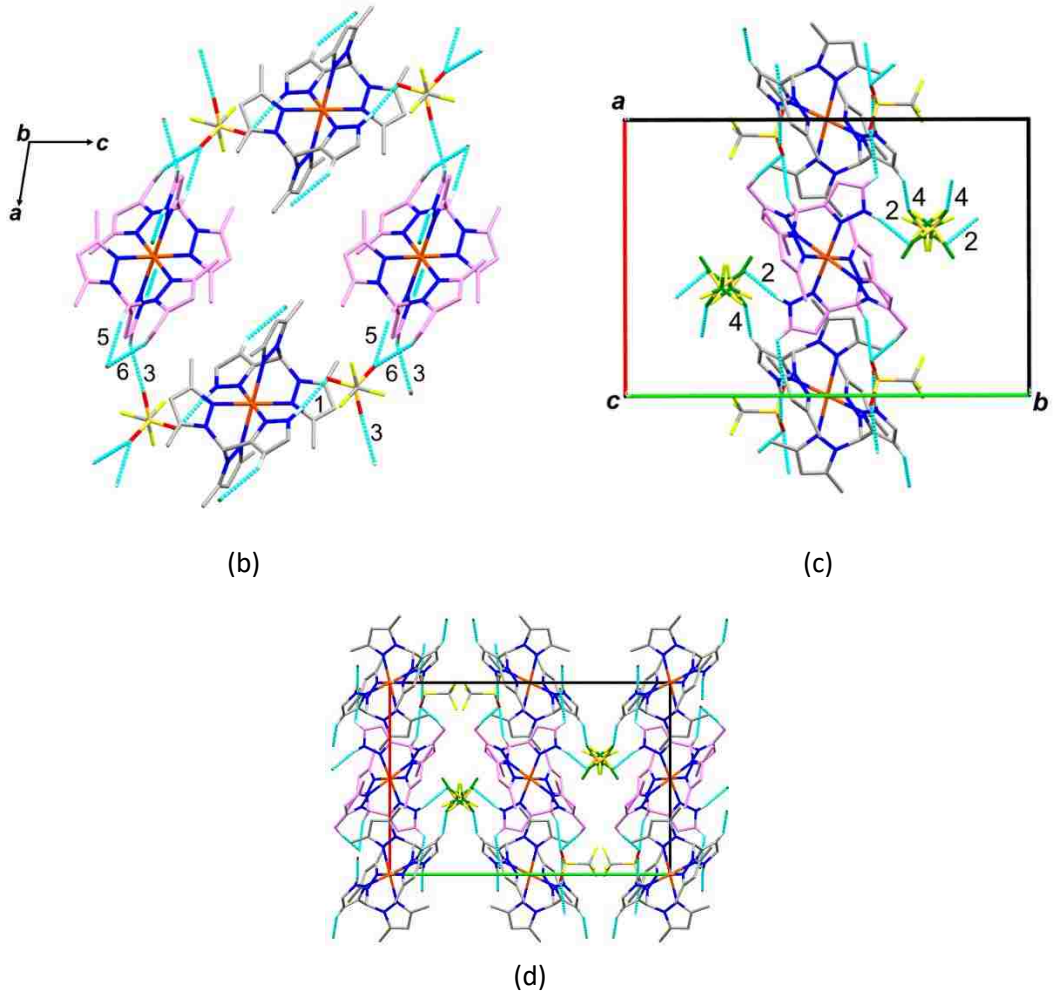

Figure 2.12. Supramolecular assembly of *trans*-**1** at 250 K. (a) View of short contacts (cyan) listed in Table 2.9. The dication that is partially LS has pink carbons while the disordered triflate has a green carbon and green oxygen atoms. (b) View down the b-axis of ac- sheet. (c) View down c- of the ac-sheet (d) View of the unit cell down c.

In the 100 K structure, the asymmetric unit (Figure 2.13a) contains three well-ordered triflate ions

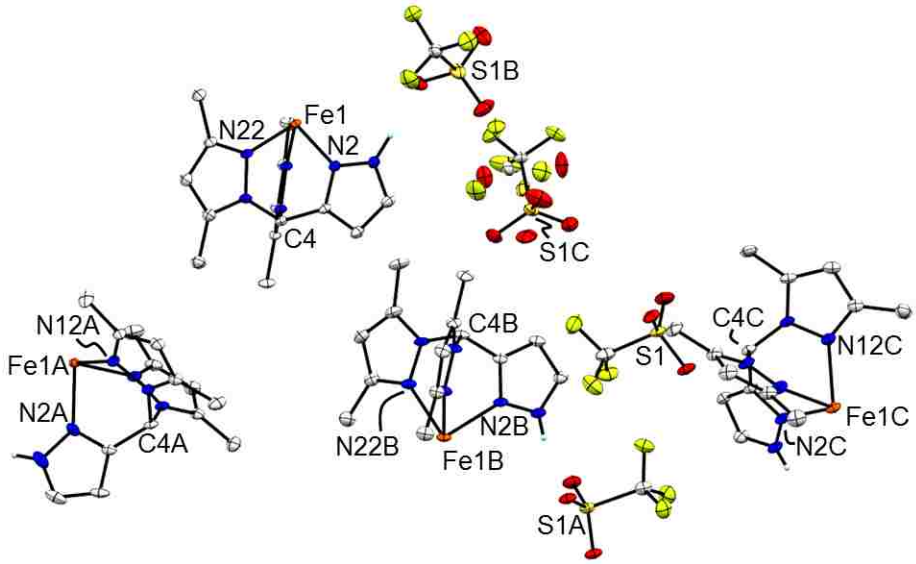

(a)

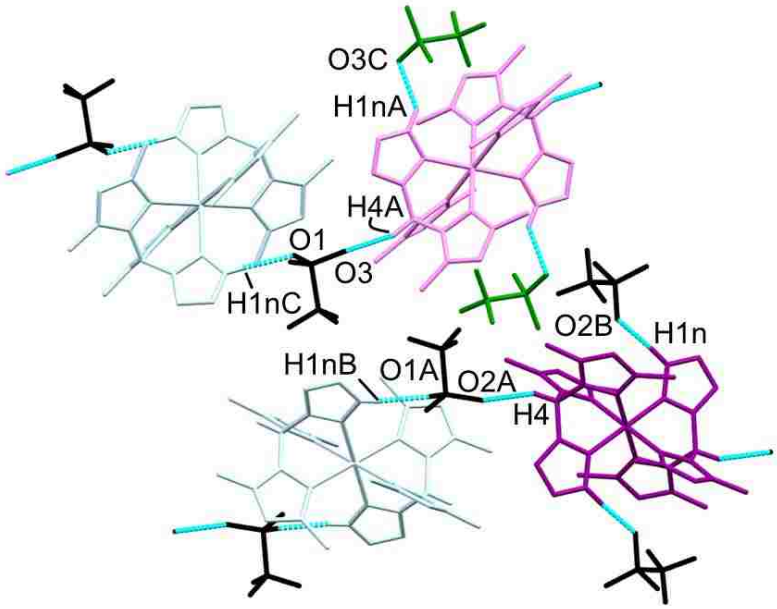

(b)

Figure 2.13. (a) Asymmetric unit of the 100 K structure of *trans*-[Fe(^{H}L*)$_2$](OTf)$_2$, *trans*-**1**, with partial atom labeling. and (b) View showing some of the shortest hydrogen bonding interactions (van der Waals radii – 0.45 Å, cyan dotted lines) forming two chains. Color key: Black sticks = well-ordered triflate ion, Green sticks = disordered triflate ion, Pale Blue sticks = HS dication with central Fe1b or Fe1c, Pink sticks = partial HS/LS dication with central Fe1a, dark violet sticks LS dication with central Fe1.

(containing S1, S1a, and S1b) and one disordered triflate (over two nearby positions in a 2:1 S1c:S1d ratio) on general positions and four independent Fe(^{H}L*) units whose metal centers are on inversion centers generating *trans*- isomers by symmetry. Inspection of the Fe-N distances reveals that two of the dications with Fe1b and Fe1c are HS (avg. Fe-N = 2.18(4) and 2.18(3) Å, respectively) and that the dication with a central Fe1 is LS (avg. Fe-N = 1.98(3) Å). The last dication with Fe1a has an average Fe-N distance of 2.11(4) Å that corresponds to approximately 25-33% LS character, so is labelled HS/LS. As with the 250 K structure, the triflate ions are hydrogen-bonded to the dications via N-H···O interactions (cyan dashed lines Figure 2.13b). Three interactions involve well-ordered triflate ions (N1H1n···O2b, 1.81(5) Å, 176(4)^{o}; N1bH1nb···O2b, 2.03(4) Å, 168(4)^{o}; N1cH1nc···O1, 2.07(4) Å, 176(4)^{o}) while the remaining interaction involves the partly LS complex and the disordered triflate (major component: N1aH1na···O3c, 2.07(4) Å, 134(4)^{o} and minor component: N1aH1na···O1d 2.12(4) Å, 170(4)^{o}). Two of the well-ordered triflate ions also interact with methine hydrogen on neighboring dications (C4H4···O2a 2.26 Å, 154^{o} and C4aH4a···O3 2.21 Å, 154^{o}) to form two separate chains. One chain along the [2 2 0] direction has alternating dications of HS Fe1c and (LS/HS) Fe1a while the other chain along the [1 1 0] direction has alternating dications of HS Fe1b and (LS) Fe1. As described above and shown in Figure 2.14a, there are four independent dications in the asymmetric unit where the iron atom resides on an inversion center. The iron-nitrogen distances reveal there are two high spin complexes (HS1 and HS2), a low spin (LS) complex, and one intermediates spin dication (HS/LS). There are also three well behave triflate ions and one triflate that is disordered over two nearby positions (green atoms Figure 2.14a). This disordered triflate is hydrogen bonded

to the (HS/LS) complex. The N-H···O hydrogen bonding and charge-assisted weak C-H···O interactions listed in Table 2.10 give rise to a three dimensional supramolecular structure. The structure can be described by only considering those interactions involving well behaved triflate while those of the disordered triflate (contact #'s 2, 10, 13, Table 2.10) serve to support the overall structure. One triflate bridges neighboring HS1 and LS dications to form a chain along [1 1 0] via N-H···O interaction with HS1 and a C-H···O interaction with LS methine hydrogens (contacts 3 and 8, Table 2.10). Similarly, the N-H···O interaction with HS2 and a C-H···O interactions with (HS/LS) (contacts 4, 6, 9 and 11, Table 2.10) gives a chain along [2 2 0]. As seen in Figure 2.14b and 2.14c, these chains are assembled into sheets in the (2 2 -2) plane by another bridging triflate that connects LS complex via a N-H···O interaction and a C-H···O interaction of a confused pyrazolyl hydrogen on HS2 (contacts 1 and 7, Table 2.10). The sheets are stacked in the third dimension by C-H···O interactions with bridging triflate oxygens and either the unique ring hydrogen of a pz* group on HS1 or the 3-position hydrogen of the confused pyrazolyl of HS/LS (contacts 5, 12, and 14, Table 2.10.

Table 2.10. Geometries of main N-H···O and C-H···O weak hydrogen-bonding interactions (sum of van der Waals radii – 0.2 Å) in *trans*- **1** at 100 K.

Contact	Donor(D)(-H)	D-H (Å)	H···A (Å)	D···A (Å)	D-H···A (°)
1	N1-H1n···O2b	0.97(5)	1.81(5)	2.778(4)	176(4)
2	N1a-H1na···O3c	0.89(4)	2.07(4)	2.765(5)	134(4)
3	N1b-	0.76(4)	2.03(4)	2.781(4)	168(4)
4	N1c-H1nc···O1	0.71(4)	2.07(4)	2.777(4)	176(5)
5	C1a-H1a···O2	0.95	2.47	3.049(5)	119
6	C2a-H2a···O3	0.95	2.57	3.246(5)	128
7	C2c-H2c···O3b	0.95	2.50	3.298(6)	141
8	C4-H4···O2a	1.00	2.26	3.190(4)	154
9	C4a-H4a···O3	1.00	2.21	3.142(4)	154
10	C4b-H4b···O2c	1.00	2.31	3.267(5)	160
11	C10a-H10g···O3	0.98	2.51	3.365(5)	145
12	C12b-	0.95	2.54	3.463(5)	165
13	C20b-	0.98	2.24	3.051(6)	139

14	C22c-H22c···O3	0.95	2.48	3.422(5)	170

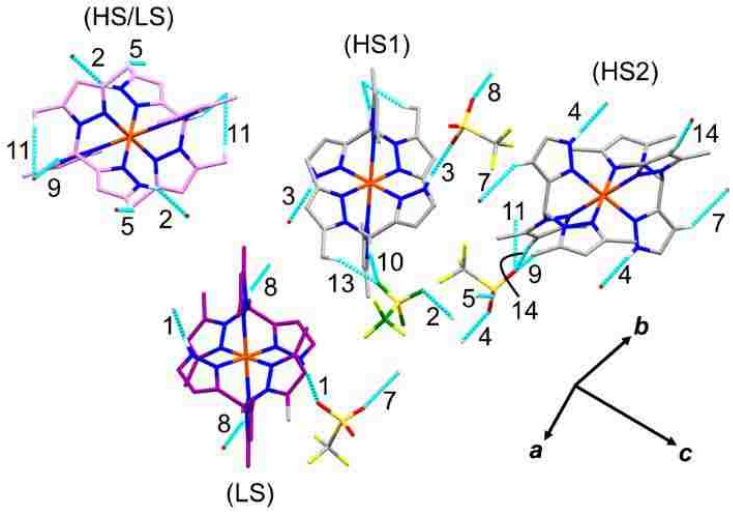

(a)

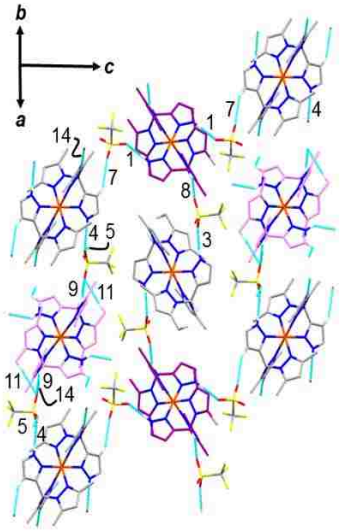

(b)

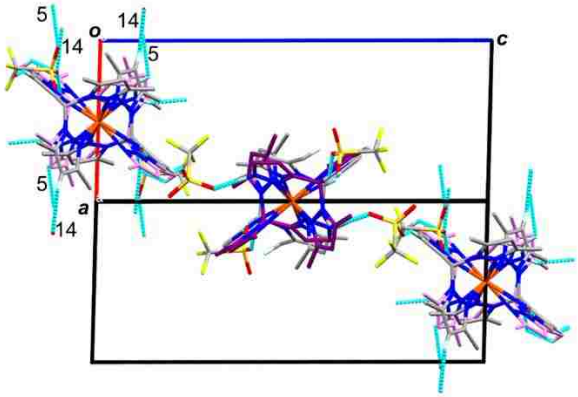

(c)

Figure 2.14. Supramolecular assembly of *trans*-**1** at 100K. (a) View of selected short contacts (numbered cyan lines) listed in Table 2.10; contacts 6 and 12 are omitted for clarity. The dication that is partially LS has pink carbons, the dication that is fully LS is has dark violet carbons, those HS dications have grey carbons. The disordered triflate has a green carbon and green oxygen atoms. (b) Top view of a sheet (2 2 -2) formed by interactions involving only well-behaved triflate ions. (c) Side view of sheet.

Figure 2.15 provides comparative views of the crystal packing diagrams in the 250 K (left) and 100 K (right) structures. The crystal packing is quite similar at both temperatures; with layers of HS complexes stacked alternately with layers of complexes with partially (LS/HS) or, fully LS (100 K case) complexes along the *a*- direction (250 K) or *c*- direction (100 K), or colloquially, the SCO layer. The well-ordered triflates (black sticks, Figure 2.15) are found in the HS layers at each temperature. The main differences in the structures occur in the SCO layers. At 250 K, the SCO layers contain partly HS/LS complexes (25-33% LS character from bond distances) and disordered triflate ions. At 100 K, one half of the complexes in the SCO layer (25% overall) have converted to fully LS (dark violet sticks, right of Figure 2.15). The other half of complexes in this layer remain (HS/LS) (25-33% LS character). So, based on estimation from bond-distances, the entire sample is approximately 31-33% LS at 100 K. Coincidentally, at 100 K one half of the triflate ions in the SCO layer (75 % overall) are now fully ordered (red arrows bottom of Figure 2.15); decreasing the temperature from 250 K to 100 K and the associated SCO contracts the unit cell sufficiently to lock one of the triflate ions into one position. The remaining 25% of the triflate ions are disordered. If the minor disorder component (34% occupancy) is associated with LS component of the partial SCO, then 33.5 % (25% LS + 34% occupancy*25% HS/LS) of the total complexes in the unit cell would be LS *trans*-**1** at 100 K.

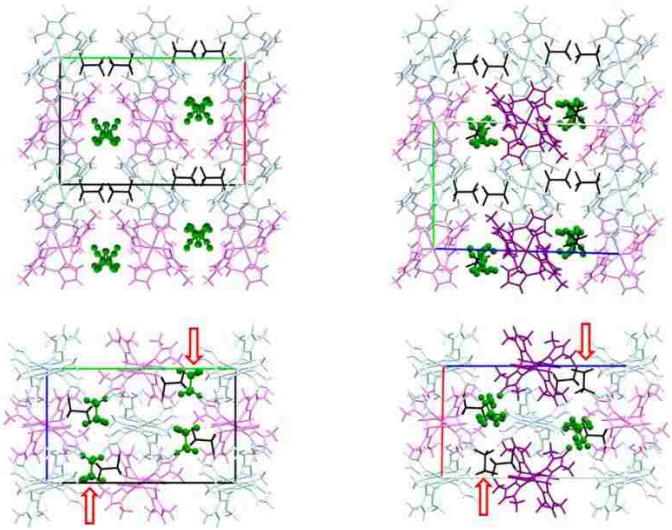

Figure 2.15. Comparison of a portion of the crystal packing diagrams in the 250 K (left) and 100 K (right) structures of trans-**1**. Top left: View to down c-axis. Top right: View down a- axis. Bottom left: View down a- axis. Bottom right: View down b-axis. Axes color scheme: a- axis (red), +b-axis (green), and +c axis (blue). Red arrows highlight transition in disorder/well-ordered triflate types upon changing temperature.

Crystals of *co*-**1** turn violet on cooling to 77 K, so single crystal X-ray diffraction experiments were performed at two temperatures, 250 K (colorless/pale blue) and 100 K (violet). Views of the 100 K structure are found in Figure 2.16 while bond distances and interatomic angles are listed in Table 2.11. The asymmetric unit (Figure 2.16a) consists of one well-ordered triflate (with terminal atoms bound to the S1-C5 unit), one triflate that is disordered unequally over two nearby positions (84% containing S1a-C5a and 16% containing S1b-C5b) and two Fe(^{H}L*) moieties (one with Fe1 on an inversion center and one with Fe2 on a two-fold rotation axis). By crystallographic symmetry, the dication with Fe1 is the *trans*- isomer (angle between iron-bound 'confused' nitrogens, N2-Fe1-N2' = 180.0(1)^{o}) whereas that with Fe2 is the

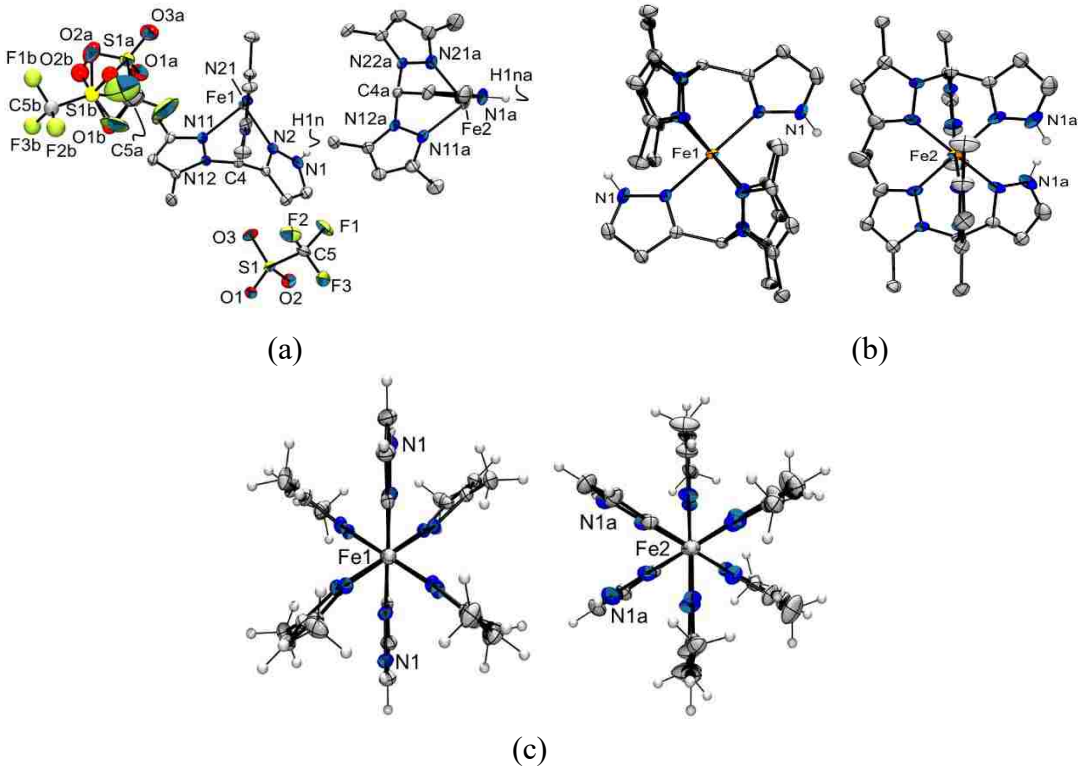

Figure 2.16. Views of the structure of a crystal with a 1:1 ratio of *cis*-$\mathbf{1}^{2+}$:*trans*-$\mathbf{1}^{2+}$, a crystal form called *co*-**1.** (a) asymmetric unit with partial atom labelling and most hydrogen atoms removed for clarity. (b) View of the *trans*- (left) and *cis*- (right) dication components. (c) View of the dications down the C(methine)-H bond showing greater pz ring tilting in the *trans*- isomer (left) than the *cis*- isomer (right).

Table 2.11. Bond distances (Å), angles (deg.) and torsion angles (deg.) for co-**1.**

Bond Distances (Å)	250 K	100 K
Fe1-N2	2.1321(19)	2.103(3)
Fe1-N11	2.2059(18)	2.163(3)
Fe1-N21	2.1850(18)	2.154(3)
Fe2-N2a	2.132(2)	2.032(4)
Fe2-N11a	2.178(2)	2.087(3)
Fe2-N21a	2.156(2)	2.064(3)
Bond Angles (°)		
N2-Fe1-N11	85.32(7)	85.68(11)
N2-Fe1-N21	84.10(7)	84.82(11)
N11-Fe1-N21	82.38(7)	83.07(10)
N2a-Fe2-N11a	85.83(8)	86.83(13)
N2a-Fe2-N21a	82.26(8)	84.35(13)
N11a-Fe2-N21a	85.94(8)	87.11(13)
Bond Torsions (°)		
C4C3-N2Fe1	-6.1(3)	-6.1(4)
C4N12-N11Fe1	-4.9(2)	-5.0(4)
C4N22-N21Fe1	-2.2(2)	-3.2(4)

C4aC3a-N2aFe2	-6.9(3)	-5.4(4)
C4aN12a-N11aFe2	-4.5(3)	-3.8(4)
C4aN22a-N21aFe2	5.9(3)	4.4(4)

cis-isomer (N2-Fe2-N2' = 92.5(2)º), Figure 2.16b. At 250 K, the average Fe-N bond distances indicate that both the *trans*- (2.17 Å) and *cis*- (2.16 Å) components are HS Fe(II). At 100 K, the *trans*- isomer remains HS ($Fe\text{-}N_{avg}$ 2.14 Å) while the *cis*-isomer has $Fe\text{-}N_{avg}$ of 2.06(3) Å, a distance between HS (2.18 Å) and LS (ca. 1.98 Å) roughly corresponding to about 38 ± 12% HS character (overall 69% HS or 31 ± 6% SCO). It is noteworthy that the *trans*- component not only has longer bond distances than the *cis*-component but the ligand is more distorted with greater pyrazolyl ring twisting (5.8 vs 4.4º at 250 K or 4.8 vs 4.5º at 100 K) and ring tilting (171º vs 175º at 250 K or 172º vs 176º at 100 K), Figure 2.16c. In other words, the *cis*- isomer with a less distorted ligand and shorter bonds at room temperature undergoes SCO on cooling (albeit incomplete over this temperature range).

An examination of the three-dimensional supramolecular structure provides insight into why the *cis*- component of *co*-**1** undergoes SCO but the *trans*- does not. Views of the crystal packing arrangement are found in Figure 2.17, while Table 2.12 lists the short non-covalent interactions that

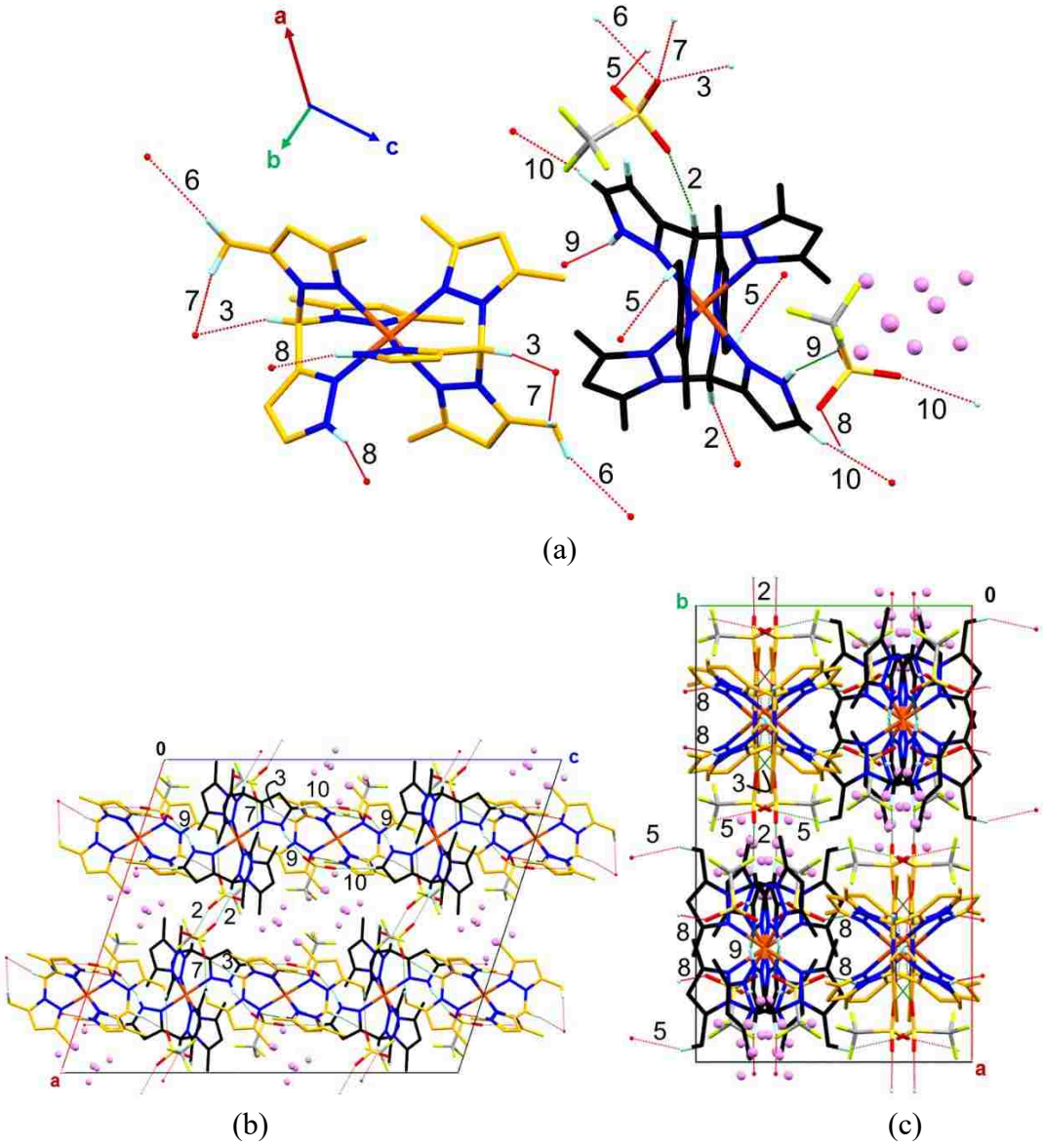

Figure 2.17. Supramolecular structure of *co*-**1**. (a) View of important noncovalent interactions with atom labeling. The *cis*- isomer has light orange carbons as capped sticks while the trans- isomer shows carbon as black capped sticks. Hanging and completed contacts are red and green dashed lines, respectively. Pink spheres represent minor triflate disorder component. (b) View of unit cell down b with contact # from Table 2.12 labeled. (c) View of unit cell down c with contacts labeled as per Table 2.12.

help organize the structure. The three dimensional structures of *co*-**1** at 250 K and 100 K are only slightly different, so the 100 K structure is discussed first. As stated above, there are two triflate anions, one well-ordered and one disordered. The three dimensional

structure can be described by only considering charge-assisted C-H···O weak hydrogen bonding interactions[94] with the well-ordered triflate where interactions with the disordered triflate further support the structure. The C-H···O interactions assemble each of the *cis*- (colored orange in Fig. 2.17) or *trans*-(colored black in Fig 2.17) isomers into separate polymeric chains (that contain only one type of isomer) that run parallel with the *c*- axis (Figures 2.17b and 2.17c). The *cis*- chain is organized via trifurcated C-H···O interaction involving O1 as a bridging acceptor to a 5-methyl hydrogen donor (H24e) on one complex and both a methine (H4a) and a nearby 5-methyl hydrogen (H24f) donor on a neighboring complex, (contacts 3, 6, and 7, Table 2.12). The

Table 2.12. Geometries of selected weak hydrogen-bonding interactions in *co*-**1** at 100 K.

contact	Donor(D)(-H)	D-H (Å)	H···A (Å)	D···A (Å)	D-H···A (°)
	ordered triflate				
1	C2-H2···O3	0.95	2.60	3.286(5)	130
2	C4-H4···O3	1.00	2.24	3.182(5)	157
3	C4a-H4a···O1	1.00	2.26	3.211(4)	158
4	C14-H14a···O3	0.98	2.57	3.434(5)	147
5	C24-H24b···O2	0.98	2.46	3.366(5)	154
6	C24-H24e···O1	0.98	2.55	3.477(5)	158
7	C24-H24f···O1	0.98	2.42	3.279(5)	145
	disordered triflate				
8	N1a-H1na···O3a	0.88	1.96	2.807(5)	162
9	N1-H1n···O1a	0.88	1.93	2.744(5)	154
10	C1-H1···O2a	0.95	2.45	3.395(6)	173
11	C1-H1···O2b	0.95	2.53	3.40(2)	153
12	C1a-H1a···O3b	0.95	2.54	3.20(2)	120
13	C10a-H10e···O2b	0.98	2.59	3.34(2)	133
14	C22a-H22e···F1b	0.98	2.48	3.269(18)	137
15	C22a-H22e···F2b	0.98	2.25	2.868(18)	122
16	C2-H2···F1b	0.95	2.48	2.977(18)	113

interaction of O3 of the triflate ions attached to the *cis*- chain with the methine hydrogen of the *trans*- isomer (H4, contact # 2 Table 2.12) also places *trans*- isomers in chains parallel to *c*- (and gives bilayer sheets parallel to the *ac*- plane), Figures 2.17b and 2.17c. The *trans*- chains are further supported by with their confused pyrazolyl hydrogens as

donors (H1n, H1) and oxygen atoms of disordered triflate ions (contacts 9 and 10, Table 2.12). The *ac*-bilayer sheets are stacked along the *b*- direction by the interaction between O2 on one sheet and a 5-methyl hydrogen of a pz* group (H24b) on an adjacent sheet (contact 5, Table 2.12). The other non-covalent interactions listed in Table 2.12 further secure this structure. This packing arrangement places the minor disorder triflate component within voids of the supramolecular framework. The minor component is still hydrogen bonded to the *trans*- isomer but does not bridge neighboring *trans*- isomers within the polymer chain. Moreover, there is no hydrogen bonding to the *cis*- isomer. It is further noted that at 250 K, the overall connectivity is retained but non-covalent interactions lengthen. Also, the minor triflate disorder component is not observed. Instead, there are solvent accessible voids 162 $Å^3$ in the same location as in the 100 K structure. Thus, the *cis*- component of *co*-**1** is more loosely packed than the *trans*- component at both temperatures and presumably is freer to adopt a LS configuration at low temperature.

B. Powder X-ray Diffraction.

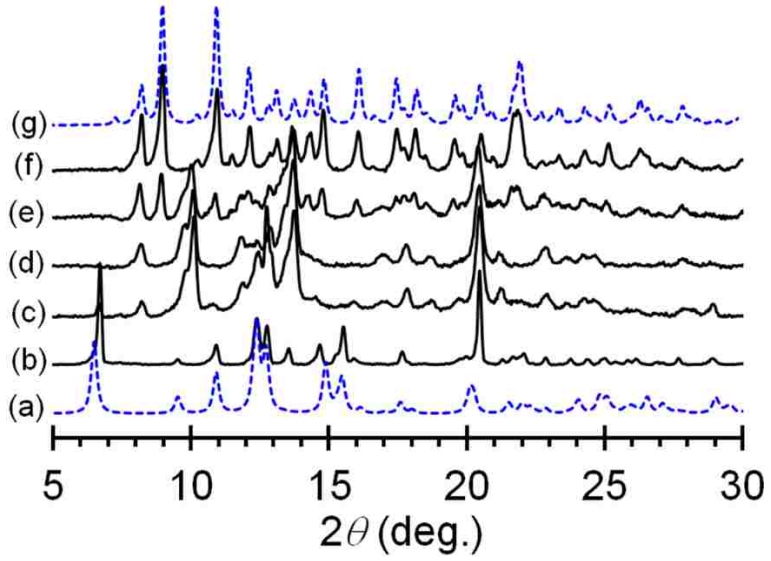

Figure 2.18. Calculated (blue dashed traces) and experimental (black traces) Powder X-ray diffractograms (Cu Kα radiation, 295 K) for various stages of desolvation of $[Fe(^{H}L^{*})_2](OTf)_2 \cdot 2CH_3CN$, *trans*-**1**$\cdot 2CH_3CN$. (a) Calculated pattern for *trans*-**1**$\cdot 2CH_3CN$. (b) Air-dried, ground crystals of *trans*-**1**$\cdot 2CH_3CN$. (c) Crystals of *trans*-**1**$\cdot 2CH_3CN$ dried under vacuum at 295 K for 5 min to give pink powder. (d) Crystals of *trans*-**1**$\cdot 2CH_3CN$ dried under vacuum at 295 K 1 h. to give colorless powder. (e) Crystals of *trans*-**1**$\cdot 2CH_3CN$ dried under vacuum at 343 K 1 h. (f) crystals of *trans*-**1**$\cdot 2CH_3CN$ dried under vacuum at 343 K 12 h. (g) Calculated pattern of *trans*-**1** from 250 K single crystal X-ray diffraction experiment.

The multiple crystal forms of **1** identified by single crystal X-ray diffraction studies prompted an investigation into the structural nature of the bulk crystalline and powder samples. First, it was found that the PXRD patterns of freshly ground bulk crystalline samples of *trans*-**1** or *co*-**1** matched those calculated from their single crystal X-ray diffraction data. The data for ground, air-dried crystals of *trans*-**1**$\cdot 2CH_3CN$ mostly matched the calculated pattern but had reflections for desolvated forms, Figures 2.18a and b. If the initially violet *trans*-**1**$\cdot 2CH_3CN$ is subjected to room temperature evacuation samples become colorless and PXRD data shows a new phase (Figure 2.18c and d) for *trans*-**1**$\cdot CH_3CN$, as suggested by NMR and combustion analysis. This new phase only very slowly (several hours) converts with heating at 70°C under vacuum to *trans*-**1** (Figures 2.18e-g) In contrast, samples of *trans*-**1**$\cdot 4CH_3CN$ readily lose solvent even at room temperature (neither heating nor evacuation is necessary) to give PXRD patterns identical with *trans*-**1** (Figure 2.19).

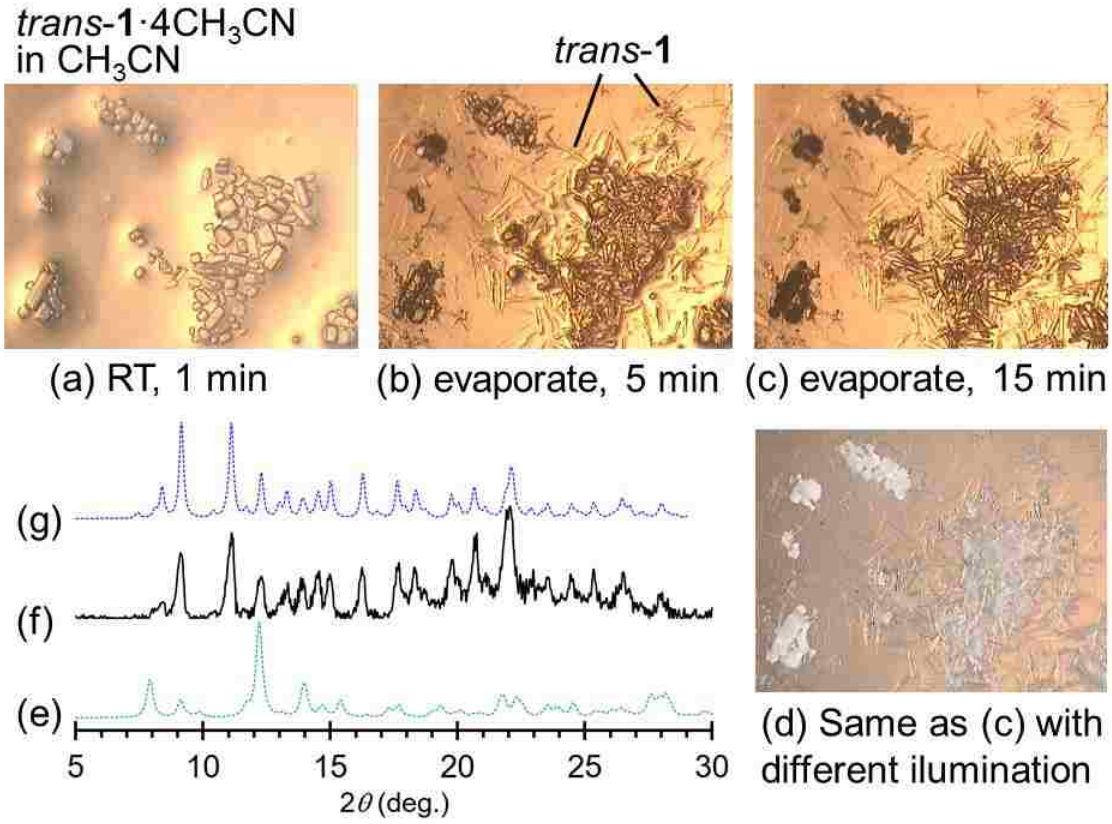

Figure 2.19. Photographs of crystals of *trans*-**1**·4CH_3CN in a thin film of mother liquor (CH_3CN) taken at intervals after removing from freezer and warming on illuminated microscope slide stage. (a) Within 1 min of removal. (b) After 5 min. (c) After 15 min, sample is now dry. (d) same as (c) but with different lighting, showing colorless nature. (e) calculated pattern for *trans*-**1**·4CH_3CN. (f) experimental PXRD pattern of desolvated crystals. (g) calculated pattern for *trans*-**1**.

Samples of as-formed powders of **1** crystallized at room temperature by Et_2O vapor diffusion had PXRD patterns were consistent with an admixture of crystalline phases *cis*-**1** and *trans*-**1**. It is noted that because of the similarity in unit cells at room temperature these two PXRD patterns are strikingly similar (Figure 2.1) but are distinguishable by peaks at: 2θ (degrees) = 7.3 (*trans*), 14.5 and 14.7 (*cis*) versus 14.4 and 14.8 (*trans*), 19.4 (*cis*) versus 19.6 (*trans*), 25.0 (*cis*) versus 25.2 (*trans*), 27.8 (*trans*), and 29.4 (*cis*). Finally, the PXRD patterns reveal that the Et_2O-washed, colorless, as-

formed powders of **1** are mixtures *trans*-**1**, *cis*-**1**, and sometimes *co*-**1**. The relative composition of the mixture depends on the temperature of the reaction mixture and that at which solvent was removed under vacuum; both are controlled by solution isomerization equilibrium (vide infra) where high temperatures favor greater proportions of *cis*-**1** and/or *co*-**1** whereas room temperature reactions and distillations gave mixtures that favored *trans*-**1** (Figures 2.1 and 2.20).

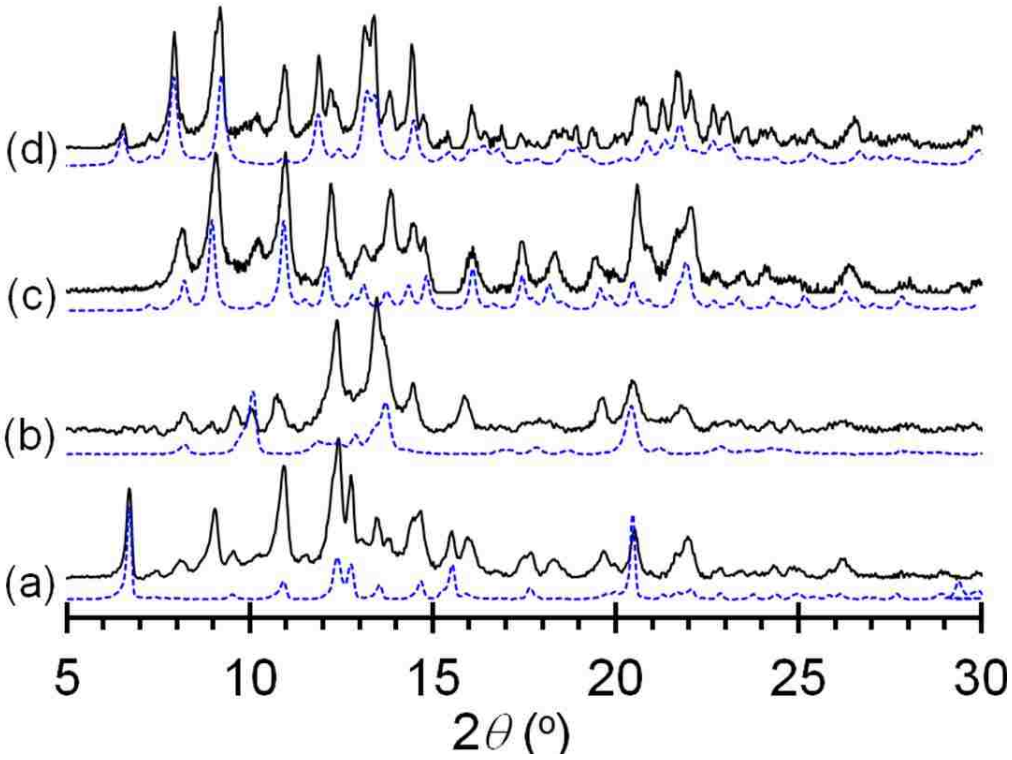

Figure 2.20. Representative PXRD patterns for powders of **1** obtained under different conditions (black lines). Calculated patterns for main component of mixture shown as blue dashed traces. (a) As-formed lilac-colored solid obtained after 1h mixing at room temperature followed by room temperature vacuum distillation, but prior to Et_2O wash. The residue is a mixture of mainly *trans*-**1**·2CH_3CN (blue trace), *trans*-**1**·CH_3CN and *trans*-**1**. (b) Similar to (a) but for the pink powder obtained after incomplete Et_2O wash. The blue trace is for *trans*-**1**·CH_3CN. Peaks for *trans*-**1** are also present. (c) Similar to (a) and (b) but for colorless powder obtained after complete Et_2O wash. The blue trace is for *trans*-**1.** (d) Colorless powder obtained after 4h mixing at 70 °C followed by vacuum distillation using external 40 °C water bath. The blue trace is for *co*-**1**. Peaks for both *cis*-**1** and *trans*-**1** are also evident (See Figure 2.1).

The composition of the as-formed powder depends on the temperature (and time) that the reaction mixture was stirred, the temperature at which solvent was removed, the rate for solvent removal, and the completeness of the Et_2O washing procedure. Reactions performed at room temperature give mainly *trans*-**1** isomer (Figure 2.20a-c). If solvent is removed under vacuum without heating, the residue prior to Et_2O washing will be colored between lilac and rose-pink indicating variable amounts of *trans*-**1**·xCH_3CN (x = 1, 2) (Figures 2.20b and 2.20c). The Et_2O washing helps drive of CH_3CN to give mainly *trans*-**1** (weak intensity reflections at 2θ = 7.3 and 27.8°, Figures 2.20c and 2.1) with some *cis*-**1** (peak at 2θ = 14.5°, Figure 2.20c and 2.1). If the preparative reaction is heated and then solvent is removed using a warm (ca. 40-50°C) water bath to maintain temperature, then variable amounts of *co*-**1** could be detected (at 2θ = 6.5, 13.4, and 19.0°) in addition to those for *cis*-**1** and *trans*-**1**, Figure 2.20d. Heating a solution to dryness under atmospheric pressure produces mainly *cis*-**1** (maximum ca. 25% *trans*-**1**, Figures 2.1b). Heating favors the formation of *cis*- isomer.

Magnetometry. The temperature dependence of the magnetic properties of air-dried crystals of *co*-**1**, a powder sample of *cis*-**1** contaminated with minor amounts of *trans*-**1**, and phase pure powders of *trans*-**1** and *trans*-**1**·CH_3CN were investigated by SQUID magnetometry. Figure 2.21

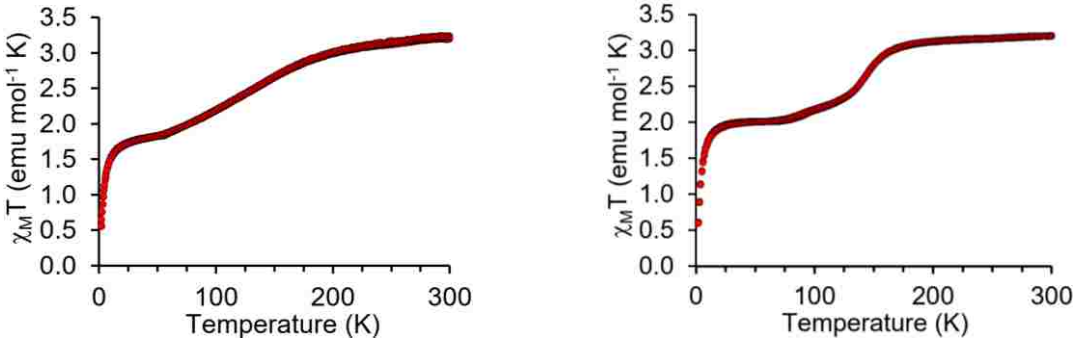

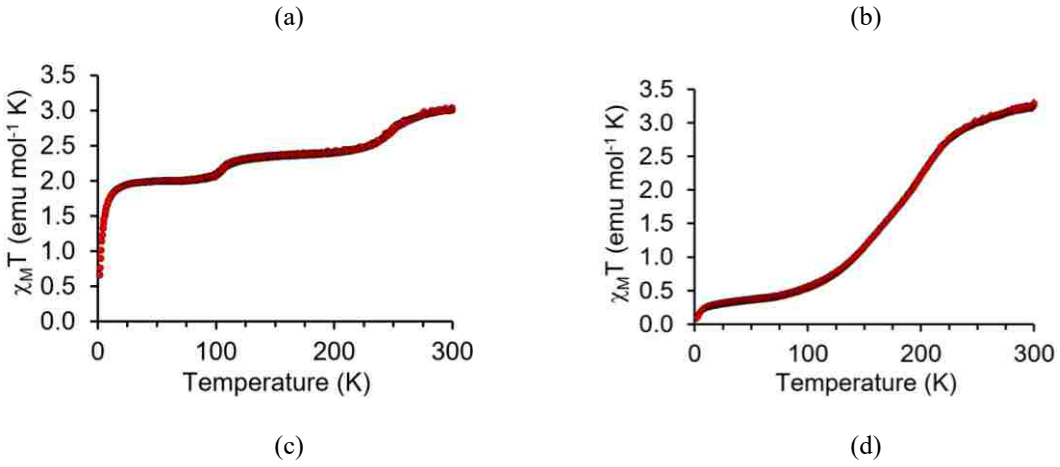

Figure 2.21. Magnetic susceptibility data obtained from hand-separated crystals of (a) *co*-**1** (b) *cis*-**1** (c) *trans*-**1**, and (d) *trans*-**1**·CH_3CN.

gives the magnetic data, plotted as χ_mT versus T. The magnetic data for *co*-**1** (Figure 2.21a) shows a gradual SCO beginning near 300 K (χ_mT = 3.2 cm^3Kmol^{-1}, 100 % HS; theor. χ_mT = 3.25 cm^3Kmol^{-1} with orbital angular momentum contribution to spin-only moment) that stops after χ_mT reaches 1.8 cm^3Kmol^{-1} at 80 K (68% HS, 32% SCO). This behavior is aligned with the crystallographic data that showed only the *cis*- component undergoes partial SCO. The χ_mT value at 100 K of 2.2 cm^3Kmol^{-1} indicates 23% SCO which is on par with 31 ± 6% % SCO estimated from bond distance analysis. As shown in Fig. 2.21b, χ_mT in *cis*-**1** maintains a constant value between 300 K to about 165 K of 3.2 cm^3Kmol^{-1} consistent with 100% HS Fe(II). Between 80 to 20 K, χ_mT value drops to a constant value of 2.0 cm^3Kmol^{-1}, indicating about 72% HS Fe(II). Given the X-ray structural data that showed a rather long average Fe-N bond distance of 2.11(2) Å at 100 K (consistent with an incomplete 30 ± 5% spin crossover) and a triflate disordered in a near 2:1 ratio over two sites, we tentatively ascribe the unusual magnetic behavior to be the result of the spin crossover of the minor disorder component in *cis*-**1**; the majority of

the sample remains HS. The subtle "hump" in the curve near 100 K is due to *trans*-**1**, as described next. For *trans*-**1**, $\chi_M T$ at 300 K is 3.1 cm^3Kmol^{-1} and reduces to a constant value of 2.0 cm^3Kmol^{-1} upon cooling to 80 K or below, in accord with about 28% SCO on cooling, similar to *cis*-**1**. As opposed to the gradual transition in *cis*-**1**, that of *trans*-**1** occurs in two unequal steps at T_1 = 250 K (18 % SCO) and T_2 = 105 K (10 % SCO) with the former being more gradual (temperature range of transition, ΔT, ~ 78 K) than the latter (ΔT ~22 K). The monoclinic/triclinic crystal phase transition is responsible for the abruptness of the low temperature SCO transition. In particular, the 10 % SCO of this second step observed from the magnetomety data is similar to the 8.5% minor component of the disordered triflate associated with the LS component of the HS/LS iron site in the 100 K structure. Finally, the sample of *trans*-**1**·CH_3CN of unknown structure undergoes a complete but gradual SCO with $T_{1/2}$ of 156 K.

C. Solution Properties.

The properties of the various crystalline forms in solution were investigated first by their crystallization behavior and then by ^{1}H NMR spectroscopy. First, dissolution of any of the crystalline forms followed by either evaporation or Et_2O vapor diffusion over about 16 h (or longer) produces a mixture of crystalline forms indicating that the complexes undergo isomerization in solution. When violet crystals of *trans*-**1**·2CH_3CN are dissolved in CH_3CN at room temperature, the resulting solution is colorless and paramagnetic (μ_{eff} = 5.0 μ_B), indicating that the LS nature of this complex is due to crystal packing effects (vide infra, DFT). The ^{1}H NMR spectrum of C_{2h} symmetric *trans*-**1**·2CH_3CN (or of *trans*-**1**·4CH_3CN) immediately after dissolution consists of six

resonances: five for the hydrogens of the complex and one for CH_3CN. The resonance near 20 ppm consists of three overlapping signals, which is evident from integration and VT NMR experiments (Figure 2.22).

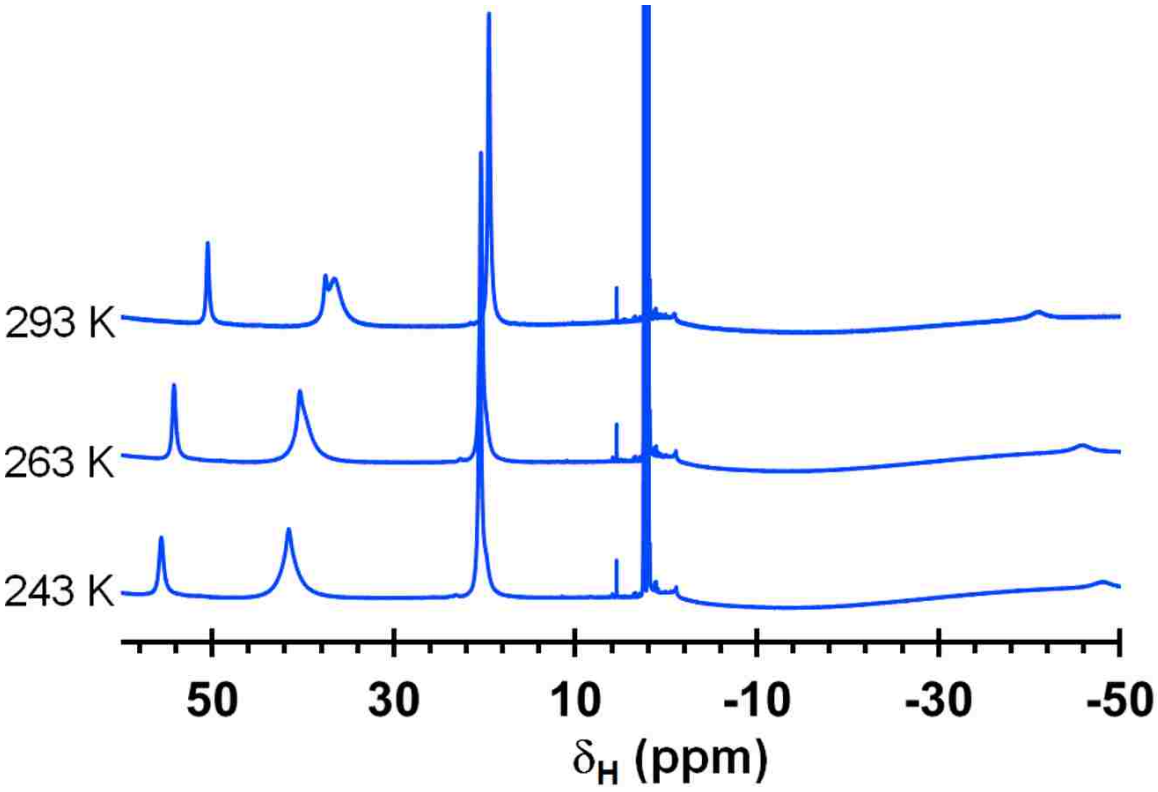

Figure 2.22. Overlay of ^{1}H NMR spectra of *trans*-**1** $2CH_3CN$ in CD_3CN at different temperatures.

Over time, new resonances characteristic of a C_2 symmetric *cis*- isomer (notably near 51, 48, 45, and 21 ppm, Figures 2.23 and 2.24) grow in intensity at the expense of those for *trans*-**1** until an equilibrium mixture of *trans*- and *cis*- isomers is reached. By monitoring the *trans*- to *cis*- isomerization at 22, 50, 60, and 70 ºC, full kinetic and thermodynamic parameters for the equilibrium (Equation 1) were obtained (see

trans-**1** ⇄ *cis*-**1** K = [*cis*-**1**]/[*trans*-**1**] ……..eq 1

below for full details). The *trans*- to *cis*- isomerization reaction (forward reaction Equation 1) is first order in *trans*-**1** with a half-life of 36.5 hr at 295 K and only 19.4 min at 343 K. The activation barrier for this conversion is only 83 kJ/mol, which is much smaller than typical metal –nitrogen bond dissociation enthalpies (ca. 300-400 kJ/mol).[100] Thus, the isomerization likely occurs via bond stretching and torsional modes of vibration rather than

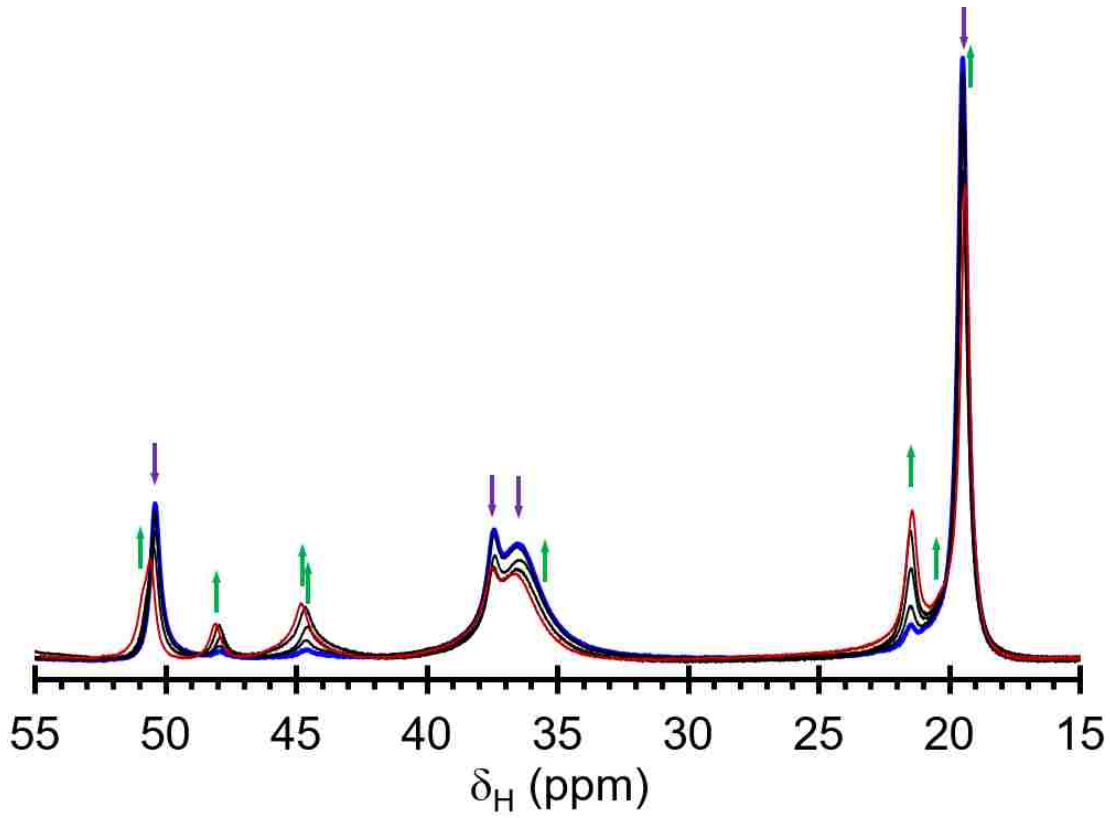

Figure 2.23. Overlay of the downfield portions of the 295 K ^{1}H NMR spectra of a 0.02 M solution of *trans*-**1**·2CH_3CN in CD_3CN acquired at five times after dissolution: 5 min (blue), 240 (black), 480 (black), 1380 (black), and 1800 min (red). The green arrows highlight emergence of resonances for the *cis*- isomer while the purple arrows indicate the receding resonances for the *trans*- isomer.

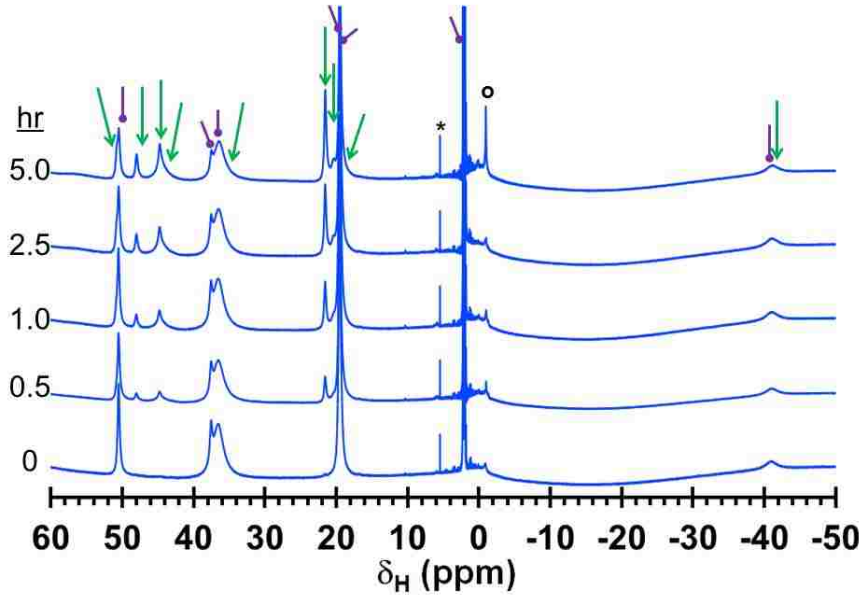

(a)

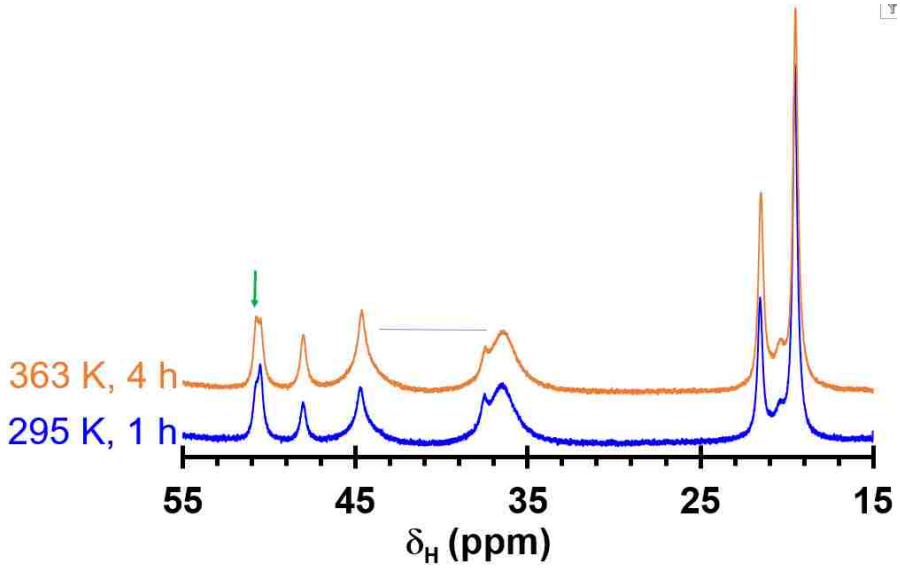

(b)

Figure 2.24. (a) Full ^{1}H NMR spectrum (CD_3CN, 295 K) showing isomerization of *trans*-**1** to a mixture of *cis*- (green arrows) and *trans*- (purple rounded pins) isomers. * and o in top spectrum are for CH_2Cl_2 (added for reference) and silicon grease (accidental). (b) ^{1}H NMR spectra for **1** formed in-situ by adding 2 equivalents ligand to $Fe(OTf)_2 \cdot CH_3CN$ before (blue spectrum, bottom) and after (orange spectrum, top) heating at 70°C. The latter spectra was acquired at room temperature minutes after removal from external oil bath. The green arrow shows resonance for

cis- isomer proton and horozontal line can be used to visually see enrichment of *cis*- isomer with heating.

by dissociation. Supporting this assertion, is that when solutions of **1** are spiked with excess ligand, the spectrum consists of two separate sets of resonances, one set for **1** (as a mixture of *cis*- and *trans*-) and one set for the ligand; the ligand exchange is slow on the timescale of the experiment. At room temperature (295 K), the isomerization proceeds until an equilibrium *cis*/*trans* ratio ($K_{eq,\,295}$) of 0.66 is achieved. At 343 K, the equilibrium favors the *cis*- isomer, $K_{eq,343} = 2.2$. The van't Hoff plot at four different temperatures (Figure 2.26) gives $\Delta H = +22$ kJ/mol and $\Delta S = +69$ J/K·mol. The small positive value of ΔS is expected due to the lower symmetry of the *cis*- versus *trans*- isomer. However, the endothermic nature of the *trans*- to *cis*- transformation was not expected (nor was it predicted by DFT, vide infra) given the otherwise identical HS FeN_6 kernels. The enthalpic contribution must originate from discrepancies in ion pairing between each isomer, or less likely in solvation, due to the different disposition of N-H bond donors. Perhaps the smaller electron repulsion of hydrogen-bonded triflate anions in the *trans*- versus *cis*- isomer may be responsible for the difference in enthalpy. We will further examine this line of query in future studies that probe anion effects on SCO of this complex cation. The difference in the apparent composition of the as-formed powders depending on whether the solution is heated or not during evaporation (Figure 2.20) originates from the values of ΔH and ΔS which indicate that the *cis*- isomer is favored above 311 K (38 ºC). In a related manner, NMR monitoring of the formation of **1** in-situ by dissolving the ligand and $Fe(OTf)_2 \cdot 2CH_3CN$ in CD_3CN initially shows a mixture of isomers that slightly favors *trans*-**1** but that converts rapidly to the equilibrium

mixture after heating (Figure 2.24b and 2.2). The ability to isolate pure *trans*-**1**·2CH_3CN from solutions of as-formed powders of **1** in CH_3CN when stored in a freezer (253 K) is facilitated by $K_{eq,253}$ = 0.15 and solubility differences in isomers. Finally, the limited boiling temperature of CH_3CN (355 K), the equilibrium constant at that temperature, $K_{eq,355}$ = 2.3, and the larger rate constant of the reverse versus the forward reaction in Equation 1, all have hampered the ability to isolate pure *cis*-**1** in the bulk from this solvent.

D. Details of Kinetic and Equilibrium NMR Analysis.

Solutions of known concentration of *trans*-**1**·2CH_3CN in CD_3CN (ca. 0.01-0.04 M = [*trans*-**1**]$_0$) were prepared immediately before inserting into a preheated NMR magnetometer (t_0 = 0 min, taken to be 100% *trans*-**1** and Temperature = 22, 50, 60, and 70 ^oC). The ^1H NMR spectrum acquired after shimming (recorded time, t_1 = ca. 5-7 min). Then spectra were acquired at designated intervals thereafter (i.e, every 5 min at 60^{o}C or every 2 min at 70^{o}C, etc.). At low temperature (295 K), a resonance for *cis*-**1** at 50.7 ppm (2 H, presumably for one of two sets of resonances for H_4 pz* hydrogens; the other set appears at δ_H = 48.0 ppm) can be seen growing in next to that at 50.5 ppm (4 H) for *trans*-**1**. While these resonances be quantified by deconvolution, they overlap in higher temperature spectra. Thus, the following procedure was used to quantify the relative amounts of *cis*-**1**:*trans*-**1**. The spectra were processed and were subject to least square baseline correction using the Spinworks program (SpinWorks 4.2.0, Copyright © 2015 Kirk Marat, University of Manitoba). The integration of the 48.0 ppm resonance (295 K, shifting to 43.0 ppm @ 343 K), Int_{48}, was set to 2 H, then the overlapping resonances near 50.5 ppm (295 K, shifting to 45.2 ppm @ 343 K), Int_{51}, were integrated

together. The fraction of *trans*-**1**, χ_{trans}, was taken as $(Int_{51} - Int_{48})/ (Int_{51} + Int_{48})$ while the fraction of *cis*-**1**, χ_{cis}, is then $(2\ Int_{48})/ (Int_{51} + Int_{48})$ or $1 - \chi_{trans}$. This procedure was repeated twice by separate individuals and all three values were averaged to minimize/establish errors in data processing procedure. Then $[trans\text{-}\mathbf{1}]_t = \chi_{trans}[trans\text{-}\mathbf{1}]_0$ and $[cis\text{-}\mathbf{1}]_t = [trans\text{-}\mathbf{1}]_0 - [trans\text{-}\mathbf{1}]_t$. A representative plot of $[trans\text{-}\mathbf{1}]_t$ versus time is found in the left of figure 2.25. The initial rate of *trans*-**1** to *cis*-**1** conversion was taken as the best line fit through plot of ln [*trans*-**1**] versus time over the first 50 min (right of Figure 2.25) where the slope is the negative of the rate constant k. The equilibrium concentration of *trans*-**1**, $[trans\text{-}\mathbf{1}]_{eq}$, is taken as the average of the [*trans*-**1**] values from 100 to the 180 min. The equilibrium concentration of *cis*-**1**, $[cis\text{-}\mathbf{1}]_{eq}$, then equals $[trans\text{-}\mathbf{1}]_0 - [trans\text{-}\mathbf{1}]_{eq}$. The van't Hoff and Erying plots are found in Figure 2.26.

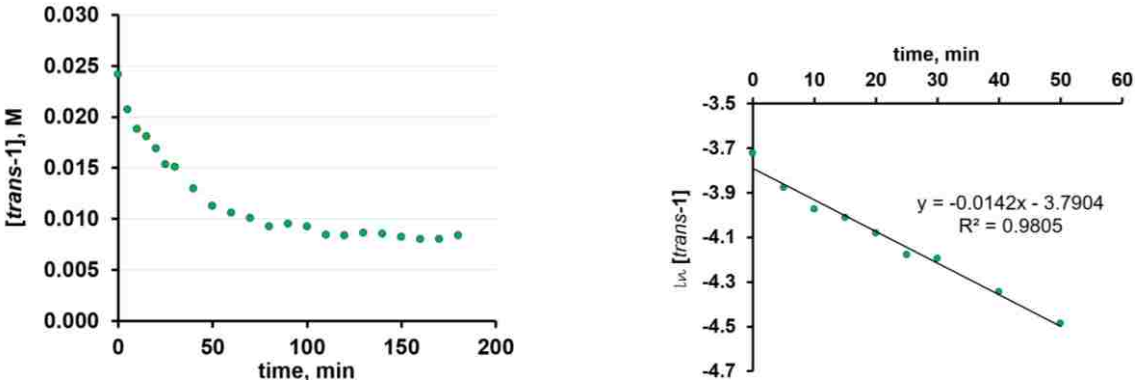

Figure 2.25. Left: Plot of [*trans-**1***] as a function of time at 333 K. Right: Plot of ln [*trans*-**1**] versus time with best fit line shown.

Table 2.13. Temperature dependence of rate constants and equilibrium constants.

T (K)	T^{-1} (K^{-1})	K_{eq}	ln K_{eq}	k	ln k	$t_{1/2}$ (min)
295	3.390×10^{-3}	2.230	0.8020	3.166×10^{-4}	-8.058	2189
323	3.096×10^{-3}	1.765	0.5682	7.142×10^{-3}	-4.942	97.03

333	3.003 x10^{-3}	1.270	0.2390	1.420 x10^{-2}	-4.255	48.80
343	2.915 x10^{-3}	0.650	-0.4308	3.574 x10^{-2}	-3.331	19.39

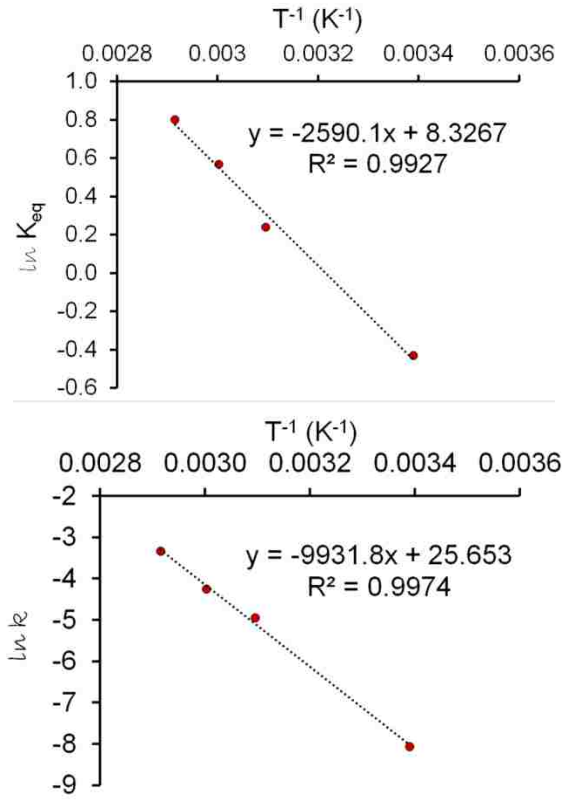

ΔH = +21.53 kJ/mol E_a = 82.57 kJ/mol

ΔS = +69.23 J/mol A = 1.383x10^{11} s^{-1}

Figure 2.26. Van't Hoff (left) and Erying (right) Plots for *trans*-**1** ⇄ *cis*-**1**.

E. DFT Calculations. To gain further insight into the nature of the electronic ground state and relative stability of isomeric dications in **1**, theoretical calculations were performed using a density functional method, (OPBE/def2-SV(P) (C,H,N), def2-QZVPP (Fe)/PCM (CH_2Cl_2), that has been successfully used for other iron complexes that undergo spin crossover.[90] First, for both isomers DFT calculations predict the quintet state to be lowest in energy at 298 K. This is in line with the experimental observation that, in solution, both isomers are paramagnetic HS species. The singlet state was higher energy by 21 and 22 kJ/mol for the *trans*- and *cis*- isomers respectively. These small values of spin-state splitting are in the range where spin crossover is expected. Finally, the isomers are nearly degenerate, with the *trans*- isomer being only 1-2 kJ more stable than the *cis*- isomer in either the quintet or singlet states. This slight preference may be due to the lower inter-ligand repulsions in the *trans*- (two pz* methyl/pz* methyl clashes) versus the *cis*- (three pz* methyl/pz* methyl clashes) isomer, Figure 2.27. If the isomers are

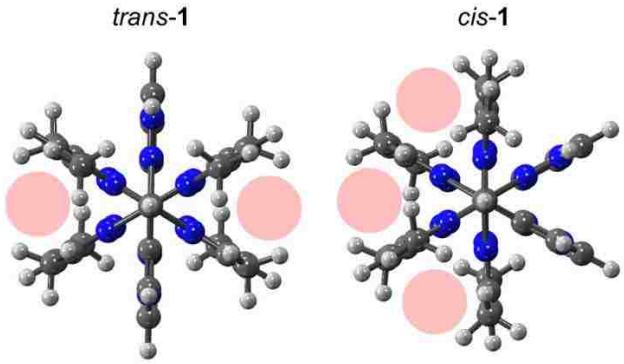

Figure 2.27. DFT calculated geometries of LS form of each isomer of **1** viewed down the H-$C_{methine}\cdots$Fe vector, showing areas of interligand steric interactions as filled pink circles.

degenerate, then one may expect a statistical 2:1 ratio of *cis*:*trans* isomers (the value achieved in the high temperature solution NMR studies). Thus, the DFT calculations are surprisingly in rather good qualitative agreement with the experimental solution isomerization equilibrium despite not accounting for potential electrostatic interactions with anions. As mentioned above, perhaps neglecting these latter interactions in the computations is responsible for the discrepancies between calculated and experimental ΔH and ΔS values.

2.3. CONCLUSIONS

Complex **1**, $[Fe(^{H}L^{*})_2](OTf)_2$, was initially prepared to compare electronic and magnetic properties with the parent complex $[Fe(^{H}L)_2](OTf)_2$, **2**, (with a $T_{1/2}$ near 360 K). It was expected that the interligand steric interactions among methyl substituents on the pyrazolyl rings in **1** should lower $T_{1/2}$ (i.e. stabilize the HS state) versus the parent complex. Indeed, **1** was found to be HS in solution at room temperature in contrast to the LS complex **2**. A secondary benefit of adding methyls to the normal pyrazolyl rings, is that **1** enjoyed much greater solubility in CH_3CN than **2** which greatly facilitated the solution NMR studies of the former. The fairly significant temperature dependence of the solution isomerization equilibrium (Equation 1) observed for **1** by NMR was surprising since both the enthalpic and entropic contributions to the equilibrium were expected to be minimal based on considering only FeN_6 cores and, perhaps, the change in point group symmetry. It would seem that interactions with the triflate anions play an important role in governing the temperature dependence. The *trans*- isomer not only has fewer interligand steric interactions than the *cis*- isomer, but if the triflate ions here hydrogen bonded to the acidic N-H group in each isomer, then the triflate ions in the *trans*- isomer would be further apart

than in the *cis*- isomer minimizing anion-anion repulsions making the *trans*- isomer more stable than the *cis*- isomer. Regardless, the temperature dependence of the equilibria provided insight into conditions that would favor one isomer over another. Indeed, six different crystalline forms of **1** could be prepared; *cis*-**1**, *co*-**1**, and *trans*-**1** xCH_3CN (x = 0, 1, 2, 4). It is worth comment that the rich structural chemistry, as observed for **1**, was not discovered in the parent complex, $[Fe(^{H}L)_2](OTf)_2$. Such behavior was missed due in part to the relatively high pseudo-symmetry of the 'confused' and 'normal' pyrazolyl rings that results in crystallographically-disordered dications which prevented definitive identification of isomers in the solid state and the low solubility in solution that stymied NMR characterization. It is also of interest that CH_3CN solvates of cis-**1** have neither been isolated nor identified by PXRD. Perhaps, this is fortuitous consequence of the solution equilibrium. It is also possible that the juxtaposition of the two N-H groups allows for chelation of one triflate anion in solution (the other anion being either outer sphere or associated with the acidic methine) that outcompetes solvent for hydrogen bonding. In the case of the *trans*- isomer, only monodentate coordination to the anion or solvent is possible, and gives rise to the observed mixture of solvate and solvate-free forms. Regardless, five of the six crystalline forms were HS in the solid state at room temperature with *trans*-**1**·2CH_3CN being the LS exception. The crystal packing of this latter derivative is remarkably efficient being denser than *co*-**1** (and only slightly less dense than *trans*-**1** or *cis*-**1**) despite having two solvate CH_3CN molecules included in the lattice. Four of the derivatives (*cis*-**1**, *co*-**1**, and *trans*-**1** xCH_3CN (x = 0, 1) showed SCO by magnetometry and only the structure of the latter remains unknown. It is now clear after examining the average pz twist angles of *cis*-**1** (6°), *co*-**1** (*cis*- component 4°, trans- component 6°), *trans*-

1·4CH_3CN (10°) and that of $[Fe(^{Ts}L)_2](BF_4)_2$ (8°) reported earlier, that the empirical '11° rule' needs to be amended, at least for N-confused scorpionates, to state: if pz twisting is above 11° then SCO will not be observed, but if pyrazolyl ring twisting is less than 11°, SCO is not guaranteed. Clearly other ligand distortions (pz-tilting < 175°) or other crystal packing effects are sufficient to prevent SCO of these iron(II) scorpionates. For three derivatives with known structures and that undergo SCO, the triflate anion plays an important role in their magnetic behavior. In all three cases, at least one of the triflate ions is disordered and the minor disorder component is responsible for SCO behavior. The ability for the triflate to adopt different geometries thereby giving more room for HS/LS interconversions in the dications may be promoted by the incompatibility of the C_{3v} point symmetry of the anion with two-fold point symmetry of the dication in most (the observed) space groups, forcing the anion to occupy crystallographic general positions (and increasing probability for disordered structures). Finally, one of the unique design features of these N-confused C-scorpionates is the availability of an N-H moiety on the confused pyrazolyl ring that can be involved in hydrogen-bonding interactions with either anions or solvent. It remains unclear whether these weak hydrogen bonding interactions have any effect on cooperativity, as both abrupt and gradual SCO transitions have been observed among the four reported examples. Future studies will be directed toward developing a better understanding of the relationships between symmetry and hydrogen bonding capabilities of anions on the cooperativity of SCO in these systems by using judicious choices of hydrogen bonding acceptors.

CHAPTER 3: SYNTHESIS AND REACTIVITY OF SILVER COMPLEXES OF NITROGEN CONFUSED SCORPIONATE LIGANDS

3.1. Introduction

Scorpionate ligands, formerly known as Trofimenko's tris(pyrazolyl)borates, Tp^x, are one of the classic and well-developed N-donor ligands in coordination chemistry.[101] The 'scorpionate' name has been extended and includes all facially-coordinating tripodal ligand analogues such as Reglinski's tris(thioimidazolyl)borate[101b], soft scorpionates (Tm^R),[102] C-scorpionates such as tris(pyrazolyl)methane (Tpm^x)[103], and tris(pyrazolyl)methanesulfonate, Tpms.[104] The presence of B-H moiety in the first generation B-scorpionates ligands had a tendency to reduce silver(I) to the zero valent metal Ag(0). The chemistry of silver scorpionates has been widely explored ever since it was learnt that silver reduction could be inhibited by removing B-H bonds, or by increasing steric bulk on the pyrazolyl ring especially at the 3-position and/or by introducing electron-withdrawing groups on the pyrazolyl.[105] The first report of a Ag-catalyzed activation of carbon-halogen bonds through a carbene insertion process occurring at mild conditions was from the Dias group. The Dias group[106] synthesized a highly fluorinated trispyrazolyl ligand, $Tp^{(CF3)2}$ [$HB(3,5\text{-}CF_3)_2Pz)_3$] which greatly stabilizes the $AgTp^{(CF3)2}$ complex. This $AgTp^{(CF3)2}$ complex was then also used to catalyze carbene insertion into C-H bonds of cyclic and acyclic hydrocarbons and aromatic C=C bonds at room temperature. The Perez group developed $AgTp^x$ complexes which catalyzed the aziridination of alkenes, dienes, amination of alkanes, unexpected N-N bond formations and recently Perez's $Ag[PhB(CH_2PPh_2)_3](PPh_3)$ catalyzed aziridination of styrene but in lower yields than the copper analogues. [13,14,107]

Compared to $AgTp^x$ and other anionic B-scorpionates ligands the reaction chemistry of AgTpms or $[Ag_n(Tpm^x)_m]^+$ were less explored because of the difficulty in their synthesis and isolation.[18-19] In 1984, Elguero and coworkers developed an improved procedure for the synthesis of these ligands.[108] After this breakthrough, the chemistry of tris(pyrazolyl)methanes began to receive attention and remarkably grew in the past decades.[104] Given the efficient aziridination and amination catalysis reported by Schomaker, He and Perez groups using silver complexes of charge neutral nitrogen donor ligands, similar chemistry might be expected for tris(pyrazolyl)methanes but only a handful reports can be found for tris(pyrazolyl)methanes for the silver metal. [109-114]

Our group has recently introduced a new class of tris(pyrazolyl)methanes, the nitrogen-confused C-scorpionates, [20] where one of the three pyrazolyl rings is bound to the central methine carbon atom via a pyrazolyl ring carbon atom rather than the more usual nitrogen atom. Synthesis of new N-confused C-scorpionate ligands with two 'normal' pz* groups (=3,5-dimethylpyrazol-1-yl) and a 'confused' pyrazolyl with either an N-H, ^{H}L*, or an N-Tosyl (Tosyl = p-toluenesulfonyl), TsL*, bound to a central methine carbon has been previously described.[20] These bulky ligands complement those previously described, ^{H}L and ^{Ts}L, that had less-bulky, unsubstituted, 'normal' pyrazol-1-yls. For these four related N-confused scorpionate ligands, the 2:1 and 1:1 ligand:silver complexes were prepared and characterized both structurally and spectroscopically. The complexes' stoichiometric reactivity and catalytic activity for aziridination of styrene were also reported. However, these silver complexes show lower activity for catalytic aziridination compared to the previously reported $AgTp^x$ complexes. The purpose of this thesis work is to fully investigate if by further increasing the steric bulk on the pyrazolyls

these current catalysts can be made more competitive with other previously reported catalysts for intermolecular aziridination reactions. In this contribution, the preparation of two new N-confused C-scorpionates, $^{Ts}L^{ipr}$ and $^{H}L^{ipr}$, each with two 'normal' 3,5-diisopropylpyrazolyl groups, and either an N-tosyl or N-H group on the 'confused' pz is described. Also, described in this chapter are the preparation of the silver complexes of these bulky ligands and their potential as catalysts for nitrene transfer reactions.

3.2. Experimental

General considerations. The compound ^{Ts}pzC(O)H (Ts = *p*-$SO_2C_6H_4CH_3$) was prepared by the literature method.[74] $PhI(OAc)_2$, 3,5-diisopropylpyrazole or H(pz^{iPr2}), H_2NTs and styrene were purchased from commercial sources and used as received. Commercial anhydrous $CoCl_2$, AgOTf (OTf = trifluoromethanesulfonate), and $[Cu(CH_3CN)_4]PF_6$ were stored under argon in a drybox. Commercial solvents ethyl acetate (EtOAc), dichloromethane (DCM), methanol (MeOH) were used as received while diethyl ether (Et_2O), acetonitrile, toluene, and tetrahydrofuran (THF) were dried by conventional means and distilled under a nitrogen atmosphere prior to use. The silver(I) complexes were prepared under argon using Schlenk-line techniques, however, after isolation, were stored and manipulated under normal laboratory atmospheric conditions, unless otherwise specified.

Instrumentation: Melting point determinations were made on samples contained in glass capillaries using an Electrothermal 9100 apparatus and are uncorrected. ^{1}H, ^{13}C, ^{19}F NMR spectra were recorded on a Varian 400 MHz spectrometer. Chemical shifts were referenced to solvent resonances at δ_H 7.26 and δ_C 77.23 for $CDCl_3$ or δ_H 1.94 and δ_C 118.26 for CD_3CN. Abbreviations for NMR: br (broad), sh (shoulder), m (multiplet), ps

(pseudo-), s (singlet), d (doublet), t (triplet), q (quartet), p (pentet), sept (septet), 'confused' pyrazolyl = pz^{cf}, isopropylpyrazolyl = pz^{iPr}

A. Ligands.

$^{Ts}L^{iPr2}$. Method A. An argon-purged solution of 3,5-diisopropylpyrazole (4.57 g, 30.0 mmol) in 20 mL THF was transferred slowly via cannula over 10 minutes to a suspension of NaH (0.75 g, 31.0 mmol) in 20 mL THF under argon atmosphere. To ensure quantitative transfer, the flask originally containing 3,5-diisopropylpyrazole was rinsed with THF (2 × 5 mL) and the washings were transferred to the reaction mixture. After 10 minutes of stirring, thionyl chloride (1.1 mL, 15.0 mmol) was added by syringe slowly over 5 minutes; a colorless precipitate formed during the addition. The suspension was stirred at room temperature for 10 minutes, then $CoCl_2$ (0.065 g, 0.5 mmol) and ^{Ts}PzC(O)H (2.5 g, 10.0 mmol) were added sequentially as solids under an argon blanket. The blue suspension was heated at reflux under argon for 12 h, and then was cooled to room temperature. Solvent was removed by vacuum distillation and the solid residue was dissolved in 200 mL of a 1:1 biphasic mixture of H_2O:ethyl acetate. The organic layer was separated, and the aqueous layer was extracted with dichloromethane (2 × 50 mL). The organic fractions were combined, dried over $MgSO_4$, and filtered. Solvents were removed by rotary evaporation to leave 6.02 g of crude product. The crude product was dissolved in 50 mL of boiling MeOH and the solution was stored at -10 °C for 1 h. The colorless crystalline product (4.5 g) was collected by vacuum filtration and was dried at room temperature under oil-pump vacuum. The mother liquor was concentrated to 10 mL and was stored at -10 °C for overnight to give another 0.3 g of pure product. The yield is 4.8 g (91 %).

Method B. Under an argon atmosphere, a solution of 0.975 g (3.28 mmol) of triphosgene in 20 mL THF was added dropwise to a solution of 3.00 g (19.7 mmol) of 3,5-diisopropylpyrazole and 2.75 mL (mmol) NEt_3 in 80 mL THF. After stirring 16 h at 22°C, the insoluble $HNEt_3Cl$ was removed by filtration and was washed with THF (2 x 10 mL). Solvent was removed from the combined THF fractions by vacuum distillation to leave a 95:5 mixture of $(Pz^{ipr2})_2C{=}O{:}H(pz^{iPr2})$ as a colorless oil that was used directly. ^1H NMR ($CDCl_3$): $(Pz^{ipr})_2C{=}O$: 6.12 (s, 2 H, H_4pz^{iPr}), 3.34 (sept, J = 6.8 Hz, 2 H, $CHMe_2$), 2.97 (sept, J = 6.9 Hz, 2 H, $CHMe_2$), 1.27 (d, J = 6.8 Hz, 12 H, iPr-CH_3), 1.24 (d, J = 6.9 Hz, 12 H, iPr-CH_3), $H(pz^{iPr2})$: 5.95 (s, 1 H, H_4pz^{iPr}), 3.03 (sept, J = 6.8 Hz, 2 H, $CHMe_2$), 1.34 (d, J = 6.8 Hz, 12 H, iPr-CH_3). Next, 2.15 g (9.85 mmol) $^{Ts}PzC(O)H$, 0.0640 g (0.490 mmol) of $CoCl_2$ and 50 mL of toluene were added and the mixture was heated at reflux under argon for 16 h. Then, the resulting blue mixture was cooled to room temperature, and the solvent was removed by vacuum distillation. The residue was partitioned between 100 mL of H_2O and 100 mL of ethyl acetate. The layers were separated, and the aqueous layer was extracted with two 50 mL portions of CH_2Cl_2. The organic fractions were combined, dried over $MgSO_4$, and filtered. Solvents were removed by vacuum distillation to leave 4.04 g (76 %) of white solid. Recrystallization by cooling a boiling MeOH solution (50 mL) to -20 °C for 1 h and filtering gave 3.45 g (65% yield) of pure $\mathbf{^{Ts}L^{iPr2}}$ as colorless crystals after filtration and drying under vacuum.
Mp: 140-143˚C. ^1H NMR ($CDCl_3$): δ_H 8.03 (d, J = 2.7 Hz, 1 H, H_5pz^{cf}), 7.81 (d, J = 8.3 Hz, 2 H, TsAr), 7.64 (s, 1 H, $CH_{methine}$), 7.26 (d, J = 8.3 Hz, 2 H, TsAr), 6.35 (d, J = 2.7 Hz, 1 H, H_4pz^{cf}), 5.85 (s, 2 H, H_4pz^{iPr}), 3.19 (sept, J = 6.9 Hz, 2 H, $CHMe_2$), 2.85 (sept, J = 6.9 Hz, 2 H, $CHMe_2$), 2.40 (s, 3 H, Ts-CH_3), 1.17 (d, J = 7.0 Hz, 12 H, iPr-CH_3), 0.95

(d, J = 6.8, 6 H, iPr-CH_3), 0.91 (d, J = 6.8, 6 H, iPr-CH_3). ^{1}H NMR (CD_3CN): δ_H 8.19 (d, J = 2.7 Hz, 1 H, H_5pz^{cf}), 7.81 (d, J = 8.4 Hz, 2 H, TsAr), 7.62 (s, 1 H, H_{meth}), 7.49 (d, J= 8.4 Hz, 2 H, TsAr), 6.33 (d, J = 2.7 Hz, 1 H, H_4pz^{cf}), 5.98 (s, 2 H, H_4pz^{iPr}), 3.14 (sept, J = 6.8 Hz, 2 H, $CHMe_2$), 2.80 (sept, J = 6.9 Hz, 2 H, $CHMe_2$), 2.40 (s, 3 H, Ts-CH_3), 1.15 (d, J = 6.9 Hz, 12 H, iPr-CH_3), 0.98 (d, J = 6.8, 6 H, iPr-CH_3), 0.87 (d, J = 6.8, 6 H, iPr-CH_3). ^{13}C NMR ($CDCl_3$): δ_C 158.47 (C_5pz^{iPr}), 145.99, 134.34, 131.89, 130.00, 128.51, 109.82 (C_4pz^{iPr}), 100.20 (C_4pz^{cf}), 69.99 (C_{meth}), 28.00, 25.52, 23.73, 23.02, 22.98, 22.83, 21.88 (Ts-CH_3).

^{H}L^{iPr2}. A solution of 20.0 mL of 5.00 M NaOH (aq) (100.0 mmol), 3.50 g (6.52 mmol) $^{Ts}L^{ipr}$, and 20 mL of THF was heated at reflux for 20 min until completion (as monitored by ^{1}H NMR and/or TLC). After the mixture had cooled to room temperature, the THF layer was separated and the aqueous layer was extracted with dichloromethane (2 × 20 mL). The combined organic fractions were dried over $MgSO_4$ and filtered. The organic solvents were removed by vacuum distillation to leave 2.42 g (97%) of pure **^{H}L^{iPr2}** as a white solid. Mp: 137-138 ˚C. ^{1}H NMR ($CDCl_3$): δ_H 7.83 (s, 1 H), 7.50 (d, J = 2.0 Hz, 1 H, H_4pz^{cf}), 6.22 (d, J = 2.0 Hz, 1 H, H_4pz^{cf}), 5.89 (s, 2 H, H_4pz^{iPr}), 3.34 (sept, J = 6.8 Hz, 2 H, $CHMe_2$), 2.92 (sept, J = 6.9 Hz, 2 H, $CHMe_2$), 1.23 (d, J = 6.9 Hz, 12 H, iPr-CH_3), 1.02 (d, J = 6.8 Hz, 6 H, iPr-CH_3), 0.93 (d, J = 6.8 Hz, 6 H, iPr-CH_3); N-H not observed. ^{1}H NMR (CD_3CN): δ_H 11.12 (br, s, 1 H, NH), 7.72 (s, 1 H, H_{meth}), 7.56 (d, J = 2.2 Hz, 1 H, H_5pz^{cf}), 6.11 (d, J = 2.2 Hz, 1 H, H_4pz^{cf}), 6.00 (s, 2 H, H_4pz^{iPr2}), 3.33 (sept, J = 6.9 Hz, 2 H, $CHMe_2$), 2.85 (sept, J = 6.9 Hz, 2 H, $CHMe_2$), 1.19 (d, J = 6.9 Hz, 12 H, iPr-CH_3), 1.07 (d, J= 6.8 Hz, 6 H, iPr-CH_3), 1.00 (d, J= 6.8 Hz, 6 H, iPr-CH_3). ^{13}C NMR ($CDCl_3$):

δ_C 158.72 (C_5pz^{cf}), 152.37, 142.88, 135.36, 105.88 (C_4pz^{cf}), 100.45 (C_4pz^{iPr}), 69.61 (C_{meth}), 28.06 ($CHMe_2$), 25.34 ($CHMe_2$), 23.86 (^{i}Pr-CH_3), 23.05 (^{i}Pr-CH_3), 23.02 (^{i}Pr-CH_3), 22.85 (^{i}Pr-CH_3).

B. Silver Complexes.

General Procedure. A solution of a given ligand (1 or 2 equiv.) in 10 mL of THF was added to a solution of AgOTf in 10 mL of THF by cannula transfer. The flask originally containing the ligand was washed twice with 2 mL of THF, and the washings were transferred to the reaction medium to ensure quantitative transfer of the reagent. After the mixture has been stirred for 2 h, the solvent was removed by vacuum distillation. The colorless residue was washed with two 2 mL portions of Et_2O and was dried under vacuum for an hour. The quantities of the reagents used and of the products obtained and characterization data for each of the four new compounds are given below. An alternative workup in the case where a precipitate was observed is also described.

[Ag($^{Ts}L^{iPr2}$)](OTf) (1a). A mixture of 0.502 g (0.935 mmol) of $^{Ts}L^{ipr}$ and 0.240 g (0.935 mmol) of AgOTf gave 0.609 g (82%) of **1a** as a colorless solid. Mp: 180-182˚C. Anal.Calcd (found) for $C_{30}H_{40}AgF_3N_6O_5S_2$: C, 45.40 (45.43), H, 5.08 (4.95), N, 10.59 (10.70). ^{1}H NMR (CD_3CN): δ_H 8.20 (d, *J* = 2.7 Hz, 1 H, H_5pz^{cf}), 7.75 (d, *J* = 8.4 Hz, 2 H, TsAr), 7.51 (s, 1 H, $H_{methine}$), 7.39 (d, *J* = 8.4 Hz, 2 H, TsAr), 6.19 (s, 2 H, H_4pz^{iPr}), 6.02 (br s, 1 H, H_4pz^{cf}), 3.18 (sept, *J* = 6.7 Hz, 2 H, $CHMe_2$), 2.73 (br m, 2 H, $CHMe_2$), 2.40 (s, 3 H, Ts-CH_3), 1.20 (d, *J* = 6.8 Hz, 6 H, iPr-CH_3), 1.17 (d, *J* = 6.7 Hz, 6 H, iPr-CH_3), 1.12 (br s, 12 H, iPr-CH_3). ^{13}C NMR (CD_3CN): δ_C 162.46, 154.91, 154.69, 147.93, 134.32, 133.96, 131.22, 128.89, 122.16 (q, *J* = 321 Hz, CF_3), 110.02, 100.76, 64.61,

29.36, 26.47, 23.54, 22.96, 22.27, 21.71. ^{19}F NMR (CD_3CN): -79.33 ppm. Crystal of **1a**·acetone suitable for single crystal X-ray diffraction were obtained by layering hexanes over a solution of 50 mg **1a** in 2 mL acetone and allowing solvents to slowly diffuse over 16 h.

[Ag($^{Ts}L^{iPr2}$)$_2$](OTf) (1b): A mixture of 0.506 g (0.943 mmol) of $^{Ts}L^{ipr}$ and 0.121 g (0.472 mmol) of AgOTf gave a colorless precipitate immediately. If the general procedure is followed, then 0.530 g (84%) **1b** is obtained as a colorless solid. If the colorless precipitate was collected by cannula filtration after 2h (in a separate experiment of the same scale), and the insoluble portion is washed with two 2 mL portions of Et_2O and dried under vacuum for an hour, then 0.353 g (56%) of **1b** is obtained a colorless solid. Mp: 128-130˚C. Anal. Calcd (found) for $C_{59}H_{80}AgF_3N_{12}O_7S_3$: C, 53.27 (53.49), H, 6.06 (6.20), N 12.63 (12.39). ^{1}H NMR (CD_3CN): δ_H 8.18 (d, J = 2.8 Hz, 1 H, H_5pz^{cf}), 7.75 (d, J = 8.3 Hz, 2 H, TsAr), 7.53 (s, 1 H, CH_{meth}), 7.38 (d, J = 8.3 Hz, 2 H, TsAr), 6.11 (s, 2 H, H_4pz^{iPr}), 6.01 (br s, 1 H, H_4pz^{cf}), 3.18 (sept, J = 6.7 Hz, 2 H, $CHMe_2$), 2.45 (br s, 2 H, $CHMe_2$), 2.40 (s, 3 H, Ts-CH_3), 1.12 (d, J = 6.7 Hz, 12 H, iPr-CH_3), 0.95 (br s, 12 H, iPr-CH_3). ^{13}C NMR (CD_3CN): 162.26 (br s), 155.32, 154.95 (br s), 147.86, 134.43, 133.62, 131.21, 128.91, 122.17 (q, J = 321 Hz, CF_3), 109.88 (C_4pz^{cf}), 100.78 (C_4pz^{iPr}), 65.76 (C_{meth}), 29.10 (br s), 26.47, 23.74, 23.36, 23.28, 21.89 (br s), 21.69. ^{19}F NMR (CD_3CN): -79.34 ppm.

[Ag($^{H}L^{iPr2}$)](OTf) (2a): A mixture of 0.510 g (1.33 mmol) of $^{H}L^{ipr}$ and 0.343 g (1.33 mmol) of AgOTf gave 0.729 g (86%) of **2a** as a colorless solid. Mp: 113-115˚C. Anal.

Calcd (found) for $C_{23}H_{34}N_6SO_3F_3Ag$: C, 43.30 (42.99), H, 5.35 (5.36), N 13.14 (12.87). ^{1}H NMR (CD_3CN): δ_H 7.66 (d, *J* = 2.5 Hz, 1 H, H_5pz^{cf}), 7.60 (s, 1 H, $CH_{methine}$), 6.25 (br s, 1 H, H_4pz^{cf}), 6.16 (s, 2 H, H_4pz^{iPr}), 3.30 (sept, *J* = 6.7 Hz, 2 H, $CHMe_2$), 2.86 (sept, *J* = 6.9 Hz, 2 H, $CHMe_2$), 2.39 (br s, 1 H, N-H), 1.24 (d, *J* = 6.9 Hz, 12 H, iPr-CH_3), 1.18 (d, *J* = 6.7 Hz, 12 H, iPr-CH_3). ^{13}C NMR (CD_3CN): δ_C 161.45, 153.81, 105.99, 100.54, 64.01, 29.34, 26.43, 23.81, 23.20, 22.90, 22.78, 22.67. ^{19}F NMR (CD_3CN): -79.34 ppm.

[Ag($^{H}L^{iPr2}$)$_2$](OTf) (2b): A mixture of 0.524 g of (1.37 mmol) of $^{H}L^{ipr}$ and 0.176 g (1.37 mmol) of AgOTf gave 0.559 g (80%) of **2b** as a colorless solid after drying under vacuum for an hour.

Mp: 125-127˚C. ^{1}H NMR (CD_3CN): δ_H 7.63 (s, 1 H, $CH_{methine}$), 7.61 (d, *J* = 1.8 Hz, 1 H, H_5pz^{cf}), 6.14 (s, 2 H, H_4pz^{iPr}), 5.97 (br d, 1 H, H_4pz^{cf}), 5.32 (br s, 2H, N-H), 3.31 (sept, *J* = 6.7 Hz, 2 H, $CHMe_2$), 2.43 (br m, 2 H, $CHMe_2$), 1.23 (m, 12 H, iPr-CH_3), 1.00 (d, *J* = 6.7 Hz, 6 H, iPr-CH_3), 0.99 (d, *J* = 6.7 Hz, 6 H, iPr-CH_3). ^{13}C NMR (CD_3CN): δ_C 161.80, 154.25, 148.41, 131.04, 122.11 (q, J = 324 Hz, CF_3), 105.68 ($C4pz^{cf}$), 100.45 ($C4pz^{iPr}$), 64.95 (C_{meth}), 29.20, 26.52, 25.48, 23.66, 23.60, 23.06, 22.24. ^{19}F NMR (CD_3CN): -79.34 ppm.

C. Catalytic Aziridination.

General Procedure. A 1.00 g sample of activated 4 Å molecular sieves and a Teflon-coated magnetic stir bar were added to a Schlenk flask under an argon blanket. The flask was flame-dried under vacuum, then was backfilled with argon, and allowed to cool to room temperature. Next, under an argon blanket, either the pre-formed metal catalyst

(0.020 mmol) or, for in-situ formed catalysts, 0.020 mmol metal salt precursor and either 0.020 mmol or 0.040 mmol ligand, were added to the flask, followed by 0.171 g (1.00 mmol) of tosylamine, and 0.322 g (1.00 mmol) of $PhI(OAc)_2$. The reaction flask was subjected to three evacuation and argon backfill cycles. Next, 4 mL of dry distilled CH_3CN was added by syringe. The reaction flask was placed in an oil bath maintained at 80˚C and allowed to equilibrate for 15 min. Then, 0.57 mL (0.52 g, 5.0 mmol) of styrene was added by syringe, at which time the solution changed color to orange, or in some instances, orange-brown. After the reaction mixture had been stirred at 80˚C for 16 h, it was filtered through a sintered glass frit. The solid residue was washed with two 2 mL portions of CH_3CN. Next, between 20 and 30 mg (89.9 to 135 μmol) of 1,4-bis(trimethylsilyl)benzene was added to the solvate as a nonvolatile NMR standard, and the solvent was removed by rotary evaporation to leave a brown-orange oily residue. NMR yields of N-tosyl-2-phenylaziridine (conversion %) in the brown-orange oily residue (dissolved in $CDCl_3$) were obtained by relative integrations as follows. First the singlet resonance at δ_H 0.26 ppm for $SiCH_3$ hydrogens was set to 18 H. Next the average integration value for the resonances at δ_H 3.78 (dd, J = 7.2, 4.6 Hz, 1 H) and δ_H 2.98 (d, J = 7.2 Hz, 1 H) for cyclopropane hydrogens was taken (the third doublet resonance is obscured by the tosyl methyl resonance near 2.4 ppm). The average integration value is then multiplied by the known μmol of $C_6H_4(SiMe_3)_2$ and 100% to give the % conversion to aziridine. The average values of three independent runs are collected in Table 3.2.

D. X-ray Crystallography.

X-ray intensity data from a colorless plate of [Ag($^{Ts}L^{iPr}$)(OTf)]·acetone were collected at 100.0(1) K with an Oxford Diffraction Ltd. Supernova equipped with a 135 mm Atlas CCD detector using Cu Kα radiation, λ = 1.54184 Å. Raw data frame integration and Lp corrections were performed with CrysAlis Pro (Oxford Diffraction, Ltd.).[84] Final unit cell parameters were determined by least-squares refinement of 22190 reflections from the data set with $I > 2\sigma(I)$. Analysis of the data showed negligible crystal decay during collection in each case. Direct methods structure solutions were performed with Olex2.solve[85] while difference Fourier calculations and full-matrix least-squares refinements against F2 were performed with SHELXTL.[86] Empirical (Gaussian) absorption corrections were applied using spherical harmonics implemented in the SCALE3 ABSPACK scaling algorithm. Hydrogen atoms were placed in idealized positions and included as riding atoms. One of the iso-propyl groups is unevenly (63:37 %) disordered over two nearby positions, affecting C14 (C14a) and C16 (C16a). A summary of crystal data and structure refinement is given in Table 3.1.

Table 3.1. Crystal data and structure refinement for [Ag($^{Ts}L^{iPr}$)(OTf)]·acetone, **1**·acetone

Identification code	**1**·acetone
Empirical formula	$C_{33}H_{46}AgF_3N_6O_6S_2$
Formula weight	851.75
Temperature/K	100.15(10)
Crystal system	monoclinic
Space group	$P2_1/n$
a/Å	9.25935(6)
b/Å	14.83472(12)
c/Å	28.0088(3)
α/°	90
β/°	96.2408(8)
γ/°	90
Volume/Å^3	3824.48(6)
Z	4
ρ_{calc}g/cm^3	1.479
μ/mm^{-1}	5.804
F(000)	1760.0
Crystal size/mm^3	0.239 × 0.129 × 0.036
Radiation	CuKα (λ = 1.54184)
2Θ range for data collection/°	8.72 to 141.2
Index ranges	$-11 \leq h \leq 11$, $-18 \leq k \leq 17$, $-30 \leq l \leq 33$
Reflections collected	35576
Independent reflections	7254 [R_{int} = 0.0344, R_{sigma} = 0.0194]
Data/restraints/parameters	7254/0/502
Goodness-of-fit on F^2	1.038
Final R indexes [$I \geq 2\sigma(I)$]	R_1 = 0.0259, wR_2 = 0.0675
Final R indexes [all data]	R_1 = 0.0267, wR_2 = 0.0682
Largest diff. peak/hole / e Å^{-3}	0.77/-0.45

3.3. Results and Discussion

The optimized synthetic route to the new bulky 'confused' scorpionate ligands is outlined in Scheme 3.1. The cobalt(II)-catalyzed Peterson rearrangement reaction[115] between N-tosylpyrazole-3-carboxaldehyde and an excess of in-situ formed bis(3,5-diisopropylpyrazolyl)sulfinyl, O=S(pz^{iPr2})$_2$, gave very high yields (> 90 %) of the N-tosyl-protected ligand, $^{Ts}L^{iPr2}$. The use of excess O=S(pz^{iPr2}) ensured reproducibly high yields. The ligand $^{Ts}L^{iPr2}$ could be also be obtained

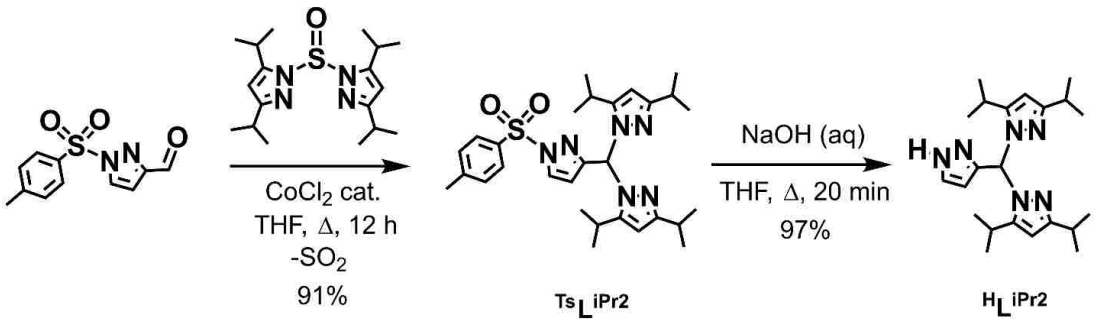

Scheme 3.1. Optimized route to the new C-scorpionate ligands.

in lower yields (ca. 65%) in a multi-pot reaction using O=C(pz^{iPr2})$_2$ in toluene instead of the sulfinyl derivative in THF. As dipyrazolylcarbonyls are generally more reactive than their sulfinyl counterparts,[ref] the lower yield by this latter route was initially surprising. It is noted, however, that the syntheses of O=C(pz^{iPr2})$_2$ from triphosgene and H(pz^{iPr2}) was invariable complicated by a small amount (ca. 5%) of the starting heterocycle that is difficult to separate and likely interferes with the subsequent rearrangement reaction. The N-tosyl group of $^{Ts}L^{iPr2}$ was quickly and quantitatively hydrolyzed under basic conditions to give $^{H}L^{iPr2}$. The ^{1}H NMR spectrum of each ligand reveals a similar low symmetry. Specifically, there is only one resonance near δ_H = 6 ppm for the ring H_4-pz^{iPr}

hydrogen and two septet resonances near δ_H = 3.3 (J = 6.8 Hz) and 2.9 (J = 6.9 Hz) ppm for the $CHMe_2$ groups indicating equivalency of these two pyrazolyl rings, top right of Figure 3.1. However, there are three doublet resonances near δ_H = 1.1, 1.0, 0.9 ppm that integrate to 12, 6, and 6 hydrogens for the isopropyl methyl groups. Moreover, the ^{13}C NMR shows 6 resonances for isopropyl group carbons. The observed number of resonances is unusual, since a C_s-symmetric ligand would be expected to give only two doublet ^{i}Pr-CH_3 ^{1}H resonances and four singlet ^{13}C isopropyl carbon resonances. Alternatively, as illustrated in Figure 3.1, a C_1- symmetric species with free rotation of isopropyl groups and of

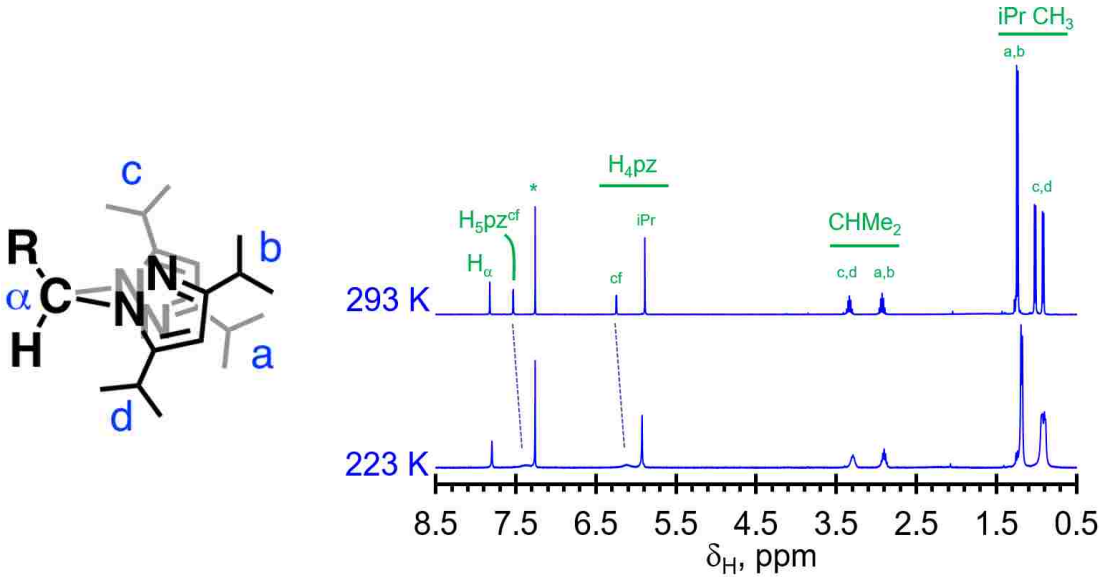

Figure 3.1. Left: Line drawing of a possible C_1-symmetric ligand geometry (R = ^{H}pz or ^{Ts}pz) with methine carbon and different iso-propyl groups labeled. Right: ^{1}H NMR spectra of $^{H}L^{iPr}$ in $CDCl_3$ at 293 K (top) and 223 K (bottom). The asterisk is for solvent resonance, the 'cf' refers to the confused pyrazolyl ring hydrogens.

pyrazolyl rings is expected to give four doublet ^{i}Pr-CH_3 ^{1}H resonances and eight singlet ^{13}C isopropyl carbon resonances (for groups a-d, left of Figure 3.1). Thus, the unusual number of resonances may occur if the local magnetic environment becomes

progressively equivalent (pseudo-C_2 symmetric) with increasing distance from the prochiral methine carbon, α, causing the resonances for isopropyl (and H_4/C_4 pyrazolyl) groups (a and b, Figure 3.1) to have coincidental chemical shifts. An alternate geometry with a C_s-symmetric ligand (with eclipsed diisopropyl pyrazolyl rings) and with 5- (but not the 3-) isopropyl groups locked into one position seems less likely since such an arrangement with overlapping nitrogen lone pairs on adjacent rings is energetically less favorable than a geometry like that in Figure 3.1. Moreover, the unique proton of the proposed 5-iPr CHMeMe' group is expected to appear as a doublet of quartets rather than the observed septet. The low temperature ^{1}H NMR spectrum of the ligands in $CDCl_3$ shows that the free rotation of the confused pyrazolyl slows into the intermediate exchange region near 223 K as the pyrazolyl doublet resonances broaden and shift upfield (bottom right Figure 3.1). Concomitantly, the resonances for the 5-iPr group hydrogens (the septet near 3.3 ppm and the two upfield doublets) broaden and shift upfield compared those in the high temperature spectrum. Unfortunately, the slow exchange limit is not reached before the solvent freezing point. The slow exchange limit was not even observed in the spectrum for CD_2Cl_2 solutions on cooling to 183 K.

Four silver complexes were prepared by direct addition of ligands, Scheme 3.2. Thus, both mono- and di-ligated derivatives could be prepared by controlling silver:ligand stoichiometry. The

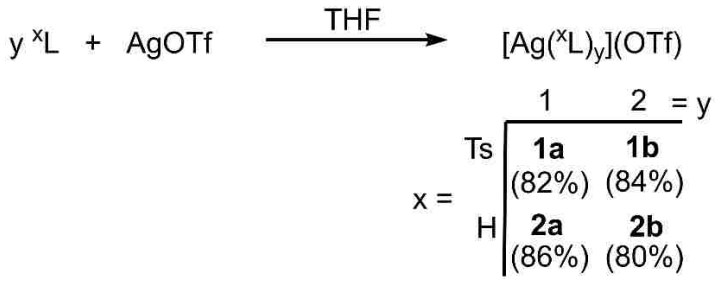

Scheme 3.2. Bulk preparation of silver complexes of the new scorpionate ligands.

yields are generally very good (≥ 80%). It is noted that [Ag($^{Ts}L^{iPr}$)$_2$](OTf), **1b**, has limited solubility in THF and the reaction mixture produces a precipitate, unlike the other derivatives which remain soluble. If the precipitate is collected by filtration and subsequent drying, then only 56% yield of **1b** is obtained because the remainder of the complex remains in the THF soluble portion of the reaction mixture.

Only one of the four new complexes, namely Ag($^{Ts}L^{iPr}$)(OTf)·acetone, **1a**·acetone, gave crystals suitable for single crystal X-ray diffraction. Figure 3.2 shows the asymmetric unit of **1a**·acetone.

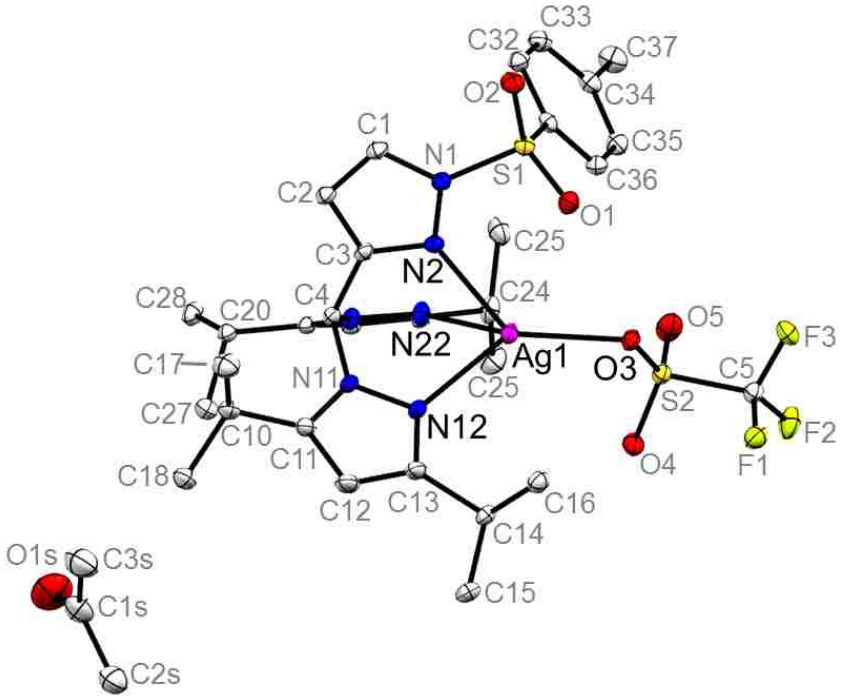

Figure 3.2. Structure of Ag($^{Ts}L^{iPr}$)(OTf)·acetone, **1a**·acetone with atom labelling. Hydrogen atoms and minor disorder components of C14 and C16 are omitted for clarity.

The main structural features of **1a**·acetone are comparable to the related silver complex Ag($^{Ts}L^{*}$)(OTf) reported previously.[20] That is, silver center in **1a**·acetone is

tetracoordinate as a result of bonding to a κ^3*N*- ligand and an oxygen (O3) of the triflate ion. The acetone solvate molecule is not bound to silver, rather it occupies channels parallel with the *a*-axis of the crystal. The Ag1-O3 distance of 2.275(1) Å in **1a**·acetone is longer than the comparable distance of 2.224(2) Å in Ag($^{Ts}L^*$)(OTf). In **1a**·acetone, the diisopropyl pyrazolyls form two shorter Ag-N bonds (Ag1-N12 2.366(2), Ag1-N22 2.335(2) Å; average 2.35(2) Å) than the 'confused' pyrazolyl (Ag1-N2 2.415(2) Å). This asymmetric mode of ligand binding is similar to that in Ag($^{Ts}L^*$)(OTf) where Ag-N_{pz*} averaged 2.34(1) Å and Ag-N2 was 2.427(2) Å. The bond angles about silver in the AgN_3O coordination environment give a τ_δ parameter[20] of 0.63 which puts the coordination polyhedron closer to distorted tetrahedral (τ_δ ~ 0.63 - 0.9) than a distorted saw horse (τ_δ ~ 0.45 – 0.62) as was found for Ag($^{Ts}L^*$)(OTf) (τ_δ = 0.61).

As described extensively in the previous paper regarding silver(I) triflate complexes of other N-confused C-scorpionates, the NMR spectra of [Ag(^xL)$_y$](OTf) (y = 1, 2) complexes in CD_3CN is deceptively simple because each species has a dynamic solution structure and each is also involved multiple dynamic equilibria, including those described by Equations 1-3. Moreover,

$$[Ag(^xL)](OTf) \leftrightarrows Ag(OTf) + {}^xL \quad \text{(Eq. 1)}$$

$$[Ag(^xL)](OTf) + {}^xL \leftrightarrows [Ag(^xL)_2](OTf) \quad \text{(Eq. 2)}$$

$$[Ag(^xL)](OTf) \leftrightarrows \tfrac{1}{2}\,[Ag(^xL)_2](OTf) + \tfrac{1}{2}\,Ag(OTf) \quad \text{(Eq. 3)}$$

the triflate ion in [Ag(^{x}L)](OTf) displaced by CD_3CN but remained in close ion-pair contact with the acidic hydrogens of ligands in the complex. Similar behavior is found for the four new complexes reported here. Thus, the ^{19}F NMR spectrum shows only a single resonance at -79.3 ppm that is identical to that of the free triflate ion in NBu_4OTf

and all metal triflate complexes of other N-confused scorpionate ligands.[20] Secondly, addition of either excess ligand or AgOTf to solutions of the appropriate complexes **1a/b** (or **2a/b**) gave only one set of resonances showing ligand exchange is fast on the NMR timescale. Fast ligand exchange is also evident in NMR titration experiments such as that shown in Figure 3.3 for the addition of AgOTf into solutions of $^{H}L^{iPr}$ (to give either **2a** or **2b**). Next, the NMR spectrum of [Ag($^{H}L^{iPr}$)](OTf), **2a**, shows that all resonances are shifted downfield from those in the free ligand as expected with the exceptions of the methine H_α resonance and the resonances of one of the two sets of isopropyl groups. These exceptional resonances are shifted upfield from those in the free ligand by $|\Delta\delta|$ = 0.10, 0.03 ($CHMe_2$), and 0.005 (iPr CH_3) ppm, respectively. The anomalous upfield shifts are thought to arise from close ion-pair contact with the triflate ion oxygen atoms, since similar behavior has

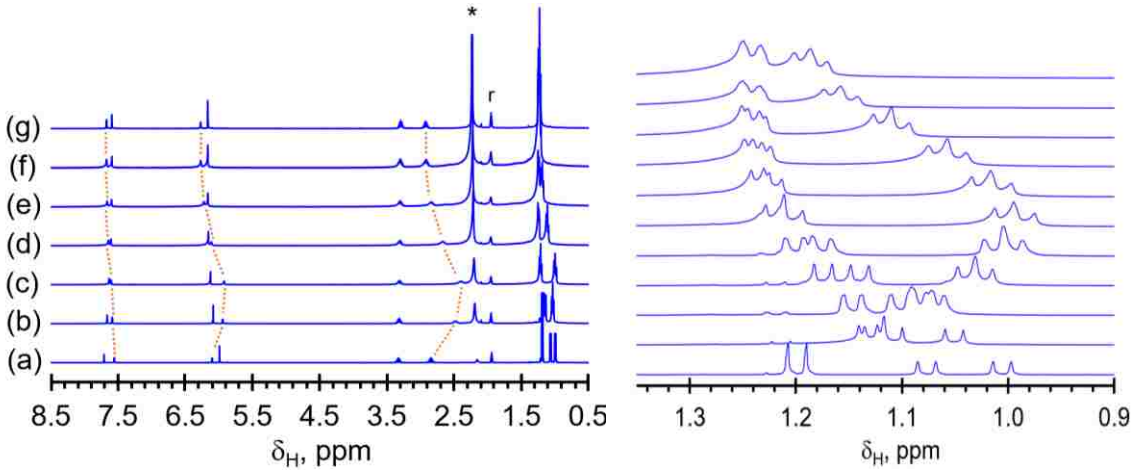

Figure 3.3. Left: Overlay of a portion of the ^{1}H NMR spectra obtained by titration of a concentrated CD_3CN solution of AgOTf into to a CD_3CN solution of $^{H}L^{iPr}$. Molar equivalents of AgOTf added to $^{H}L^{iPr}$: (a) zero; (b) 0.3; (c) 0.5; (d) 0.8; (e) 1.0; (f) 1.5; (g) 2.0. The doublet resonances for the confused pyrazolyl ring hydrogens and one multiplet resonance for a $CHMe_2$ group are tracked with orange dashed lines as a visual guide. The 'r' represents residual CD_2HCN resonance while the asterisk '*' represents residual H_2O in CD_3CN. Right: overlay of iPr-CH_3 region of the NMR spectrum of the free ligand (bottom) and after incremental additions of 0.1 equivalents of AgOTf until a 1:1 L:Ag ratio (top).

been observed in solutions of other metal complexes[20] and because the triflate ion is often found to be in close contact with the methine hydrogen of the ligands in the solid state structures (including that of **1a**·acetone here).[20] The ^{1}H NMR spectrum of **1a** is similar to that of **2a**, but the resonance for H_4 of the confused ring (nearest to the methine H_α) and the resonances for the tolyl ring hydrogens are also shifted upfield with respect to the free ligand; the tolyl CH_3 resonance is unchanged. The ^{1}H NMR spectra of the di-ligated complexes **1b** and **2b** are similar to the mono-ligated cases, but as shown for **2b** in Figures 3.3c and middle spectrum in the right of Figure 3.3, the H_4-pz^{cf} resonance ($|\Delta\delta|$ = 0.19 ppm) and one set of isopropyl resonances exhibits quite large shifts ($CHMe_2$ $|\Delta\delta|$ = 0.45 ppm; iPr-CH_3 $|\Delta\delta|$ = 0.19 ppm) while that for the methine H_α resonance ($|\Delta\delta|$ = 0.19 ppm) exhibits a modest upfield shift ($|\Delta\delta|$ = 0.08 ppm) with respect to the free ligand. These features are qualitatively in agreement with those observed for previous $[Ag(^{x}L^{*})_2](OTf)$ complexes, which were shown to have κ^2*N*- ligands with non-bonded confused pyrazolyl rings in the solid state and possibly interconverting to κ^3*N*- ligands in solution.[20] Given the greater steric profile of diisopropyl pyrazolyls versus dimethylpyrazolyls, it is likely that the current complexes **1b** and **2b** have κ^2*N*- ligands in solution.

Nitrene-Transfer Catalysis.

The ability of **1a**, **1b**, **2a**, **2b**, and related complexes to catalyze the aziridination of styrene by using an in-situ formed N-tosylnitrene (H_2NTs and $PhI(OAc)_2$) in CH_3CN was explored. A summary of results is provided in Table 3.2. Anhydrous silver triflate

(for in situ reactions) or oven-dried samples of preformed complexes were used to ensure both reproducibility and maximum activity. Control experiments showed that activated molecular sieves alone have some activity under these conditions (16h at 80˚C). Aziridination reactions did not occur at room temperature. The current catalysts [**1a-b**, **2a-b**] did not perform better than the previously reported catalysts [Entries 3 and 4]. Among the current Ag catalysts (**1a, 1b, 2a, 2b**), **2a** performed the best followed by **1b** ≈ **1a** and then **2b**. The lower activity of the diisopropyl derivatives could be because of increased ligand electronics which is causing the $[AgL]^+$ and the $[AgL_2]^+$ to adopt a six coordinate (presumably catalytically inactive) silver center in solution. Insitu reactions of copper salts ($Cu(OTf)_2$ and $[Cu(CH_3CN)_4](PF_6)$) with 1 or 2 equivalents of $^{Ts}L^*$ and $^{Ts}L^{ipr}$ were also carried out to catalyze the aziridination of styrene. In the case of $[Cu(CH_3CN)_4](PF_6)$, the addition of the ligand $^{Ts}L^*$ and $^{Ts}L^{ipr}$ did not help the rate of aziridination reaction. But in the case of $Cu(OTf)_2$, addition of $^{Ts}L^{ipr}$ increased the rate of aziridination

Table 3.2. Results of nitrene transfer reactions.[a]

Entry	Catalyst	% yeld
1	None	3(2)
2	Ag(OTf)	3(2)
3	$[Ag(^{Ts}L^*)](OTf)$[20]	17(6)
4	$[Ag(^{Ts}L^*)_2](OTf)$[20]	34(4), 27(3)[b]
5	$[Ag(^{Ts}L^{iPr})](OTf)$, **1a**	12(3), 12(2)[b]
6	$[Ag(^{Ts}L^{iPr})_2](OTf)$, **1b**	13(2), 9(2)[b]
7	$[Ag(^{H}L^{iPr})](OTf)$, **2a**	15(2)
8	$[Ag(^{H}L^{iPr})_2](OTf)$, **2b**	6(2)
9	$[Cu(CH_3CN)_4](PF_6)$	40(5)
10	$Cu(OTf)_2$	44(2)
11	$[Cu(^{Ts}L^*)](PF_6)$	65(4)[b]
12	$[Cu(^{Ts}L^*)_2](PF_6)$	59(3)[b]

13	[Cu(^{Ts}L^{iPr})](PF$_6$)	50(3)[b]
14	[Cu(^{Ts}L^{iPr})](OTf)	49(3)[b]
15	[Cu(^{Ts}L^{iPr})$_2$](PF$_6$)	50(2)[b]

a. conditions: : 5 mmol of styrene, 1 mmol of PhI(OAc)$_2$, 1 mmol of H_2NTs, 0.02 mmol of [Ag], 1 g of 4 Å molecular sieves, 4 mL of CH_3CN, 16 h, 80˚C. b. catalyst formed in-situ.

3.4 Conclusions.

Two new N-confused C-scorpionate ligands , ^{Ts}L^{ipr} and ^{H}L^{ipr}, each with two 'normal' 3,5-diisopropylpyrazolyl groups, and either an N-tosyl or N-H group on the 'confused' pz have been synthesized. The four new Ag complexes with 1:1 and 2:1 L/Ag ratios were spectroscopically characterized. It was possible to structurally characterize only one of the four new complexes. In the solid state, the Ag center of Ag(^{Ts}L^{ipr})(OTf).acetone is four coordinate as a result of bonding to a κ^3*N*- ligand and an oxygen (O3) of the triflate ion. . The ^{1}H NMR spectra of [Ag(^{x}L)$_y$](OTf) (y =1,2) complexes shows a dynamic solution structure and are involved in multiple rapid equilibria. In NMR titrations of the addition of AgOTf into solutions of ^{H}L^{iPr}, fast ligand exchange is also evident. The four new silver(I) C-scorpionates were used as nitrene-transfer catalysts in the aziridination of styrene. The previously reported Ag(I) scorpionates of dimethyl pyrazolyls [Ag(^{x}L*)$_y$(OTf)](y=1,2) showed higher activity in aziridination compared to the pyrazolyl derivatives[Ag(^{x}L)$_y$(OTf)](y=1,2). It was anticipated that if by further increasing the steric bulk on the pyrazolyls these current catalysts can be made more competitive with the AgTp^x or other silver catalysts for aziridination reactions. However, these diisopropyl pyrazolyl silver(I) complexes did not prove to be better catalysts than the previously reported [Ag(^{x}L*)$_y$(OTf)](y=1,2) ones.

CHAPTER 4: FUTURE WORK

Our group has recently synthesized new N-confused C-scorpionate ligands with two 'normal' pz* groups (=3,5-dimethylpyrazol-1-yl) and a 'confused' pyrazolyl with either an N-H, ^{H}L*, or an N-Tosyl (Tosyl = p-toluenesulfonyl), TsL*, bound to a central methine carbon. These bulky ligands complement those previously described, ^{H}L and ^{Ts}L, that had less-bulky, unsubstituted, 'normal' pyrazol-1-yls. For these four related N-confused scorpionate ligands, the 2:1 and 1:1 ligand:silver complexes were prepared and characterized both structurally and spectroscopically. However, these silver complexes show lower activity for catalytic aziridination compared to the previously reported AgTp^{x} complexes. The purpose of this thesis work is to fully investigate if by further increasing the steric bulk on the pyrazolyls these current catalysts can be made more competitive with other previously reported catalysts for intermolecular aziridination reactions. In this contribution, silver complexes of two new N-confused C-scorpionates, ^{Ts}L^{ipr} and ^{H}L^{ipr}, each with two 'normal' 3,5-diisopropylpyrazolyl groups, and either an N-tosyl or N-H group on the 'confused' pz has been prepared and its catalytic ability compared. However, the silver catalysts of the bulkier diisopropylpyrazolyl derivatives did not perform better than the dimethylpyrazolyl derivatives. Future experimental and theoretical work will be done towards determining the mechanism of nitrene transfer catalysis and whether further alteration of ligand sterics and electronics can give more competitive catalysts for aziridination reactions.

Since the bis complexes of the dimethylpyrazolyl ligand derivatives performed better, future work would be to synthesize an anionic tetradentate ligand. By incorporating a pycolyl appendage to two N-confused C-scorpionates will give us a new

tetradentate N_4 ligand. Then the silver complexes of this ligand could be prepared and characterized both structurally and spectroscopically and its catalytic ability toward nitrene transfer could be investigated.

BIBLIOGRAPHY

1. Belloli, R. Nitrenes. *J. Chem. Educ*. **1971**, *48* (7), 422.

2. Eguchi, A.; Shimbayashi, T.; Okamoto, K.; Sasakura, K.; Ohe, K. Recent Progress on Cyclic Nitrenoid Precursors in Transition-Metal-Catalyzed Nitrene-Transfer Reactions. *Chem. – A Eur. J.* **2018**, 1–26.

3. Halfren, J.A. Curr.Org.Chem.2005,9,657-669.

4. B. P. Gómez-Emeterio, J. Urbano, M. M. Díaz-Requejo, P. J. Pérez. *Organomet.* **2008**, *27*, 4126-4130.

5. Au, S. M.; Huang, J. S.; Yu, W. Y.; Fung, W. H.; Che, C. M. *J. Am. Chem. Soc.* **1999,** *121*, 9120-9132.

6. D. S. Breslow, M. F. Sloan, *Tet. Lett.* **1968**, *51*, 5549-5352.

7. R. Breslow, S. H. Gellman, *J. Chem. Soc., Chem. Commun.* **1982**, 1400-1401.

8. Cui, C. He. *J. Am. Chem. Soc.* **2003,** *125*, 16202-16203.

9. Guthikonda,K.; Du Bois, J. *J. Am. Chem. Soc.* **2002**, *124* ,13672-13673.

10. Liang, J. L.; Yuan, S. X.; Chan, P. W. H.; Che, C. M. *Org. Lett.* **2002,** *4*, 4507-4510.

11. Ma, L.; Du, D.; Xu, J. Asymmetric Aziridination of 1 , 3-Dienes Catalyzed by Bisoxazoline-Copper Complexes. Chirality **2006**, *580*, 575–580.

12. Fantauzzi, S.; Gallo, E.; Caselli, A.; Piangiolino, C.; Ragaini, F.; Cenini, S. The (Porphyrin) Ruthenium-Catalyzed Aziridination of Olefins Using Aryl Azides as Nitrogen Sources, *J. Org. Chem.* **2007**, 6053–6059.

13. J. Llaveria, A. Beltrán. M. M. Díaz-Requejo, M. I. Matheu, S. Castillón, P. J. Pérez. *Angew. Chem. Int. Ed*. **2010**, *49*, 7092-7095.

14. L. Maestre, W. M. C. Sameera, M. Díaz-Requejo, F. Maseras, P. J. Pérez. *J. Am. Chem. Soc.* **2013**, *135*, 1338-1348.

15. Y. Cui, C. He. *Angew. Chem. Int. Ed.* **2004**, 43, 4210-4212.

16. Z. Li, D. A. Capretto, R. Rahaman, C. He. *Angew. Chem. Int. Ed.* **2007***, 46*, 5184-5186.

17. J. W. Rigoli, C. D. Weatherly, J. M. Alderson, B. T. Vo, J. M. Schomaker. *J. Am. Chem Soc.* **2013**, *135*, 17238- 17241.

18. Cingolani, A.; Effendy; Martini, D.; Pellei, M.; Pettinari, C.; Skelton, B. W.; White, A. H. Silver Derivatives of Tris(pyrazol-1- yl)methanes. A silver(I) nitrate complex containing tris(pyrazolyl)- methane coordinated in a bridging mode. *Inorg. Chim. Acta* **2002,** *328,* 87−95.

19. Smolenski, P.; Pettinari, C.; Marchetti, F.; Guedes da Silva, M. F. C.; Lupidi, G.; Badillo Patzmay, G. V.; Petrelli, D.; Vitali, L. A.; Pombeiro, A. J. L. Syntheses, structures, and antimicrobial activity of new remarkably light-stable and water-soluble tris(pyrazolyl) methanesulfonate silver(I) derivatives of N-methyl-1, 3, 5-triaza-7- phosphaadamantane salt - [mPTA] BF_4. *Inorg. Chem.* **2015**, *54*, 434−440. (b) Pettinari, C.; Marchetti, F.; Lupidi, G.; Quassinti, L.; Bramucci, M.; Petrelli, D.; Vitali, L. A.; Guedes da Silva, M. F. C.; Martins, L. M. D. R. S.; Smolenski, P.; Pombeiro, A. J. L. Synthesis, Antimicrobial and Antiproliferative Activity of Novel Silver(I) Tris(pyrazolyl)methanesulfonate and 1, 3, 5-Triaza-7-phosphadamantane Complexes. *Inorg. Chem.* **2011**, *50,* 11173−11183.

20. Gardinier, J. R.; Meise, K. J.; Jahan, F.; Lindeman, S. V., Reaction Chemistry of Silver(I) Trifluoromethanesulfonate Complexes of Nitrogen-Confused C-Scorpionates. *Inorg Chem* **2018,** *57* (3), 1572-1589.

21. Halcrow, M. A. *Spin Crossover Materials, Properties and Applications*; John Wiley & Sons, Ltd, 2013.

22. Gutlich, P.; Goodwin, H. A. *Spin Crossover in Transition Metal Compounds I-III. Topics in Current Chemistry;* Springer-Verlag: Berlin, Germany, 2004; Vol 233-235.

23. Gütlich, P.; Hauser, A.; Spiering, H. "Thermal and Optical Switching of Iron(II) Complexes" *Angew. Chem., Int. Ed. Engl.* **1994**, *33*, 2024–2054.

24. Gütlich, P.; Garcia, Y.; Goodwin, H. A.; "Spin crossover phenomena in Fe(II) complexes" *Chem. Soc. Rev.* **2000**, *29*, 419-427.

25. Gütlich, P. "Spin transition in iron(II) complexes induced by heat, pressure, light, and nuclear decay" *Hyperfine Interactions **1987***, 33, 105-132.

26. Levchenko, G. G.; Khristov, A. V.; Varyukhin, V. N. "Spin crossover in iron(II)-containing complex compounds under a pressure" *Low Temp. Phys.* **2014**, *40*, 571-585.

27. Drickamer, H. G. "Electronic transfer reactions in transition metal compounds at high pressure" *Angew. Chem.* **1974**, *13*, 39-47.

28. Lenz, F. "Physical and chemical induced spin crossover" *J. Phys.: Conf. Ser.* **2010**, *217*, 012022.

29. Nègre, N.; Conséjo, C.; Goiran, M.; Bousseksou, A.; Varret, F.; Tuchagues, J. P.; Barbaste, R.; Askénazy, S.; Haasnoot, J. G. "Spin transitions in a series of FeII molecular complexes induced by a strong-pulsed magnetic field" *Physica B* **2001**, *91*, 294–295.

30. Unruh, D.; Homenya, P.; Kumar, M.; Sindelar, R.; Garcia, Y.; Renz, F. "Spin state switching of metal complexes by visible light or hard X-rays" *Dalton Trans.* **2016**, *45*, 14008-14018.

31. Létard, J.-F. "Photomagnetism of iron(II) spin crossover complexes—the T(LIESST) approach" *J. Mater. Chem.* **2006**, *16*, 2550-2559.

32. Lefter, C.; Tan, R.; Dugay, J.; Tricard, S.; Molnár, G.; Salmon, L.; Carrey, J.; Nicolazzi, W.; Rotaru, A.; Bousseksou, A. "Unidirectional electric field-induced spin-state switching in spin crossover based microelectronic devices" *Chem. Phys. Lett.* **2016**, *644*, 138-141.

33. Kumar, K. S.; Ruben, M. "Emerging trends in spin crossover (SCO) based functional materials and devices" *Coord. Chem. Rev.* **2017**, *346*, 176-205.

34. Lefter, C.; Davesne, V.; Salmon, L.; Molnar, G.; Demont, P.; Rotaru, A.; Bousseksou, A. "Charge transport and electrical properties of spin crossover materials: towards nanoelectronic and spintronic devices" *Magnetochemistry* **2016**, 2, 1-19.

35. Holovchenko, A.; Dugay, J.; Gimenez-Marques, M.; Torres-Cavanillas, R.; Coronado, E.; van der Zant, H. S. J. "Near room-temperature memory devices based on hybrid spin crossover@SiO_2 nanoparticles coupled to single-layer graphene nanoelectrodes" *Adv. Mater.* **2016**, *28*, 7228-7233.

36. Manrique-Juarez, M. D.; Mathieu, F.; Shalabaeva, V.; Cacheux, J.; Rat, S.; Nicu, L.; Leichle, T.; Salmon, L.; Molnar, G.; Bousseksou, A. "A Bistable Microelectromechanical System Actuated by Spin crossover Molecules" *Angew. Chem., Int. Ed.* **2017**, *56*, 8074-8078.

37. von Ranke, P. J. "A microscopic refrigeration process triggered through spin crossover mechanism" *Appl. Phys. Lett.* **2017**, *110*, 181909/1-181909/4.

38. Kucheriv, O. I.; Oliynyk, V. V.; Zagorodnii, V. V.; Launets, V. L.; Gural'skiy, I. A. "Spin crossover Materials towards Microwave Radiation Switches" *Scientific Reports* **2016**, *6*, 38334

39. Thorarinsdottir, A. E.; Gaudette, A. I.; Harris. T. D. "Spin crossover and high-spin iron(ii) complexes as chemical shift ^{19}F magnetic resonance thermometers" *Chem Sci.* **2017**, *8*, 2448–2456.

40. Jeon, I.-R.; Park, J. G.; Haney, C. R.; Harris, T. D. "Spin crossover iron(II) complexes as PARACEST MRI thermometers" *Chem. Sci.* **2014**, *5*, 2461-2465.

41. Brooker, S. "Spin crossover with thermal hysteresis: practicalities and lessons learnt" *Chem. Soc. Rev.* **2015**, *44*, 2880-2892.

42. Polymorphs: (a) Shatruk, M.; Phan, H.; Chrisostomo, B. A.; Suleimenova, A. "Symmetry-Breaking Structural Phase Transitions in Spin crossover Complexes" *Coord. Chem. Rev.*

2015, *289-290*, 62-73. (b) Tao, J; Wei, R. –J.; Huang, R.-B.; Zheng, L.-S. "Polymorphism in Spin crossover Systems" *Chem. Soc. Rev.* **2012**, *41*, 703-737.

43. (a) Vela, S.; Paulsen, H. "Deciphering Crystal Packing Effects in the Spin Crossover of six $[Fe(2\text{-pic})_3]Cl_2$ Solvatomorphs" *Dalton Trans.* **2019**, 48, 1237-1245. (b) Bartual-Murgui, C.; Codina, C.; Roubeau, O.; Aromí, G. "A Sequential Method to Prepare Polymorphs and Solvatomorphs of $[Fe(1,3\text{-bpp})_2](ClO_4)_2 \cdot nH_2O$ (n=0, 1, 2) with Varying Spin-Crossover Behaviour" *Chem. Eur. J.* **2016**, *22*, 12767-12777.

44. (a) Berdiell, I. C.; Kulmaczewski, R.; Cespedes, O.; Halcrow, M. A. "An Incomplete Spin Transition Associated with a Z' =1 to Z'=24 Crystallographic Symmetry Breaking" *Chem. Eur. J.* **2018**, 24, 5055-5059. (b) Craig, G. A.; Roubeau, O.; Aromi, G. "Spin state switching in 2,6-bis(pyrazol-3-yl)pyridine (3-bpp) based Fe(II) complexes" *Coord. Chem. Rev.* **2014**, *269*, 13-31.

45. Roubeau, O. "Triazole-Based One-Dimensional Spin crossover Coordination Polymers" *Chem. Eur. J.* **2012**, *18*, 15230-15244.

46. Olguin, J.; Brooker, S. "Spin crossover active iron(II) complexes of selected pyrazole-pyridine/pyrazine ligands" *Coord. Chem. Rev.* **2011**, *255*, 203-240.

47. Munoz, M. C.; Real, J. A. "Thermo-, piezo-, photo- and chemo-switchable spin crossover iron(II)-metallocyanate based coordination polymers" *Coord. Chem. Rev.* **2011**, *255*, 2068-2093.

48. Goodwin, H. A. "Spin crossover in iron(II) tris(diimine) and bis(terimine) systems" *Top. Curr. Chem.* **2004**, *233*, 59-90.

49. Phan, H.; Hrudka, J. J.; Igimbayeva, D.; Lawson D., Latevi M.; Shatruk, M. "A Simple Approach for Predicting the Spin State of Homoleptic Fe(II) Tris-diimine Complexes" *J. Am. Chem. Soc.* **2017**, *139*, 6437-6447.

50. Trofimenko, S. Scorpionates: The Coordination Chemistry of Polypyrazolylborate Ligands, Imperial Press, London, 1999.

51. Pettinari, C. Scorpionates II: Chelating Borate Ligands, Imperial Press, London, 2008.

52. Long, G. J.; Grandjean, F.; Reger, D. L. "Spin Crossover in Pyrazolylborate and Pyrazolylmethane Complexes" *Top. Curr. Chem.* **2004**, *233*, 91-122.

53. Lavrenova, L. G.; Shakirova, O. G. "Spin Crossover and Thermochromism of Iron(II) Coordination Compounds with 1,2,4-Triazoles and Tris(pyrazol-1-yl)methanes" *Eur. J. Inorg. Chem.* **2013**, *2013*, 670-682.

54. Real, J. A.; Muñoz, M. C.; Faus, J.; Solans, X. "Spin Crossover in Novel Dihydrobis(1-pyrazolyl)borate $[H_2B(pz)_2]$-Containing Iron(II) Complexes. Synthesis, X-ray Structure,

and Magnetic Properties of [FeL{$H_2B(pz)_2$}$_2$] (L = 1,10-Phenanthroline and 2,2'-Bipyridine)" *Inorg. Chem.* **1997**, *36*, 3008–3013.

55. (a) Moliner, N.; Salmon, L.; Capes, L.; Muñoz, M. C.; Létard, J.-F.; Bousseksou, A.; Tuchagues, J.-P.; McGarvey, J. J.; Dennis, A. C.; Castro, M.; Burriel, R.; Real, J. A. "Thermal and Optical Switching of Molecular Spin States in the {[FeL[$H_2B(pz)_2$]$_2$} Spin crossover System (L = bpy, phen)" *J. Phys. Chem. B* **2002** *106*, 4276-4283. (b) Galet, A.; Gaspar, A. B.; Agusti, G.; Muñoz, M. C.; Levchenko, G.; Real, J. A. "Pressure Effect Investigations on the Spin Crossover Systems{Fe[$H_2B(pz)_2$]$_2$(bipy)} and {Fe[$H_2B(pz)_2$]$_2$(phen)}" *Eur. J. Inorg. Chem.* **2006**, *2006*, 3571-3573.

56. Xue, S.; Guo, Y.; Rotaru, A.; Müller-Bunz, H.; Morgan, G. G.; Trzop, E.; Collet, E.; Oláh, J.; Garcia, Y. "Spin Crossover Behavior in a Homologous Series of Iron(II) Complexes based on Functionalized Bipyridyl Ligands" *Inorg. Chem.* **2018**, *57*, 9880-9891.

57. Moertel, M.; Witt, A.; Heinemann, F. W.; Bochmann, S.; Bachmann, J.; Khusniyarov, M. M. "Synthesis, Characterization, and Properties of Iron(II) Spin- Crossover Molecular Photoswitches Functioning at Room Temperature" *Inorg. Chem.* **2017**, *56*, 13174-13186.

58. Ru, J.; Yu, F.; Shi, P.-P.; Jiao, C.-Q.; Li, C.-H.; Xiong, R.-G.; Liu, T.; Kurmoo, M.; Zuo, Jing-L. "Three Properties in One Coordination Complex: Chirality, Spin Crossover, and Dielectric Switching" *Eur. J. Inorg. Chem.* **2017**, *2017*, 3144-3149.

59. Luo, Y.-H.; Nihei, M.; Wen, G.-J.; Sun, B.-W.; Oshio, H. "Ambient-Temperature Spin-State Switching Achieved by Protonation of the Amino Group in [Fe(H_2Bpz_2)$_2$(bipy-NH_2)]" *Inorg. Chem.* **2016**, *55*, 8147-8152.

60. Mahfoud, T.; Molnár, G.; Cobo, S.; Salmon, L.; Thibault, C.; Vieu, C.; Demont, P.; Bousseksou, A. "Electrical properties and non-volatile memory effect of the [Fe($HB(pz)_3$)$_2$] spin crossover complex integrated in a microelectrode device" *Appl. Phys. Lett.* **2011**, *99*, 053307.

61. Davesne, V.; Gruber, M.; Studniarek, M.; Doh, W. H.; Zafeiratos, S.; Joly, L.; Sirotti, F.; Silly, M. G.; Gaspar, A. B.; Real, J. A.; Schmerber, G.; Bowen, M.; Weber, W.; Boukari, S.; Da Costa, V.; Arabski, J.; Wulfhekel, W.; Beaurepaire, E. "Hysteresis and change of transition temperature in thin films of Fe{[Me_2Pyrz]$_3$BH}$_2$, a new sublimable spin crossover molecule" *J. Chem. Phys.* **2015**, *142*, 194702/1-194702/8 .

62. Iasco, O.; Boillot, M.-L.; Bellec, A.; Guillot, R.; Rivière, E.; Mazerat, S.; Nowak, S.; Morineau, D.; Brosseau, A.; Miserque, F.; Repain, V.; Mallah, T. "The disentangling of hysteretic spin transition, polymorphism and metastability in bistable thin films formed by sublimation of bis(scorpionate) Fe(II) molecules" *J. Mater. Chem. C*, **2017**, 5, 11067-11075.

63. Ossinger, S.; Naggert, H.; Kipgen, L.; Jasper-Toennies, T.; Rai, A.; Rudnik, J.; Nickel, F.; Arruda, L. M.; Bernien, M.; Kuch, W.; Berndt, R.; Tuczek, F. "Vacuum-Evaporable Spin crossover Complexes in Direct Contact with a Solid Surface: Bismuth versus Gold" *J. Phys. Chem. C* **2017**, *121*, 1210-1219.

64. Beniwal, S.; Zhang, X.; Mu, S.; Naim, A.; Rosa, P.; Chastanet, G.; Letard, J.-F.; Liu, J.; Sterbinsky, G. E.; Arena, D. A.; Dowben, P. A.; Enders, A. "Surface-induced spin state locking of the [Fe(H_2B(pz)$_2$)$_2$(bipy)] spin crossover complex" *J. Phys.* **2016**, *28*, 206002/1-206002/8

65. Naggert, H.; Rudnik, J.; Kipgen, L.; Bernien, M.; Nickel, F.; Arruda, L. M.; Kuch, W.; Naether, C.; Tuczek, F. "Vacuum-evaporable spin crossover complexes: physicochemical properties in the crystalline bulk and in thin films deposited from the gas phase" *J. Mater. Chem. C* **2015**, *3*, 7870-7877.

66. Bernien, M.; Naggert, H.; Arruda, L. M.; Kipgen, L.; Nickel, F.; Miguel, J.; Hermanns, C. F.; Krüger, A.; Krüger, D.; Schierle, E.; Weschke, E.; Tuczek, F.; Kuch, W. "Highly Efficient Thermal and Light-Induced Spin-State Switching of an Fe(II) Complex in Direct Contact with a Solid Surface" *ACS Nano* **2015**, *9*, 8960–8966.

67. Milek, M.; Heinemann, F. W.; Khusniyarov, M. M. "Spin Crossover Meets Diarylethenes: Efficient Photoswitching of Magnetic Properties in Solution at Room Temperature" *Inorg. Chem.* **2013**, *52*, 11585-11592.

68. Goodman, M. A.; Nazarenko, A. Y.; Casavant, B. J.; Li, Z.; Brennessel, W. W.; DeMarco, M. J.; Long, G.; Goodman, M. S. "Tris(5-methylpyrazolyl)methane: Synthesis and Properties of Its Iron(II) Complex" *Inorg. Chem.* **2012**, *51*, 1084-1093.

69. Goodman, M. A.; DeMarco, M. J.; Tarasek, S. E.; Nazarenko, A. Y.; Brennessel, W.; Goodman, M. S. "Iron complexes of tris(pyrazolyl)ethane ligands methylated in the 3-, 4-, and 5-positions" *Inorg. Chim. Acta* **2014**, *423*, 358–368.

70. Sohrin, Y.; Kokusen, H.; Matsui, M. "Control of Ligand Field Strength through Intra- and Interligand Contact. Octahedral Iron(II) Poly(pyrazolyl)borate Complexes" *Inorg. Chem.* **1995**, *34*, 3928-3934.

71. Hamon, P.; Thépot, J.-Y.; Le Floch, M.; Boulon, M.-E.; Cador, O.; Golhen, S.; Ouahab, L.; Fadel, L.; Saillard, J.-Y.; Hamon, J.-R. "Dramatic Remote Substituent Effects on the Electronic Spin State of Bis(scorpionate) Iron(II) Complexes" *Angew. Chem. Int. Ed.* **2008**, *47*, 8687 –8691.

72. Reger, D. L.; Gardinier, J. R.; Elgin, J. D.; Smith, M. D.; Hautot, D.; Long, G. J.; Grandjean, F. "Structure−Function Correlations in Iron(II) Tris(pyrazolyl)borate Spin-State Crossover Complexes" *Inorg. Chem*. **2006**, *45*, 8862-8875.

73. Gardinier, J. R.; Meise, K. J.; Jahan, F.; Lindeman, S. V. "Reaction Chemistry of Silver(I) Trifluoromethanesulfonate Complexes of Nitrogen-Confused C-Scorpionates" *Inorg. Chem.* **2018**, *57*, 1572-1589.

74. Gardinier, J. R.; Treleven, A. R.; Meise, K. J.; Lindeman, S. V. "Accessing Spin crossover Behaviour in Iron(II) complexes of N-Confused Scorpionate Ligands" *Dalton Trans.* **2016**, *45*, 12639-12643.

75. (a) Reger, D. L.; Little, C. A.; Rheingold, A. L.; Lam, M.; Concolino, T.; Mohan A.; Long, G. J. "Structural, Electronic, and Magnetic Properties of $\{Fe[HC(3,5\text{-}Me_2pz)_3]_2\}(BF_4)_2$ (pz = Pyrazolyl): Observation of Unusual Spin crossover Behavior" *Inorg. Chem.* **2000**, *39*, 4674-4675. (b)Reger, D. L.; Little, C. A.; Young Jr. V. G.; Pink, M. "Variable-Temperature X-ray Structural Investigation of $\{Fe[HC(3,5\text{-}Me_2pz)_3]_2\}(BF_4)_2$ (pz = Pyrazolyl Ring): Observation of a Thermally Induced Spin State Change from All High Spin to an Equal High Spin-Low Spin Mixture, Concomitant with the Onset of Nonmerohedral Twinning" *Inorg. Chem.* **2001**, 40, 2870-2874. (c) Reger, D. L.; Little, C. A.; Smith, M. D.; Long, G. J. "Solid-State Structural and Magnetic Investigations of $\{M[HC(3,5\text{-}Me_2pz)_3]_2\}(BF_4)_2$ (M = Fe, Co, Ni, Cu): Observation of a Thermally Induced Solid-State Phase Change Controlling an Iron(II) Spin-State Crossover" *Inorg. Chem.* **2002**, *41*, 4453-4460.

76. Reger, D. L.; Little, C. A.; Rheingold, A. L.; Lam, M.; Liable-Sands, L. M.; Rhagitan, B.; Concolino, T.; Mohan, A.; Long, G. J.; Briois, V.; Grandjean, F. "A Synthetic, Structural, Magnetic, and Spectral Study of Several $\{Fe[tris(pyrazolyl)methane]_2\}(BF_4)_2$ Complexes: Observation of an Unusual Spin-State Crossover" *Inorg. Chem.* **2001**, *40*, 1508-1520; Briois, V.; Sainctavit, P.; Long, G. J.; Grandjean, F. "Importance of Photoelectron Multiple Scattering in the Iron K-Edge X-ray Absorption Spectra of Spin crossover Complexes: Full Multiple Scattering Calculations for Several Iron(II) Trispyrazolylborate and Trispyrazolylmethane Complexes" *Inorg. Chem.* **2001**, *40*, 912-918.

77. Reger, D. L.; Elgin, J. D.; Foley, E. A.; Smith, M. D.; Grandjean, F.; Long, G. J. "Structural, Magnetic, and Mössbauer Spectral Study of the Electronic Spin-State Transition in $[Fe\{HC(3\text{-}Mepz)_2(5\text{-}Mepz)\}_2](BF_4)_2$" *Inorg. Chem.* **2009**, *48*, 9393-9401.

78. Moubaraki, B.; Leita, B. A.; Halder, G. J.; Batten, S. R.; Jensen, P.; Smith, J. P.; Cashion, J. D.; Kepert, C. J.; Létard, J.-F.; Murray, K. S. "Structure, magnetism and photomagnetism of mixed-ligand tris(pyrazolyl)methane iron(II) spin crossover compounds" *Dalton Trans.* **2007**, 4413–4426.

79. (a) Moertel, M.; Witt, A.; Heinemann, F. W.; Bochmann, S.; Bachmann, J.; Khusniyarov, M. M. "Synthesis, Characterization, and Properties of Iron(II) Spin crossover Molecular Photoswitches Functioning at Room Temperature." *Inorg. Chem.* **2017**, *56*, 13174−13186. (b) Rösner, B.; Milek, M.; Witt, A.; Gobaut, B.; Torelli, P.; Fink, R. H.; Khusniyarov, M. M. "Reversible Photo-switching of a Spin crossover Molecular Complex in the Solid State at Room Temperature." *Angew. Chem., Int. Ed.* **2015**, *54*, 12976−12980.

80. Fulmer, G. R.; Miller, A. J. M.; Sherden, N. H.; Gottleib, H. E.; Nudelman, A.; Stoltz, B. M.; Bercaw, J. E.; Goldberg, K. I. "NMR Chemical Shifts of Trace Impurities: Common Laboratory Solvents, Organics, and Gases in Deuterated Solvents Relevant to the Organometallic Chemist" *Organometallics* **2010**, *29*, 2176-2179.

81(a) Evans, D. F. "The determination of the paramagnetic susceptibility of substances in solution by nuclear magnetic resonance" *J. Chem. Soc.* **1959**, 2003–2005; (b) Evans, D.

F.; Fazakerley, G. V.; Phillips, R. F. “Organometallic compounds of bivalent europium, ytterbium, and samarium” *J. Chem. Soc. A* **1971**, 1931–1934. (c) Piguet, C. “Paramagnetic Susceptibility by NMR: The "Solvent Correction" Removed for Large Paramagnetic Molecules” *J. Chem. Ed.* **1997**, *74*, 815-816.

82. Morrison, G.; zur Loye, H.-C. “Simple correction for the sample shape and radial offset effects on SQUID magnetometers: Magnetic measurements on Ln_2O_3 (*Ln*=Gd, Dy, Er) standards” *J. Solid State Chem.* **2015**, 221, 334–337.

83. Bain, G. A.; Berry, J. F. “Diamagnetic Corrections and Pascal's Constants” *J. Chem. Ed.* **2008**, *85*, 532-536.

84. CrysAlisPro, Agilent Technologies, Version 1.171.34.46 (release 25-11-2010 CrysAlis171 .NET), (compiled Nov 25 2010,17:55:46).

85. O. V. Dolomanov, L. J. Bourhis, R. J. Gildea, J. A. K. Howard and H. Puschmann. "OLEX2: a complete structure solution, refinement and analysis program". *J. Appl. Cryst.* **2009**, *42*, 339-341.

86. Sheldrick, G. M. SHELXTL Version 6.12; Bruker Analytical X-ray Systems, Inc., Madison Wisconsin, USA, 2001.

87. (a) Swart, M.; Groenhof, A. R.; Ehlers, A. W.; Lammertsma, K. “Validation of Exchange-Correlation Functionals for Spin States of Iron Complexes” *J. Phys. Chem. A* **2004**, *108*, 5479-5483. (b) Swart, M.; Ehlers, A. W.; Lammertsma, K. “Performance of the OPBE exchange-correlation functional” *Molec. Phys.* **2004**, *102*, 2467-2474.

88. Weigend, F. and Ahlrichs, R. “Balanced basis sets of split valence, triple zeta valence and quadruple zeta valence quality for H to Rn: Design and assessment of accuracy” *Phys. Chem. Chem. Phys.*, **2005**, *7*, 3297-3305.

89. (a) Liddle, B. J.; Wanniarachchi, S.; Hewage, J. S.; Lindeman, S. V.; Bennett, B.; Gardinier, J. R. “Electronic Communication Across Diamagnetic Metal Bridges: A Homoleptic Gallium(III) Complex of a Redox-Active Diarylamido-Based Ligand and Its Oxidized Derivatives” *Inorg. Chem.* **2012**, *51*, 12720-12728. (b) Wanniarachchi, S.; Liddle, B. J.; Kizer, B.; Hewage, J. S.; Lindeman, S. V.; Gardinier, J. R. “Syntheses and Electronic Properties of Rhodium(III) Complexes Bearing a Redox-Active Ligand” *Inorg. Chem.* **2012**, *51*, 10572-10580. (c) Wanniarachchi, S.; Liddle, B. J.; Toussaint, J.; Lindeman, S. V.; Bennett, B.; Gardinier, J. R. “Using sterics to promote reactivity in *fac*-$Re(CO)_3$ complexes of some ‘non-innocent’ NNN-pincer ligands” *Dalton Trans.* **2011**, *40*, 8776-8787.

90. (a) Güell, M.; Solà, M.; Swart, M. “Spin-state splittings of iron(II) complexes with trispyrazolyl ligands” *Polyhedron* **2010**, *29*, 84-93. (b) Gruden-Pavlović, M.; Stepanović, S.; Perić, M.; Güell, M.; Swart, M. “A density functional study of the spin state energetics of polypyrazolylborato complexes of first-row transition metals” *Phys. Chem. Chem. Phys.* **2014**, *16*, 14514-14522. (c) Swart, M.; Gruden, M. “Spinning Around in Transition-Metal Chemistry” *Acc. Chem. Res.* **2016**, *49*, 2690-2697. (d) Sirirak, J.;

Sertphon, D.; Phonsri, W.; Harding, P.; Harding, D. J. "Comparison of density functionals for the study of the high spin low spin gap in Fe(III) spin crossover complexes" *J. Quantum Chem.* **2017**, *117*, e25362.

91. Scalmani G., Frisch, M. J. "Continuous surface charge polarizable continuum models of solvation. I. General formalism." *J. Chem. Phys.*, **2010**, *132*, 114110-114124.

92. Gaussian 16, Revision B.01, Frisch, M. J.; Trucks, G. W.; Schlegel, H. B.; Scuseria, G. E.; Robb, M. A.; Cheeseman, J. R.; Scalmani, G.; Barone, V.; Petersson, G. A.; Nakatsuji, H.; Li, X.; Caricato, M.; Marenich, A. V.; Bloino, J.; Janesko, B. G.; Gomperts, R.; Mennucci, B.; Hratchian, H. P.; Ortiz, J. V.; Izmaylov, A. F.; Sonnenberg, J. L.; Williams-Young, D.; Ding, F.; Lipparini, F.; Egidi, F.; Goings, J.; Peng, B.; Petrone, A.; Henderson, T.; Ranasinghe, D.; Zakrzewski, V. G.; Gao, J.; Rega, N.; Zheng, G.; Liang, W.; Hada, M.; Ehara, M.; Toyota, K.; Fukuda, R.; Hasegawa, J.; Ishida, M.; Nakajima, T.; Honda, Y.; Kitao, O.; Nakai, H.; Vreven, T.; Throssell, K.; Montgomery, J. A., Jr.; Peralta, J. E.; Ogliaro, F.; Bearpark, M. J.; Heyd, J. J.; Brothers, E. N.; Kudin, K. N.; Staroverov, V. N.; Keith, T. A.; Kobayashi, R.; Normand, J.; Raghavachari, K.; Rendell, A. P.; Burant, J. C.; Iyengar, S. S.; Tomasi, J.; Cossi, M.; Millam, J. M.; Klene, M.; Adamo, C.; Cammi, R.; Ochterski, J. W.; Martin, R. L.; Morokuma, K.; Farkas, O.; Foresman, J. B.; Fox, D. J. Gaussian, Inc., Wallingford CT, 2016.

93. (a) Arunan1, E.; Desiraju, G. R.; Klein, R. A.; Sadlej, J.; Scheiner, S.; Alkorta, I.; Clary, D. C.; Crabtree, R. H.; Dannenberg, J. J.; Hobza, P.; Kjaergaard, H. G.; Legon, A. C.; Mennucci, B.; Nesbitt, D. J. "Defining the hydrogen bond: An account (IUPAC Technical Report)" *Pure Appl. Chem.* **2011**, *83*, 1619–1636. (b) Arunan1, E.; Desiraju, G. R.; Klein, R. A.; Sadlej, J.; Scheiner, S.; Alkorta, I.; Clary, D. C.; Crabtree, R. H.; Dannenberg, J. J.; Hobza, P.; Kjaergaard, H. G.; Legon, A. C.; Mennucci, B.; Nesbitt, D. J. "Definition of the hydrogen bond (IUPAC Recommendations 2011)" *Pure Appl. Chem.* **2011**, *83*, 1637–1641. (c) Desiraju, G. R.; Steiner, T.; The Weak Hydrogen Bonding in Structural Chemistry and Biology; Oxford University Press: New York, 1999. (d) Taylor, R.; Kennard, O. "Hydrogen Bond Geometry in Organic Crystals" *Acc. Chem. Res.* **1984**, *17*, 320-326.

94. (a) Bernstein, J. "It Isn't" *Cryst. Growth Des.* **2013**, *13*, 961-964. (b) Gu, Y.; Kar, T.; Scheiner, S. "Fundamental Properties of the CH···O Interaction: Is It a True Hydrogen Bond?" *J. Am. Chem. Soc.* **1999**, *121*, 9411–9422. (c) Desiraju, G. J. "The C−H···O Hydrogen Bond: Structural Implications and Supramolecular Design" *Acc. Chem. Res.* **1996**, *29*, 441–449. (d) Steiner, T.; Saenger, F. *J. Am. Chem. Soc.* **1992**, *114*, 10146-10154. (e) Desiraju, G. J. "The CH···O hydrogen bond in crystals: what is it?" *Acc. Chem. Res.* **1991**, 24, 290–296. (f) Taylor, R.; Kennard O. "Crystallographic evidence for the existence of CH···O, CH···N and CH···Cl hydrogen bonds" *J. Am. Chem. Soc.* **1982**, *104*, 5063–5070. (g) Gardinier, J. R.; Tatlock, H. M.; Hewage, J. S.; Lindeman, S. V. "Cyclic versus Polymeric Supramolecular Architectures in Metal Complexes of Dinucleating Ligands: Silver(I) Trifluoromethanesulfonate Complexes of the Isomers of Bis(di(1H-pyrazolyl)methyl)-1,1'-biphenyl." *Cryst. Growth Des.* **2013**, 13, 3864-3877.

95.(a) Takahashi, H.; Tsuboyama, S.; Umezawa, Y.; Honda, K.; Nishio, M. "CH/π Interactions as Demonstrated in the Crystal Structure of Host/Guest Compounds. A Database Study" *Tetrahedron* **2000**, *56*, 6185–6191. (b) Tsuzuki, S.; Honda, K.; Uchimaru, T.; Mikami, M.; Tanabe, K. "Origin of the Attraction and Directionality of the NH/π Interaction: Comparison with OH/π and CH/π Interactions" *J. Am. Chem. Soc.* **2000**, *122*, 11450–11458. (c) Nishio, M.; Hirota, M.; Umezawa, Y. *The CH-π interaction: evidence, nature, and consequences*, Wiley-VCH, Inc: New York, 1998. (d) Umezawa, Y.; Tsuboyama, S.; Honda, K.; Uzawa, J.; Nishio, M. "CH/π Interaction in the Crystal Structure of Organic Compounds. A Database Study" *Bull. Chem. Soc. Jpn* **1998**, *71*, 1207-1213. (e) Braga, D.; Grepioni, F.; Tedesco, E. "X−H---π (X = O, N, C) Hydrogen Bonds in Organometallic Crystals" *Organometallics* **1998**, *17*, 2669-2672.

96. (a) Choudhury, A. R.; Row, T. N. G. *Cryst. Growth Des.* **2004**, *4*, 47–52. (b) van den Berg, J. A.; Seddon, K. R. "Critical Evaluation of C−H···X Hydrogen Bonding in the Crystalline State" *Cryst. Growth Des.* **2003**, *3*, 643-661. (c) Brammer, L.; Bruton E. A.; Sherwood, P. "Fluoride ligands exhibit marked departures from the hydrogen bond acceptor behavior of their heavier halogen congeners" *New J. Chem.* **1999**, *23*, 965-968. (d) Grepioni, F.; Cojazzi, G.; Draper, S. M.; Scully, N.; Braga, D. "Crystal Forms of Hexafluorophosphate Organometallic Salts and the Importance of Charge-Assisted C−H···F Hydrogen Bonds" *Organometallics* **1998**, *17*, 296-307. (e) Thalladi , V. R.; Weiss , H. -C.; Bläser , D.; Boese , R.; Nangia, A.; Desiraju, G. R. "C−H···F Interactions in the Crystal Structures of Some Fluorobenzenes" *J. Am. Chem. Soc.* **1998**, *120*, 8702–8710.

97. Coronado, E.; Giménez-López, M. C.; Giménez-Saizab, C.; Romero, F. M. "Spin crossover complexes as building units of hydrogen-bonded nanoporous Structures" *CrystEngComm*, **2009**, *11*, 2198–2203.

98. Roberts, T. D.; Little, M. A.; Tuna, F.; Kilner, C. A.; Halcrow, M. A. "Isostructural salts of the same complex showing contrasting thermal spin-crossover mediated by multiple phase changes" *Chem. Commun.*, **2013**, *49*, 6280—6282.

99. Bartual-Murgui, C.; Codina, C.; Roubeau, O.; Aromí, G. "A Sequential Method to Prepare Polymorphs and Solvatomorphs of $[Fe(1,3\text{-bpp})_2](ClO_4)_2 \cdot nH_2O$ (n=0, 1, 2) with Varying Spin-Crossover Behaviour" *Chem. Eur. J.* **2016**, *22*, 12767 – 12776.

100. *CRC Handbook of Chemistry and Physics*, 77th ed.; Lide, D.R., Ed.; CRC Press: Boca Raton, FL, 1996; Section 9, Table 1.

101. (a)Trofimenko, S. *Scorpionates: The Coordination Chemistry of Polypyrazolylborate Ligands;* Imperial Press: London, 1999. (b) Pettinari, C. *Scorpionates II: Chelating Borate Ligands*; Imperial Press: London, 2008.

102. Spicer, M. D.; Reglinski, J. *Eur. J. Inorg. Chem.* **2009**, 12, 1553-1574.

103. (a) Alkorta, I.; Claramunt, R. M.; Díez-Barra, E.; Elguero, J.; de la Hoz, A.; Lopez, C. *Coord. Chem. Rev.* **2017**, 339, 153-182. (b) Pettinari, C.; Pettinari, R. *Coord. Chem. Rev.*

2005, 249, 525-543. (c) Bigmore, H. R.; Lawrence, S. C.; Mountford, P. Tredget, C. S. *Dalton Trans.*, **2005**, 635–651. (d) Reger, D. L. *Comments Inorg. Chem.* **1999**, *21*, 1-28.

104. (a) Kläui, W.; Berghahn, M.; Rheinwald, G.; Lang, H. *Angew. Chem., Int. Ed.* **2000**, *39*, 2464−2466. (b) Kläui, W.; Schramm, D.; Peters, W.; Rheinwald, G.; Lang, H. *Eur. J. Inorg. Chem.* **2001**, 1415−1424. (c) Kläui, W.; Berghahn, M.; Frank, W.; Reiβ, G. J.; Schönherr, T.; Rheinwald, G.; Lang, H. *Eur. J. Inorg. Chem.* **2003**, 2059−2070. (d) Papish E. T.; Taylor, M. T; Jernigan, F. E., 3rd; Rodig, M. J; Shawhan, R. R; Yap, G. P. A.; Jove, F. A. *Inorg. Chem.* **2006**, *45*, 2242-2250.

105. (a) Ana Caballero, M. Mar Díaz-Requejo, Manuel R. Fructos, Juan Urbano and Pedro J. Pérez "Modern Applications of Trispyrazolylborate Ligands in Coinage Metal Catalysis" in *Ligand Design in Metal Chemistry: Reactivity and Catalysis:* (eds M. Stradiotto and R. J. Lundgren), John Wiley & Sons, Ltd, Chichester, UK, **2016**, 308-329. Doi: 10.1002/9781118839621.ch11. (b) Caballero, A.; Perez, P. *J. Organomet. Chem.* **2015**, *793*, 108-113. (c) Diaz-Requejo, M. M.; Perez, P. *J. Chem. Rev.* **2008**, *108*, 3379-3394. (e) Diaz-Requejo, M. M.; Perez, P. J. *J. Organomet. Chem.* **2005**, *690*, 5441-5450.

106. (a) Dias, H. V. R.; Browning, R. G.; Polach, S. A.; Diyabalanage, H. V. K.; Lovely, C. J. *J. Am. Chem. Soc.* **2003**, 125, 9270–9271. (b) Lovely, C. J.; Browning, R. G.; Badarinarayana, V.; Dias, H. V. R. *Tetrahedron Lett.* **2005**, 46, 2453-2455. (c) Dias, H. V. R.; Browning, R. G.; Richey, S. A.; Lovely, C. J. *Organometallics* **2004**, *23*, 1200-1202.

107.(a) Maestre, L.; Sameera, W. M. C.; Díaz-Requejo, M. M.; Maseras, F.; Pérez, P. J. *J. Am. Chem. Soc.* **2013**, *135*, 1338–1348. (b) Maestre, L.; Dorel, R.; Pablo, Ó.; Escofet, I.; Sameera, W. M. C.; Álvarez, E.; Maseras, F.; Díaz-Requejo, M. M.; Echavarren, A. M.; Pérez, P. J. *J. Am. Chem. Soc.* **2017**, 139, 2216-2223.

108. Julia, S.; del Mazo, J.; Avila, L.; Elguero, J. *Org. Prep. Proc. Int.* **1984**,*16*, 299-307.

109. Reger, D. L.; Grattan, T. C.; Brown, K. J.; Little, C. A.; Lamba, J. J. S.; Rheingold, A. L.; Sommer, R. D. *J. Organomet. Chem.* **2000**, *607*, 120-128.

110. Li, Z; Capretto, D. A.; He, C. Prog. *Inorg. Chem.* **2009**, *56*, 1-48.

111. Yang, M.; Su, B.; Wang, Y.; Chen, K.; Jiang, X.; Zhang, Y. –F.; Zhang, X. –S.; Chen, G.; Cheng, Y.; Cao, Z.; Guo, Q. –Y.; Wang, L.; Shi, Z. –J. *Nat. Commun.* **2014**, *5:4707*, 1-6.

112. (a) Corbin, J. R.; Schomaker, J. M. *Chem. Commun.* **2017**, 53, 4346-4349. (b) Alderson, J. M.; Corbin, J. R.; Schomaker, J. M. *Acc. Chem. Res.* **2017**, 50, 2147- 2158.

113. (a) Martins, L. M. D. R. S. Catalysts, **2017**, 7, 12; doi:10.3390/catal7010012. (b) Wathier, M.; Love, J. A. *Eur. J. Inorg. Chem.* **2016**, 2391-2402. 49.

114. Liang, S.; Jensen, M. P. *Organometallics* **2012**, *31*, 8055-8088.

115. (a) The, K.I.; Peterson, L.K. Can. J. Chem. **1973,** *51*, 422-426. (b) The, K.I.; Peterson, L.K.; Kiehlmann, E. *Can. J. Chem*. **1973**, *51*, 2448-2451. (c) Peterson, L.K.; Kiehlmann, E.; Sanger, A.R.; The, K.I. *Can J. Chem.* **1974**, *52,* 2367-2374.